A multiscale study of magnetic nanovectors : application to USPIO contrast agents for MRI of atherotic inflammation in a murine model

Valentin-Adrian Maraloiu

Nº d'ordre 305 Année 2010

THESE DE L'UNIVERSITE DE LYON

Délivrée par

L'UNIVERSITE CLAUDE BERNARD LYON 1

ECOLE DOCTORALE

MATERIAUX

Pour obtention du

DIPLOME DE DOCTORAT

(Arrêté du 7 août 2006)

Valentin-Adrian MARALOIU

A multiscale study of magnetic nanovectors: *application to USPIO contrast agents for MRI of atherotic inflammation in a murine model*

JURY:

Pr Jose-Manuel DOMINGUEZ-VERA	Rapporteur
Dr Hana LAHRECH	Rapporteur
Pr Dominique LEGUELLEC	Examinateur
Pr Alfonso SAN MIGUEL	Examinateur
Dr Valentin TEODORESCU	Examinateur
Dr Marie-Geneviève BLANCHIN	Directeur de thèse

UNIVERSITE CLAUDE BERNARD - LYON 1

Président de l'Université	**M. le Professeur L. Collet**
Vice-président du Conseil Scientifique	M. le Professeur J-F. Mornex
Vice-président du Conseil d'Administration	M. le Professeur G. Annat
Vice-président du Conseil des Etudes et de la Vie Universitaire	M. le Professeur D. Simon
Secrétaire Général	M. G. Gay

COMPOSANTES SANTE

Faculté de Médecine Lyon Est – Claude Bernard	Directeur : M. le Professeur J. Etienne
Faculté de Médecine Lyon Sud – Charles Mérieux	Directeur : M. le Professeur F-N. Gilly
UFR d'Odontologie	Directeur : M. le Professeur D. Bourgeois
Institut des Sciences Pharmaceutiques et Biologiques	Directeur : M. le Professeur F. Locher
Institut des Sciences et Techniques de Réadaptation	Directeur : M. le Professeur Y. Matillon
Département de Biologie Humaine	Directeur : M. le Professeur P. Farge

COMPOSANTES ET DEPARTEMENTS DE SCIENCES ET TECHNOLOGIE

Faculté des Sciences et Technologies	Directeur : M. le Professeur F. Gieres
Département Biologie	Directeur : M. le Professeur C. Gautier
Département Chimie Biochimie	Directeur : Mme le Professeur H. Parrot
Département GEP	Directeur : M. N. Siauve
Département Informatique	Directeur : M. le Professeur S. Akkouche
Département Mathématiques	Directeur : M. le Professeur A. Goldman
Département Mécanique	Directeur : M. le Professeur H. Ben Hadid
Département Physique	Directeur : Mme S. Fleck
Département Sciences de la Terre	Directeur : M. le Professeur P. Hantzpergue
UFR Sciences et Techniques des Activités Physiques et Sportives	Directeur : M. C. Collignon
Observatoire de Lyon	Directeur : M. B. Guiderdoni
Ecole Polytechnique Universitaire de Lyon 1	Directeur : M. le Professeur J. Lieto
Institut Universitaire de Technologie de Lyon 1	Directeur : M. le Professeur C. Coulet
Institut de Science Financière et d'Assurance	Directeur : M. le Professeur J-C. Augros
Institut Universitaire de Formation des Maîtres	Directeur : M R. Bernard

Table of contents

French summary

Résumé

Dans le cadre du développement des nanotechnologies pour les sciences de la vie et de la santé, les nanovecteurs magnétiques connaissent un essor considérable. Ces structures composites constituées de sphères polymériques encapsulant des nanoparticules magnétiques ou d`un cœur nanoparticulaire magnétique entouré d`une couverture organique présentent une combinaison de propriétés physico-chimiques et magnétiques très performante pour le diagnostic en imageries par exemple, notamment Imagerie par Résonance Magnétique (IRM), ou la thérapie : vectorisation pharmaceutique ciblée, hyperthermie thérapeutique…L`obtention de tels vecteurs avec une taille nanométrique permet l`injection intraveineuse chez les patients et la propagation dans l`organisme, tout en augmentant l`action liée à la surface spécifique.

Les présents travaux de doctorat ont porté sur deux familles importantes de nanovecteurs magnétiques :

- des nanosphères de polymère biocompatible chargé en composé radioactivable et encapsulant des nanoparticules de magnétite, pour la thérapie tumorale
- des agents de contraste pour l`IRM de l`inflammation vasculaire ou cérébrale chez la souris, constituée d`un cœur nanoparticulaire d`oxyde de fer (maghémite ou magnétite) entourée d`une enveloppe organique pour le ciblage de la région visée (ultrasmall superparamagnetic iron oxide – USPIO, en anglais)

Pour cerner le comportement de ces nanovecteurs en interaction avec le milieu liquide de suspension, puis avec les régions ciblées dans l`organisme, une approche physique multiéchelle de leurs structure et propriétés a été développée.

Les études structurales des nanovecteurs ont été menées à bien grâce à des développements innovants s`appuyant sur les microscopies électroniques à résolution nanométrique. Par l`application du mode Wet-STEM, un nouveau mode en transmission de microscopie électronique à balayage environnementale, l`image en transmission de la structure interne organique/nanoparticule(s) magnétiques(s) a été obtenue et les simulations d`images par méthode de Monte Carlo ont montré qu`une résolution nanométrique pouvait être obtenue. Pour les nanovecteurs en environnement tissulaire, on a utilisé la microscopie électronique en transmission (MET) pour laquelle on a fait varier le degré de coloration dans des préparations de tissus ex vivo inclus en résine ; on a ainsi obtenu les premières images MET en haute résolution (METHR) spatiale d`agents de contraste USPIO cristallisés dans les tissus de l`aorte ou la rate chez la souris athérotique.

En combinant ces études structurales avec la mesure des propriétés magnétiques par SQUID, un suivi longitudinal d`agents USPIO injectés chez la souris pour l`IRM de la plaque d`athérome a été menée à bien dans l`aorte et la rate : les résultats ont été interprétés en terme d`agglomération de particules à taille variable en fonction du temps de séjour dans l`organisme et confrontés à un modèle in vitro de dégradation en milieu acide (métabolisme lysosomal).

Introduction

As applications of nanotechnologies for life and health sciences get booming, magnetic nanovectors undergo a considerable development. Such composite structures made from polymer spheres encapsulating magnetic nanoparticles or from a nanoparticular magnetic core surrounded by an organic coverage exhibit a combination of physical, chemical and magnetic properties very appropriate for diagnostic by imaging such as Magnetic Resonance Imaging (MRI), or for therapy: targeted pharmaceutical vectorization, therapeutic hyperthermia... When such vectors exhibit a nanometric size, intravenous injection and easy spread in the body of the patients are allowed, while effects related to the specific surface area are increased.

The present doctoral work was concerned by two important families of magnetic nanovectors:

- nanospheres of biocompatible polymer having loaded a radioactivable compound for tumoral therapy and having encapsulated magnetite nanoparticles for diagnostic by MRI: a system for thera-diagnostic is thus obtained.
- contrast agents for MRI of vascular or cerebral inflammation, consisting of a nanometric iron oxide (maghemite or magnetite) core i.e. ultrasmall superparamagnetic iron oxide – USPIO - surrounded by an organic coverage for targeting the affected region. These USPIO were used to study inflammation in the atherotic plaque of the aorta in a murine model.

Most of the time, such nanovectors are administered to the patients in liquid suspensions by intravenous injection. It is thus crucial to characterize both the collective behaviour and the individual structure of the vectors in liquid suspension. On the other hand their interactions with the targeted regions in the body have to be understood. For this purposes, a multiscale approach of the structure and properties of such nanovectors has been developed, with structural studies carried out through innovative developments based on electron microscopies down to subnanometric resolution and correlated with physical properties.

To achieve characterization of nanovectors in liquid media we have developed the application of Wet-STEM, a new mode in transmission of environmental scanning electron microscopy (ESEM), to image the internal structure of the magnetic nanoparticles in liquid suspension and image calculations by Monte Carlo simulations have shown that a nanometric resolution could be theoretically achieved. By the same technique, stability or tendency to flocculation in suspensions can be evidenced with respect to the collective behavior of different nanovectors.

In a second step we have investigated the interactions of the nanoparticles with targeted regions. The biodistribution and biotransformation of the USPIO contrast agents in the tissular and cellular environments were investigated at increasing spatial resolution using different techniques. The biodistribution of a MRI contrast agent grafted with a fluorophore, in ex vivo samples from atherotic aorta and spleen were revealed by biphoton microscopy with a resolution of a few hundred nanometers, down to macrophage scale. Then preparation of ex vivo samples for transmission electron microscopy (TEM) was adapted from standard protocols especially with respect to staining after inclusion in resin. This way, the first high resolution HR(TEM) images and electron diffraction patterns of crystallized USPIO contrast agents in the aorta or the spleen of an atheromatous mouse were obtained. Combining such structural studies with measurement (using a SQUID setup) of magnetic properties, a longitudinal follow-up of USPIO nanoparticles injected in mice for MRI of the atherotic plaque has been completed for USPIO particles embedded in the aorta and the spleen: the results were interpreted in terms of agglomeration of the particles with a decreasing size depending on time after injection and found consistent with a model of in vitro degradation in acidic environment proposed to mimick the lysosomal metabolism.

The manuscript is divided in different chapters. The first chapter presents an overview of the main types of nanovectors and MRI contrast agents common in the field of nanomedicine nowadays and summarizes the specifications of the nanovectors and of the contrast agents studied in the present work. In the second chapter, the techniques used to characterize the studied nanoparticular systems are described: the photonic and the electron microscopies and the magnetic measurements. The third chapter reports the study of PLLA nanospheres having encapsulated Rhenium and magnetite nanoparticles and of GUERBET USPIO contrast agents by Wet-STEM, including experimental results and image simulations. The fourth chapter is an introduction to atherosclerosis and atherotic plaque development with an example of MRI examination of the aortic plaque in a murine model using USPIO contrast agents. Iron containing species and the iron metabolism in the living organisms are then introduced. In the fifth chapter are reported the results of in vitro aging experiments for different iron oxide core nanoparticles in acid solutions mimicking the lysosomal environment. The sixth chapter is devoted to the follow up of the behavior of USPIO contrast agents after injection into an atherotic mouse using biphoton microscopy, electron microscopy techniques and magnetic measurements.

This doctoral work took place at the Claude Bernard Lyon1 University (UCBL), in the Laboratoire de Physique de la Matière Condensée et Nanostructures (LPMCN) – CNRS UMR 5586, in the frame of several interdisciplinary collaborations.

All the researches involving electron microscopies have been conceived and conducted by us from sample preparation to image simulations. Wet STEM studies were performed on the ESEM microscope of the CLYM Research Federation (whom LPMCN belongs to) in Villeurbanne (France): we were helped by Mr. A. PERRAT to operate the microscope. For STEM-HAADF and EELS studies, we had access to the TITAN microscope of Institut Matériaux Microélectronique Nanosciences de Provence (IM2NP) – UMR 6242 in Marseille, access granted by the National METSA (Microscopie Electronique et Sonde atomique) Network: on that site we were helped by Drs. Thomas NEISIUS and Jany THIBAULT-PENISSON (IM2NP) in operating the microscope and recording the data.

Concerning the collaborative researches involved in our work, we proposed the research scheme, prepared the samples (unless stated otherwise), planned and followed us the experiments. Except few exceptions, as mentioned, due to special circumstances, we took part in the experiments and in the interpretation of the results.

The study of the system for tumoral therapy was achieved in collaboration with the team of Prof. H. Fessi (Laboratoire d'Automatique et de Génie des Procédés (LAGEP) - UMR 5007, UCBL; that team elaborated the nanovectors and performed complementary physicochemical characterizations. Profs C. LETHIAS and D. LEGUELLEC at Institut de Biologie et Chimie des Proteines (IBCP) – UMR 5086 taught us the basis in cellular and tissular biology to prepare the samples for microscopies and to understand the micrographs. Prof LEGUELLEC helped us in recording visible light microscopy pictures and obtaining ex vivo samples.

Researches concerning MRI contrast agents were granted by the French National Agency for Research ANR in the frame of the INFLAM project. In that frame, collaborative work was carried out with Dr. M. SIGOVAN, Dr. A. BESSAAD and Prof. E. CANET-SOULAS (CREATIS - LRMN Laboratory – UMR 5220, UCBL), M. LEVY and Dr. F. GAZEAU (Laboratoire Matière et Systèmes Complexes – UMR 7057, Université Paris Diderot) who performed the FMR experiments, Dr. F. LAGARDE (Laboratoire des Sciences Analytiques – UMR 5180, UCBL), Drs. E. LANCELOT and S. BALLET, A. DENCAUSSE, C. FACTOR (Laboratoires GUERBET). The biphoton microscopy studies were achieved in collaboration with Dr. B. VAN DER SANDEN (Grenoble Institute de Neurosciences - Inserm U 836 - UJF - CEA – CHU); preliminary experiments were conducted in collaboration with

Dr. J.C. VIAL and H. WEGE at LSP Laboratory – Université Joseph Fourier. The magnetic measurements were performed at Centre de Magnetometrie UCBL in collaboration with Drs V. DUPUIS and A. TAMION, A. HILLION (LPMCN) and Dr. M. HILLENKAMP (LASIM).

Concerning the animal experiments, French and European regulations have been respected as well as the recommendations by the Ethics Committee of UCBL.

CHAPTER I

Composite magnetic nanovectors as multimodal systems

Diseases are a major social and health factor that influences the contemporaneous society, especially when it comes to cancers and heart diseases, both being the main causes of mortality nowadays in developed countries. The major disadvantage of most therapies is that they are not targeted to the sick region of the body leading to a general systemic distribution of the therapeutic drug. This means that not only the sick regions are affected, but also the normal, healthy ones. The solution for preventing such side-effects is the vectorization, i.e. the production of micrometric or submicrometric carriers (vectors) transporting the therapeutic drug specifically to the sick organs. This way, the amount of systemic distribution of the therapeutic agent is reduced and the required dosage is decreased. Development of nanosciences and nanotechnology introduced vectorisation in the nanometric range. Indeed, vectors of nanometric size exhibit a maximal surface area thus optimizing surface associated effects and are suitable for intravenous injections; moreover they can more easily travel in the patient's body, overcome tissular and even cellular barriers to target the cells themselves.

In this frame, composite magnetic nanovectors (nanospheres or nanocapsules) made of biopolymers encapsulating magnetic nanoparticles have been intensively studied in the last decade due to the interesting combination of their structural specifications with their magnetic properties. Indeed this combination gives rise to a very large range of applications for diagnostic: magnetic resonance imaging (MRI) and ultrasonic imaging [1, 2, 3] and for therapy: drug targeting [4], hyperthermia [5]... Many drug delivery systems developed in the last decade contains magnetic nanoparticles [6] which can be used to concentrate the therapeutic agent at the organs or tissues altered by diseases with the aid of a magnetic field. In order to ensure a more specific targeting [7], the surface of the drug delivery system can be functionalized by attaching glucides and derivatives, plasmatic proteins, protein ligands…[8]

During the last years, nanocapsules for drug targeting have been obtained from different biocompatible polymers such as polystyrene [9], polyesters like poly (lactide) (PLLA) [10], poly (D, L-lactide-co-glycolide) (PLGA) [11] and poly epsilon caprolactone (PCL) [12]. The molecular weight and crystallinity of these polymers can control the biodegradation and the drug release process [13, 14]. Other polymers such as poly (*N*-isopropylacrylamide) (PNIPPAm) or poly (*N*-vinylcaprolactam) (PVCL) enable the release of loaded drugs to be controlled by thermal and magnetic stimuli [15]. Nanovectors with functionalized surface can be targeted as chemotherapy agents to organs affected by a tumor or a disease [16, 17]. Nanovectors can also be loaded with radioactivable compounds for radionuclide intratumoral therapy: recently radioisotopes like (^{166}Ho), (^{90}Y), (^{186}Re), (^{188}Re)

have been considered [18]. Magnetic polymer nanoparticles have other useful applications (selective cell labelling and separation, immunomagnetic separation in microbiology and molecular biology) or they have a promising potential for applications in biotechnology (protein-based recognition systems, DNA-based particles aggregates, bio-nanoreactors) [19].

In MRI studies especially, nanoparticular systems consisting of a nanometric core of iron oxide (maghemite or magnetite) with an organic coating are currently used as agents to reinforce the contrast of MRI images. The advantage of iron oxide nanoparticles, compared with other metallic compounds (Gadolinium for instance), is their relatively low toxicity [6]. The latest studies [7] show that such nanovectors can be used as specific contrast agents for targeted organs.

We now consider two important families of composite magnetic nanovectors.

I.1. Polymer magnetic nanovectors for tumoral therapy

I.1.1. Composition and elaboration

The study of polymer magnetic nanovectors for tumoral therapy took place as a collaboration with the team of Prof. H. Fessi (Laboratoire d'Automatique et de Génie des Procédés (LAGEP) – Université Claude Bernard Lyon 1), specialized in the preparation of nanovectors for the transport of biomolecules and the active vectorization. Among the range of vector systems developed by this team, we chose magnetic nanovectors having loaded a radioactivable compound dedicated to tumoral therapy. In the case of the chosen system, the rhenium (^{186}Re) and (^{188}Re) radioisotopes were activated from natural rhenium ^{185}Re and ^{187}Re isotopes by neutron irradiation. Once activated, they emit β and γ radiations which will destroy the tumoral cells.

The main nanovector configurations used for tumoral therapy are the liposomes, the spheres and the capsules [20, 21]. The liposomes consist of an aqueous phase enclosed by one or more lipid layers. The spheres consist of a polymer matrix which keeps inside or at its surface the therapeutic agent (drug, DNA, proteins, peptides and genes) physically and uniformly dispersed. In the case of a capsule, the therapeutic agent is confined to a cavity surrounded by a unique polymer membrane.

Several polymers showed promising results (low toxicity, biocompatible and biodegradable properties, thermosensitivity) when used for drug delivery systems: poly (ε-caprolactone) (PCL) [12], poly(D,L-lactic acid) (PLA) [22, 23], polylactide polymer (PLLA) [10, 24], poly(D,L-lactide-co-glycolide) (PLGA) [9, 25]. In the studied case, a system of PLLA

nanospheres was chosen, loading the $Re_2(CO)_{10}$ compound as source of rhenium, and encapsulating magnetic particles.

The magnetic nanoparticles can be synthesized in solution or by aerosol/vapor methods [26, 27]. The synthesis in solution can be achieved by coprecipitation, by high-temperature decomposition of organometallic precursors or by microemulsions. Spray and laser pyrolysis are the routes of synthesis by aerosol/vapor methods.

To prepare the nanovectors, there are basically two methods: emulsion-diffusion [28] and emulsion-evaporation [29]. The nanovectors studied here were prepared by emulsion-evaporation. The organic phase was obtained by mixing oleic acid-coated magnetite nanoparticles synthesized separately (diameter ~10 nm) with the PLLA polymer and $Re_2(CO)_{10}$ compound in dichloromethane (DCM). The aqueous phase was obtained after dissolving poly (vinyl alcohol) (PVA) in continuously stirred water at 40°C. The two phases were then mixed under mechanical stirring at speed of 24000 rpm, for 2 min. Once the emulsion obtained, a rotative evaporator at 100 rpm was used for 15 min under vacuum to evaporate DCM. With such parameters the produced nanospheres exhibited a mean diameter close to 300 nm as measured by Photo Correlation Spectroscopy (PCS).

I.1.2. Physicochemical specifications

To obtain this nanovector system, the LAGEP team had studied [18] how parameters like the stirring speed, the polymer concentration or the PVA concentration control the nanoparticles size and the encapsulation efficacy.

Due to the influence on the biopharmaceutical properties and on the biodistribution of nanoparticles, the particle size is an important parameter. The main elaboration parameter that affects the size is the stirring speed. Larger speeds allow a better dispersion of the oily phase in the aqueous one leading to smaller droplets. The size is also dependent on the polymer concentration and the PVA concentration. An increase in polymer concentration leads to an increase in viscosity of the oily phase which becomes more resistant to shear forces, what yields larger nanoparticle sizes. An increase in PVA concentration tends to reduce the nanoparticles sizes: the external aqueous phase becomes more viscous and thus exerts larger shear forces on the oily phase, giving rise to smaller emulsion droplets.

Drug encapsulation efficacy is a key factor for drug delivery systems. In the case of the studied nanovectors, i.e. rhenium-loaded nanoparticles, a higher efficacy means higher radiotherapeutic doses at relatively shorter activation times. The encapsulation efficacy reached for the studied nanovectors was in the range of 81% to 98 %, meaning 13-24% mg of

Re metal/mg of nanoparticles. The parameter with the larger influence on the encapsulation efficacy is the polymer concentration in the oily phase. The encapsulation of the $Re_2(CO)_{10}$ compound increases with the amount of polymer. This is explained by the fact that an increase of PLLA in the organic phase induces an increase of the nanoparticles size leading to a decrease of the surface area which reduces the loss of $Re_2(CO)_{10}$ molecules by diffusion towards the aqueous medium during the emulsification-evaporation process. As an opposite effect, a raised probability of $Re_2(CO)_{10}$ molecules loss by diffusion towards the aqueous phase due to a decrease of the nanoparticle size, is observed when the stirring speed or the PVA concentration are increased.

I.2. Contrast agents for MRI

The main origin of the contrast observed in MRI examination of patient's body is the difference in the relaxation behaviour of the magnetic moment of the protons belonging to water molecules related to their chemical and physical properties in the tissues. **Contrast agents** are chemical substances (injected or orally administered) targeted to certain anatomical or functional regions which are being imaged and their role is to increase the image contrast between different tissues or between normal and abnormal tissue.

Several kinds of paramagnetic or superparamagnetic contrast agents covering various applications have been developed. They can be classified into three categories: gadolinium chelates, manganese chelates and iron oxide nanoparticles. Among chelates complexes of gadolinium are by far the most widely used agents because of their highest electronic spin value (S=7/2). The contrast agents act by altering the relaxation time of the protons present in the tissues or the body cavities where they get located. The origin of the reduction of the relaxation times is due to the dipolar interaction between the electronic (spin) moment of the contrast agent and the nuclear magnetic moment of the protons.

In general (but not in all the cases), paramagnetic contrast agents are composed with gadolinium while superparamagnetic agents are composed by iron oxide nanoparticles. The difference between paramagnetic and superparamagnetic contrast agents is due to the value of the electronic moment. Paramagnetic contrast agents have a weak electronic moment compared to the superparamagnetic moment.

Contrast agents are characterized by their relaxivities which depend on the value of the applied magnetic field. The relaxivities r_1 and r_2 for a given contrast agent concentration [CA] are defined by:

$$r_1 = R_1 - R_{10} / [CA] \text{ and } r_2 = R_2 - R_{20} / [CA],$$

where $R_1 = 1/T_1$ and $R_2 = 1/T_2$ are the longitudinal and the transversal relaxation rates in the presence of CA and $R_{10} = 1/T_{10}$ and $R_{20} = 1/T_{20}$ in the absence of CA. In all cases, $r_2 > r_1$.

In general gadolinium chelates have low r_1 and r_2 and these two values are approximately in the same range whereas the relaxivities of the iron particles are characterized by $r_2 >> r_1$.

For these reasons, when using gadolinium chelates, the effect of the longitudinal relaxation is exploited by means of specific MRI sequences (T_1– weigthted). In this case the region affected by the contrast agent after injection appears white, hence what is called a positive contrast.

However when using iron oxide nanoparticles the effect of the transverse relaxation is exploited using T_2 - weighted sequences. The regions affected by the contrast agents after injection appear dark and hence a negative contrast.

But it is important to understand that each contrast agent can be used as positive or negative by choosing appropriate MRI sequences.

I.2.1. Composition: a magnetic core with an organic envelope

MRI contrast agents consist of a nanometric magnetic core with an organic coating (dextran, glucose derivatives, siloxane, etc.). The organic coating has multiple purpose: blocking the agglomeration of the nanoparticles in the suspension, increasing the lifetime of the nanoparticles in the body by blocking the rapid degradation and / or the elimination, targeting to a specific region.

I.2.2. Gadolinium systems : toxicity

In the gadolinium systems, the gadolinium core is coated with chelate complexes: among them DTPA and DOTA [30, 31], of which formulas and molecular structure are displayed in Appendix I. The role of these complexes is to minimize the toxicity to a biologically tolerable level [32].

The gadolinium systems present a risk of toxicity. The free Gd^{3+} ions if accumulated in the liver, spleen and bones are toxic for the human body. At pH larger then 6.4, they do precipitate what leads to the blockage of the reticulo-endothelial system. Also they have an anticoagulant effect and they tend to block the neurotransmission and the respiratory system. In consequence, in order to be used as contrast agents, the Gadolinium systems must be very stable from a chemical point of view. Several systems are commercialized and currently used: Gd-DTPA (Magnevist), Gd-DOTA (Dotarem), gadodiamide. These Gadolinium complexes are told to be very stable (constant of stability $K > 10^{20}$ at pH 11).

I.2.3. Iron oxide systems

Another family of contrast agents is the Iron Oxide systems. They have several important advantages over the Gadolinium systems. As described later in chapter 4, Iron is a biocompatible element with a key role in the organism. These systems exhibit larger relaxivity values, what means an improved contrast. There are two types of iron oxide systems: Superparamagnetic Iron Oxide (SPIO) with a median diameter of the core larger than 50 nm and Ultrasmall Superparamagnetic Iron Oxide (USPIO) with a median diameter of the core smaller than 50 nm.

Recent studies like [33] report multiple functionalization of the surface of dextran coated superparamagnetic nanoparticles to add for instance near infrared in vivo optical imaging to MRI potentialities.

In the present work, we studied three different types of iron oxide magnetic nanoparticles. They all have a magnetic core of iron oxide, either maghemite (γ-Fe_2O_3) or magnetite (Fe_3O_4), with a typical diameter of 5 - 8 nm. Maghemite/magnetite cores were synthesized by coprecipitation of ferric and ferrous ions in alkaline medium following a classical procedure [34]. The mode of stabilization in aqueous suspension at physiological pH7 depends on the surface coating. The nanoparticles then differ by their surface coatings so that two categories of systems can be distinguished.

I.2.3.1. Anionic Magnetic Nanoparticles (AMNP)

A successful strategy for increasing the nanoparticles internalization by the cells is to coat the iron oxide nanoparticles with charged monomers. This strategy proved efficient for every kind of cell. This efficiency is due to the electrostatic interactions between the coating and the plasma membrane. Another advantage of the charged coating is the stability of magnetic nanoparticles in colloidal aqueous suspension (ferrofluid). The repulsive interactions are larger than the attractive Van der Waals and dipole-dipole interactions.

Anionic magnetic nanoparticles studied in this thesis were developed by two teams lead by Dr. C. Menager (Laboratoire Liquides Ioniques et Interfaces Chargées – Université Pierre et Marie Curie, Paris) and by Dr. F. Gazeau (Laboratoire Matières et Systèmes Complexes - Université Paris Diderot). They consist of a maghemite core which is coated with citrate. These particles are intended for in vitro cell labelling [35]. They are stabilized in water supplemented with 5 mM sodium citrate. Electrostatic repulsions are provided by the negatively-charged carboxylate ligands of citrate complexed on the nanoparticle surface.

Colloidal stability is ensured from pH 3 to pH 8 [36]. In that particle family, we used the product called D46, which exhibits a hydrodynamic size of about 30 nm, as determined by PCS.

I.2.3.2. Iron oxide contrast agents

In the present work, we studied two contrast agents families supplied by GUERBET Laboratories.

Sinerem ® (GUERBET SA in Europe and Advanced Magnetics Inc in USA, brand name Ferumoxtran ® or Combinex®) is a MRI contrast agent used for the detection of metastatic diseases in lymph nodes [37, 38]. The magnetite core is surrounded by a dextran layer, which creates steric repulsions between particles. Colloidal stability is maintained even at acidic pH<2. The measured hydrodynamic size by PCS is 20-40 nm.

Another family of contrast agent with a maghemite core is developed by GUERBET SA. In this family, P904 is intended for MRI detection of macrophages involved in inflammatory diseases [39]. Aminoalcohol derivative of glucose are grafted to the surface of the magnetic core of maghemite via phosphonate ligands. Both negative surface charges and steric hindrance ensure the colloidal stability of P904, with a hydrodynamic size of 23 – 25 nm. M' and M'' agents have a similar structure but differ from P904 by the physicochemical specifications of their envelope.

References

[1] MORAWSKI A.M., LANZA G.A., WICKLINE S.A., Targeted contrast agents for magnetic resonance imaging and ultrasound, *Current opinion in biotechnology,* 2005, 16, p. 89 - 92

[2] GUPTA A. K., GUPTA M., Synthesis and surface engineering of iron oxide nanoparticles for biomedical applications, *Biomaterials,* 2005, 26, p.3995 - 4021

[3] SHIEH D.B., CHENG F.Y., SU C.H., *et al.*, Aqueous dispersions of magnetite nanoparticles with NH3+ surfaces for magnetic manipulations of biomolecules and MRI contrast agents, *Biomaterials*, 2005, 26, p. 7183 - 7191

[4] TIMKO M., KONERACKA M., TOMASOVICOVA N., *et al.*, Magnetite polymer nanospheres loaded by Indomethacin for anti-inflammatory therapy, *Journal of Magnetism and Magnetic Materials*, 2006, 300, p. e191 – e194

[5] KIM D.H., LEE S.H., IM K.H., *et al.*, Surface-modified magnetite nanoparticles for hyperthermia: Preparation, characterization, and cytotoxicity studies, *Curr. Appl. Phys.*, 2006, 6S1**,** p. e242 – e 246

[6] IANNONE A., MAGIN R.L., T. WALCZACK, *et al.*, Blood clearance of dextran magnetite particles determined by a noninvasive in vivo ESR method, *Magn. Reson. Med.*, 1991, 22, p. 435 - 442

[7] LEE C.M., JEONG H.J., KIM S.L., *et al.*, SPION-loaded chitosan-linoleic acid nanoparticles to target hepatocytes, *International Journal of Pharmaceutics*, 2009, 371, p. 163 – 169

[8] COUVREUR P., "Les Nanos sur tous les fronts", *Journal de CNRS*, 2005, 189, p. 24

[9] ZHENG W., GAO F., GU H., Magnetic polymer nanospheres with high and uniform magnetite content, *Journal of Magnetism and Magnetic Materials*, 2005, 288**,** p. 403 - 410

[10] HU F.X., NEOH K.G., KANG E.T., Synthesis and in vitro anti-cancer evaluation of tamoxifen-loaded magnetite/PLLA composite nanoparticles, *Biomaterials,* 2006, 27, p. 5725-5733

[11] LEE Seung-Jun, JEONG Jong-Ryul, SHIN Sung-Chul, *et al.*, Magnetic enhancement of iron oxide nanoparticles encapsulated with poly(d,l-latide-co-glycolide) *Colloids Surf. A*, 2005, 255, p. 19-25

[12] HAMOUDEH Misara, FESSI Hatem, Preparation, characterization and surface study of poly-epsilon caprolactone magnetic microparticles, *J. Colloid Interface Sci.*, 2006, 300, p. 584-590

[13] KWON H.Y., LEE J.Y., CHOI S.W., *et al.*, Preparation of PLGA nanoparticles containing estrogen by emulsification-diffusion method, *Colloid Surf. A*, 2001, 182, p. 123-130

[14] LEMOINE D., FRANCOIS C., KEDZIEREWICZ F., *et al.*, Stability study of nanoparticles of poly(epsilon-caprolactone), poly(D,L-lactide) and poly(D,L-lactide-co-glycolide), *Biomaterials*, 1996, 17, p. 2191-2197

[15] LIU Ting-Yu, HU Shang-Hsiu, LIU Dean-Mo et al., Biomedical nanoparticle carriers with combined thermal and magnetic responses, *Nanotoday*, 2009, 4, p. 52 - 65

[16] PATIL Y.B., TOTI U.S., KHDAIR A., *et al.*, Single-step surface functionalization of polymeric nanoparticles for targeted drug delivery, *Biomaterials*, 2009, 30**,** p. 859 – 866

[17] ZHANG R., WU C., WANG X., *et al.*, Enhancement effect of nano Fe_3O_4 to the drug accumulation of doxorubicin in cancer cells, *Materials Science & Engineering C*, 2009, 29, p. 1697 - 1701

[18] HAMOUDEH Misara, SALIM H., BARBOS Dumitru, *et al.*, Preparation and characterization of radioactive dirhenium decacarbonyl-loaded PLLA nanoparticles for radionuclide intra-tumoral therapy, *European Journal of Pharmaceutics and Biopharmaceutics*, 2007, 67, p. 597-611

[19] NIEMEYER Christoph M., Nanoparticles, Proteins, and Nucleic Acids: Biotechnology Meets Materials Science, *Angew. Chem. Int. Ed.*, 2001, 40, p. 4128 - 4158

[20] HAMOUDEH Misara, M.A. Kamleh, R. Diab, H. Fessi, Radionuclides delivery systems for nuclear imaging and radiotherapy of cancer, *Advanced Drug Delivery Reviews*, 2008, 60, p. 1329-1346

[21] GUPTA S., YADAV B.S., KESHARWANI R., *et al.,* The Role of Nanodrugs for Targeted Drug Delivery in Cancer Treatment, *Archives of Applied Science Research*, 2010, 2, p. 37-51

[22] LEO E., RUOZI B., TOSI G., VANDELLI M.A., PLA-microparticles formulated by means a thermoreversible gel able to modify protein encapsulation and release without being co-encapsulated, *International Journal of Pharmaceutics*, 2006, 323, p. 131–138

[23] GOMEZ-LOPERA S. A., PLAZA R. C., DELGADO A. V., Synthesis and Characterization of Spherical Magnetite/Biodegradable Polymer Composite Particles, *J. Colloid Interface Sci*, 2001, 240**,** p. 40–47

[24] AAMER K.A., SARDINHA H., BHATIA S.R., *et al.*, Rheological studies of PLLA-PEO-PLLA triblock copolymer hydrogels, *Biomaterials*, 2004, 25, p. 1087 – 1093

[25] LEE D.S., SHIM M.S., KIM S.W., *et al.*, Novel thermoreversible gelation of biodegradable PLGA-block-PEO-block-PLGA triblock copolymers in aqueous solution, *Macromol Rapid Commun*, 2001, 22, p. 587–92

[26] TARTAJ P., MORALES M.P., VEINTEMILLAS-VERDAGUER S, *et al.*, The preparation of magnetic nanoparticles for applications in biomedicine, *J. Phys. D: Appl. Phys*, 2003, 36, p. R182-R197

[27] TARTAJ P., MORALES M.P., GONZALEZ-CARENO T., *et al.*, Advances in magnetic nanoparticles for biotechnology applications, *Journal of Magnetism and Magnetic Materials*, 2005, 209-291, p. 28-34

[28] GUINEBRETIERE S., BRIANCON S., FESSI H., *et al.*, Nanocapsules of biodegradable polymers: preparation and characterization by direct high resolution electron microscopy, *Materials Science and Engineering C*, 2002, 21, p. 137-142

[29] HAMOUDEH M., AL FARAJ A., CANET-SOULAS E., *et al.*, Elaboration of PLLA-based superparamagnetic nanoparticles : Characterization, magnetic behaviour study

and in vitro relaxivity evaluation, *International Journal of Pharmaceutics*, 2007, 338, p. 248-257

[30] CHAN K.W.-Y., WONG W.-T., Small molecular gadolinium(III) complexes as MRI contrast agents for diagnostic imaging, *Coordination Chemistry Reviews*, 2007, 251, p. 2428–2451

[31] BELLIN M.-F., MR contrast agents, the old and the new, *European Journal of Radiology*, 2006, 60, p. 314–323

[32] BERTIN A., MICHOU-GALLANI A.-I., GALLANI J.-L., FELDER-FLESCH D., In vitro neurotoxicity of magnetic resonance imaging (MRI) contrast agents: Influence of the molecular structure and paramagnetic ion, Toxicology in Vitro, 2010, 24, p. 1386–1394

[33] MEDAROVA Z., PHAM W., FARRAR C., *et al.*, In vivo imaging of siRNA delivery and silencing in tumors, *Nature Medicine*, 2007, 13, p. 372–377

[34] MASSART R., Preparation of aqueous magnetic liquids in alkaline and acidic media. *IEEE Trans on Magn*, 1981, 17, p. 1247 - 1248.

[35] WILHELM C., GAZEAU F., Universal cell labelling with anionic magnetic nanoparticles, *Biomaterials,* 2008, 29, p. 3161-74

[36] MASSART R.D., CABUIL V., HASMONAY E., Preparation and properties of monodisperse magnetic fluids, *Journal of Magnetism and Magnetic Materials*, 1995, 149, p. 1-5

[37] BOURRINET P., BENGELE HH., BONNEMAIN B., *et al.*, Preclinical safety and pharmacokinetic profile of ferumoxtran-10, an ultrasmall superparamagnetic iron oxide magnetic resonance contrast agent, *Invest Radiol*, 2006, 41, p. 313-24.

[38] BERND H., DE KERVILER E., GAILLARD S., BONNEMAIN B., Safety and tolerability of ultrasmall superparamagnetic iron oxide contrast agent: comprehensive analysis of a clinical development program, *Invest Radiol*, 2009, 44, p. 336-42.

[39] SIGOVAN M., BOUSSEL L., SULAIMAN A., *et al.*, Rapid-clearance iron nanoparticles for inflammation imaging of atherosclerotic plaque: initial experience in animal model, *Radiology*, 2009, 252, p. 401-409.

CHAPTER II

Experimental techniques for characterization of nanovectors from suspensions or from ex vivo samples

II.1. Photonic microscopies

II.1.1. Visible light microscopy

The role of any microscopy is to produce a magnified image of small objects and to separate close details (spatial resolution) in these objects. Photonic microscopy using the visible light is a technique which allows a rapid observation of samples, even alive ones. We used it to get overview images from ex vivo tissue slices, as detailed later.

The interaction between light and matter (Figure II.1) can induce modifications of the amplitude (due to absorption of photons) and of the phase of the light.

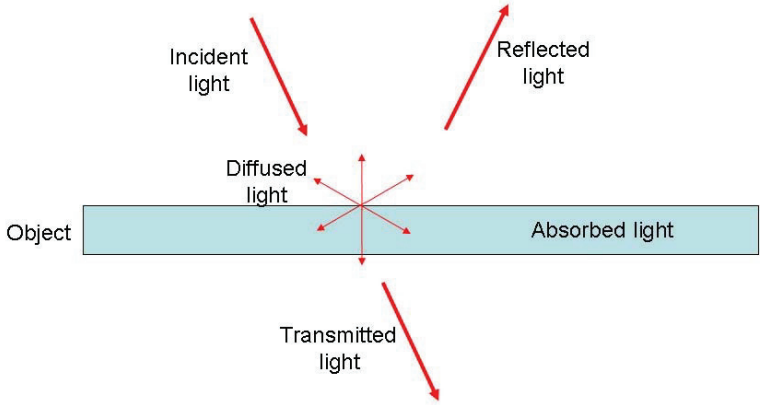

Figure II.1. Interaction between light and matter.

It has been shown [1] that the spatial resolution achieved by a microscope is mainly controlled by the imperfections of the apparatus (basically the aberrations of the optical lenses) and also by the diffraction phenomena in the sample, from where comes the Rayleigh criterion (Figure II.2).

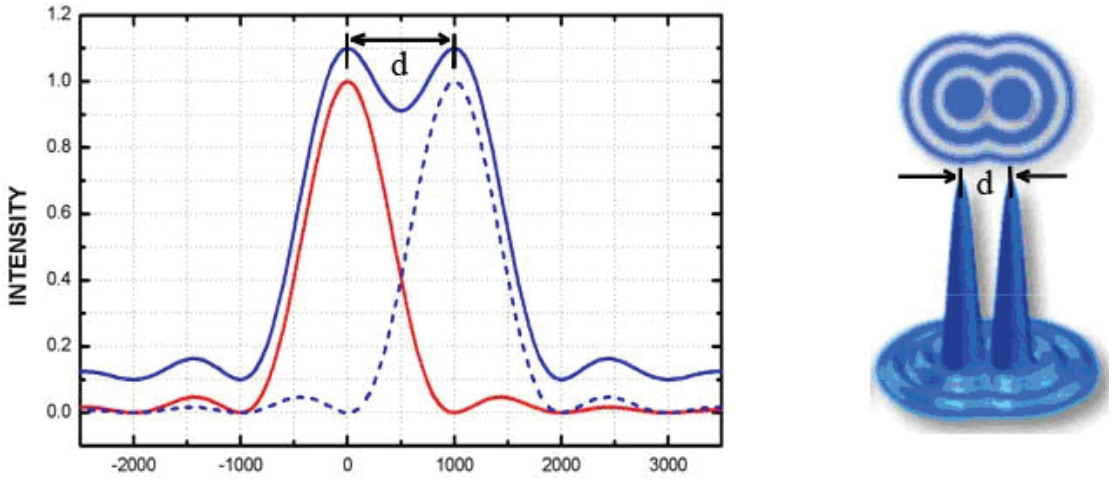

Figure II.2. The resolution limit as defined by the Rayleigh criterion.

The Rayleigh criterion which states that two points can be separated if the principal diffraction maximum of one is at the first minimum of the spot nearby, gives a relationship to establish the spatial resolution:

$$d = 0{,}61 \cdot \lambda / n \sin\alpha$$

where λ is wavelength of the incident beam, n is the index of refraction in the sample and α is the angle of aperture of the incident beam.

Finally, for latest models of visible range microscopes the resolution is about 300 nm.

In Figure II.3, a cutaway diagram of a modern photonic microscope is reproduced. The illumination source is a lamp. The photons are concentrated on the specimen using a condenser lens. The transmitted beam of photons is collected by the objective lens. The obtained magnified image of the specimen is observed either via an eyepiece, either using a CCD camera or a photographic camera.

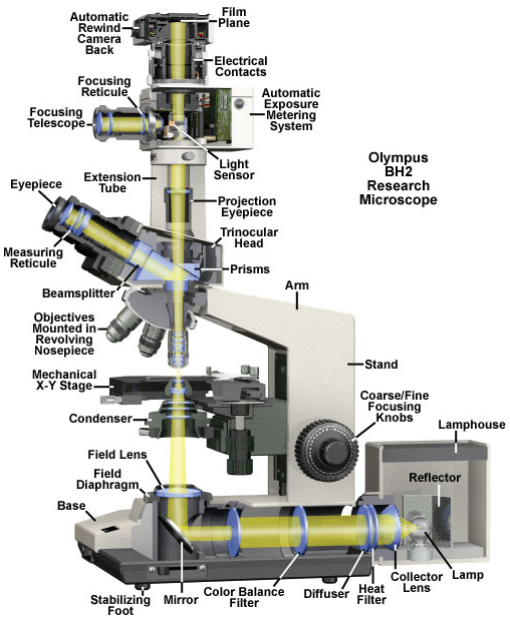

Figure II.3. A cutaway diagram of a modern microscope showing the optical pathways.

II.1.2. Two photon microscopy

The two photon microscopy [2] is a technique based on the non-linear excitation of fluorescent molecules in the sample, this excitation being induced by the addition of two photons in the infrared (IR) wavelength domain. This three-dimensional imaging technique allows the observation of living specimens due to a reduced photodamage for the exciting IR photons. The two photon microscopy possesses an intermediate resolution between the light microscopy and the transmission electron microscopy, along with the possibility of

observation of subcellular structures in deep tissue layers; therefore we used it to investigate the distribution of contrast agent nanoparticles in ex vivo samples from tissues of mouse's aorta, spleen or liver.

In Figure II.4, the principles of single photon and of two photon microscopies are comparatively presented. In single photon microscopy, an electron passes from the ground state to an excited state absorbing a photon with the energy equal to the energy of the gap. In two photon microscopy, the molecule is excited by the first photon to an intermediate state and the absorption of the second photon brings the molecule to the final excited state. **The reduced photodamage comes from the use of two less energetic photons**. For the two cases, the molecule relaxes to the first electronic excited state by vibrational processes and then returns to the ground state by emitting a photon.

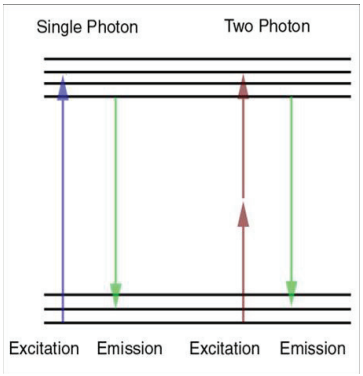

Figure II.4. Principles of single photon and of two photon microscopy.

The different energies needed in the two cases, so that an electron passes from the ground state to an excited state, imply the use of lasers with different wavelengths. In the case of single photon excitation, lasers with wavelength in the UV-visible domain (Argon, He-Ne) are required. In the case of two photon excitation, wavelengths in the IR domain are needed. The advantage of the IR radiation is its better penetration in diffusing (absorbent) environment, especially in physiological tissues.

Single photon microscopy is currently achieved using a confocal microscope. In the single photon/confocal case, the probability that the excitation photons are being scattered (1 and 3) is high, due to their shorter wavelength. A pinhole in front of the detector is necessary in order to eliminate the photons originating from off-focus sections (5) and those coming from focal section whose direction was changed by a scattering event (6). In consequence, only the ballistic fluorescence photons (4) generated in the sample (i.e., unscattered) reach the photomultiplier detector (PMT). In the multiphoton

case, a larger fraction of the excitation light reaches the focus (2' and 3'). The scattered photons (1') have an insufficient energy to cause 2-photon excitation. Since the fluorescence excitation is limited to the focal section, both ballistic (4') and scattered photons (5') constitute a useful signal for the image. [3]

One of the key components is the excitation light source, typically a mode-locked Titanium-Sapphire laser, which produces femtosecond pulses. The high photon density and flux required for two photon excitation typically correspond to a pulse width of approximately 100 femtoseconds and a repetition rate of about 80 MHz. The excitation wavelength can be varied between 700 and 1000 nm. A region of the specimen is illuminated by raster scanning of x-y mirrors by means of a galvanometer-driven scanner. The dichroic mirror is custom made to maximize the reflection of the infrared radiation and to transmit the radiation in the blue-green region of the spectrum.

The fluorescent radiation emitted from the sample is collected by the objective and transmitted to the dichroic mirror to the detection system. The most commonly used photodetectors are photomultiplier tubes due to their good sensitivity, large active areas, low price.

For our experiments, a **ZEISS LSM 7 MP** microscope was used at the Grenoble Institut des Neurosciences (GIN). A piezomotor interfaced with a computer translates the microscope objective in vertical steps of 1- 5 μm to acquire the optical sections at different depths in the specimen. Typical observations were performed with 800 nm excitation light and an incident power of 3200 mW.

II.1.3. Sample preparation

For both visible light microscopy and two photon microscopy, the ex vivo tissue samples were first fixed and included in the Epon resin according to the protocol which will be described further in the later section concerning the electron microscopy sample preparation.

For visible light microscopy, thin sections (thickness ≈ 0.5 μm) were cut by microtome from the resin blocks containing the tissue samples. These sections were put on glass slides and observed using a photonic microscope as described in the 2.1.1 section.

For two photon microscopy, the ex vivo aorta samples were cut longitudinally, opened and stretched out in a Petri dish with the atherosclerotic plaque towards the objective of the

microscope as depicted in Figure II.5. In the case of the liver or spleen, a thin section was cut with a razor blade. The samples were covered with distilled water and a glass cover.

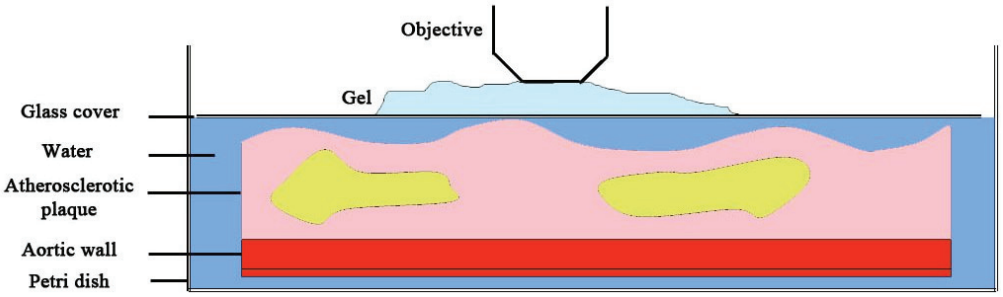

Figure II.5. Schematic illustration (not at scale) of the set-up for observation of ex vivo aorta in two photon microscopy.

II.2. Electron microscopies

In any microscopy, the resolution is proportional to the wavelength of the incident radiation as expressed by the Rayleigh criterion (section II.1.1). In electron microscopies, the light beam is replaced by an electron beam. Electrons emitted by an electron gun are accelerated by an electric field due to a difference in potential between 100 and 400 kV for commonly used microscopes.

The electrons accelerated at relative speeds by the difference of potential V_0 have a wave behaviour characterized by a wavelength λ given by De Broglie expression:

$$\lambda = \frac{h}{|p|}$$

where h is the Planck constant and **p** is the impulse of an electron. The expression of wavelength depending on the accelerating voltage V_0 is:

$$\lambda = \frac{h}{\sqrt{2 \cdot m_0 \cdot e \cdot V_0 \left[1 + \frac{e}{2 \cdot m_0 c^2} \cdot V_0\right]}}$$

where m_0 and e are the mass and the charge of the electron, c is the speed of light in vacuum. For an acceleration voltage of 200 kV, the wavelength of the electrons is then 0.0025 nm.

Radiations/particles	Wavelength (nm)
Photons (visible)	400 to 700
Photons (X domain)	$5 \cdot 10^{-2}$ to 1.25
Electrons	10^{-3} to $3 \cdot 10^{-3}$

Protons or ions	$\approx 10^{-4}$
Neutrons	≈0.1

Table II.1. Wavelength corresponding to different radiations or particles.

When comparing the wavelength corresponding to electrons, photons and x-rays (Table II.1), it can be easily observed that a better resolution is obtained for electrons.

II.2.1. Interactions between electron beam and sample: basics for electron microscopies

When an incident electron beam hits a sample, different categories of electrons (e's) or radiations are transmitted, diffracted or reemitted by the sample [4], as summarized in Figure II.6.

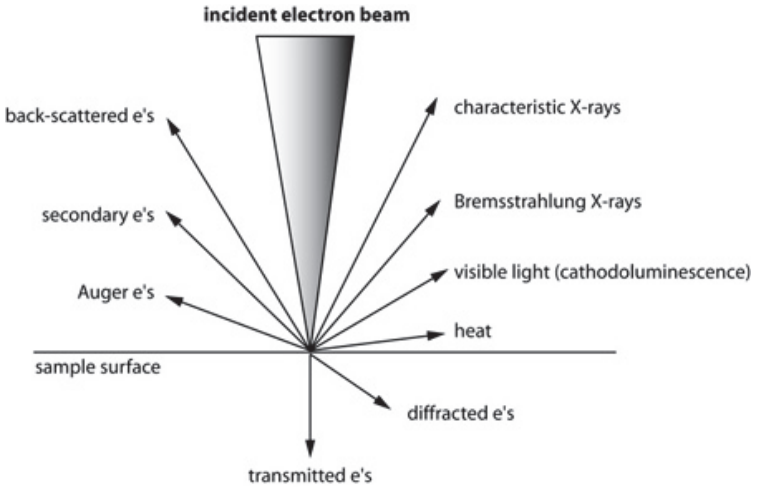

Figure II.6. Electron beam - sample interaction [3].

This results from the different types of interactions between the incident electron beam and the atoms of the sample:

- elastic interactions without energy loss:
    - transmitted electrons,
    - elastically diffused electrons,
    - backscattered electrons.
- inelastic interactions with energy loss:
    - inelastically diffused primary electrons,
    - secondary electrons,
    - AUGER electrons,
    - X radiation,
    - Cathodoluminescence...

The different electron microscopies correspond to the categories of electrons or radiations collected to obtain the image.

Transmission electron microscopy uses the transmitted and diffracted electrons, whereas standard scanning electron microscopy uses backscattered and secondary.

The backscattered electrons leave the sample after a series of elastic collisions. The secondary electrons are generated by the ionization of electronic levels of the sample's atoms. They have a low energy (less than 50 eV) and they are quickly absorbed in the sample by inelastic diffusion. They are emitted in the whole volume of interaction but only those that are produced at less 5λ distance from the surface can be retrieved for scanning techniques.

The X-rays radiation characteristic of sample elements results from the interaction between the sample atoms and the incident electrons decelerated in the atomic cores; it is used to achieve a chemical analysis of the samples.

II.2.2. Environmental Scanning Electron Microscopy (ESEM)

This microscopy is an advanced development of scanning electron microscopy (SEM).

II.2.2.1. Standard ESEM

Standard ESEM enables observation of hydrated samples in a humid low vacuum atmosphere. This is achieved by keeping water vapor pressure in the specimen chamber of the microscope. In the conventional SEM, the entire column is operated under high vacuum. In the environmental SEM [5], the column is divided into different parts with differential vacuum.

The interactions of the electron beam with the water vapor molecules enable both to protect the specimen and to amplify the image signal. The collisions between the incident electron beam and the gas molecules produce positive ions which neutralize the negative charges on the observed surface so that metallic covering of insulating samples is not necessary. There is also an amplification of the signal of the secondary electrons due to a cascade effect: secondary electrons emitted after the interaction of the electrons from the incident beam with the surface interact with the gas molecules producing positive ions and other secondary electrons which are collected by the image signal detector.

II.2.2.2. Wet-STEM

For our studies, we used a particular ESEM mode recently developed by Bogner et al. [6, 7], mode called Wet-STEM (Figure II.7). In this mode, the two sector semi-annular

detector normally used for the backscattered electrons is placed under a former TEM holder supporting the sample grid hit by the incident beam. In this mode, the sample is seen in transmission. Our samples of liquid suspensions containing nanovectors were put on the back side of TEM copper grids coated with holey carbon film thus giving rise to retention basins.

In the specimen chamber, the control of the pressure and of the temperature by means of the PELTIER stage enabled us to keep a water layer thin enough for the transmitted and backscattered electrons to be collected.

At CLYM Research Federation (in Villeurbanne), we used a FEI XL30 FEG ESEM, which has a nominal resolution of 2 nm, possible acceleration voltage between 0.2 and 30 kV, magnification between 15 and 500000, pressure in the specimen chamber up to 20 Torr. It is equipped with a Peltier stage that can cool / heat between - 20° C and + 20° C.

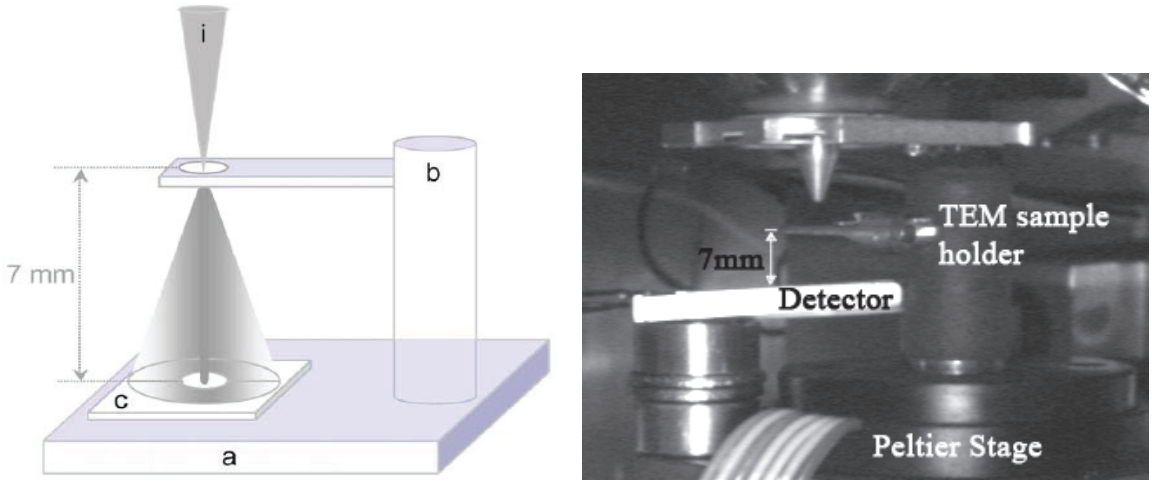

Figure II.7. Schematic illustration of the Wet-STEM mode: focused incident electron beam (i); Peltier stage (a); TEM former holder supporting the sample grid hit by i (b); solid-state detector (c).

II.2.2.3. Sample preparation

The starting specimen consisted of a droplet of 5 µl of the diluted suspensions containing the nanovectors, deposited with a micropipette on the backside of holey carbon film coated TEM copper grid so that the carbon film within the copper squares acted as retention basin.

II.2.3. Transmission Electron Microscopy (TEM)

To image the specimens, TEM uses electrons which keep enough energy after interactions with sample atoms to exit out of the specimen.

II.2.3.1. Conventional TEM

The optical schema of an electron microscope is rather similar to photonic microscope, but the light radiation is replaced by electron beam and the optical lenses by electromagnetical lenses. On Figure II.8, the optical scheme and the cross section view of the TOPCON microscope are reproduced.

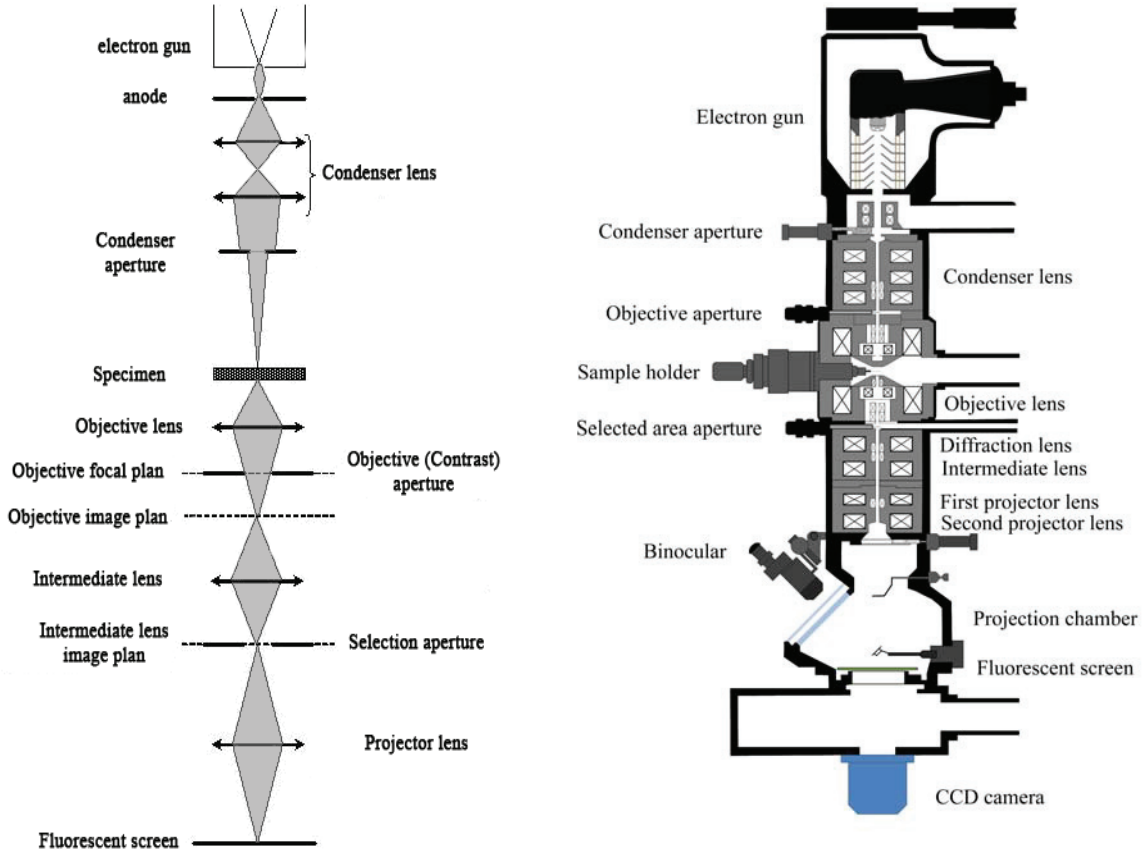

Figure II.8. The optical scheme of a transmission electron microscope (left) and a cross-section view of the TOPCON 02B microscope (right).

It can be recalled that the electrons produced by the electron gun will undergo different types of interaction with the atoms of the specimen:

- elastic interactions without energy loss
- inelastic interactions with energy loss.

Basically, CTEM uses electrons having undergone *elastic interactions* in the specimen travelling along the optical axis or along directions at small angles with respect to optical axis.

When the electron beam passes through a crystalline sample, the diffraction phenomena occurs leading to the strengthening of intensity elastically diffused by sample in

certain directions, according to the Bragg law. One or several beams are diffracted at small angles 2θ (between 10^{-3} and 10^{-2} rad) when, for example, the wavelength for the electrons accelerated at 200 kV is λ = 0.00251 nm. These angles are defined by the Bragg relation:

$$2 \cdot d_{hkl} \cdot \sin\theta = n \cdot \lambda,$$

where n is the order of reflexion, d_{hkl} is the distance between the reflecting crystalline planes and θ is the incident Bragg angle.

Different combination modes for the excitation of the electron lenses lead to obtention of an image or a diffraction pattern. When the intermediate lens of the microscope is focalized on the image focal plane of the objective lens, a diffraction diagram is obtained. The diagram corresponds to the intersection between the reciprocal space of the observed sample with the observation plane (screen).

In the case of a single crystal object, this diagram is made by spots each representing a family of crystalline planes (hkl). In the case of the powder, the spots are situated on concentric rings centered on the optical axis, in which the diameters correspond to different families of planes (hkl). A continuous background due to the inelastic diffusion superposes with the spot or the rings.

On the other hand different types of images can be obtained. With the help of the contrast diaphragm in the objective lens focal plane, one or more electronic beams can be selected to build the image. If the transmitted beam is selected, all diffracted beams are blocked. In the resulting image, the regions which satisfy the Bragg diffraction condition are darker than the regions which do not diffract, as crystals deviated from the Bragg position, holes in the material. The resulting image is called image in bright field (see Figure II.9a). If a diffracted beam is selected, it highlights the regions that contribute with electrons to the selected beam. These regions appear bright on a dark background. The image is called dark field (Figure II.9b) image.

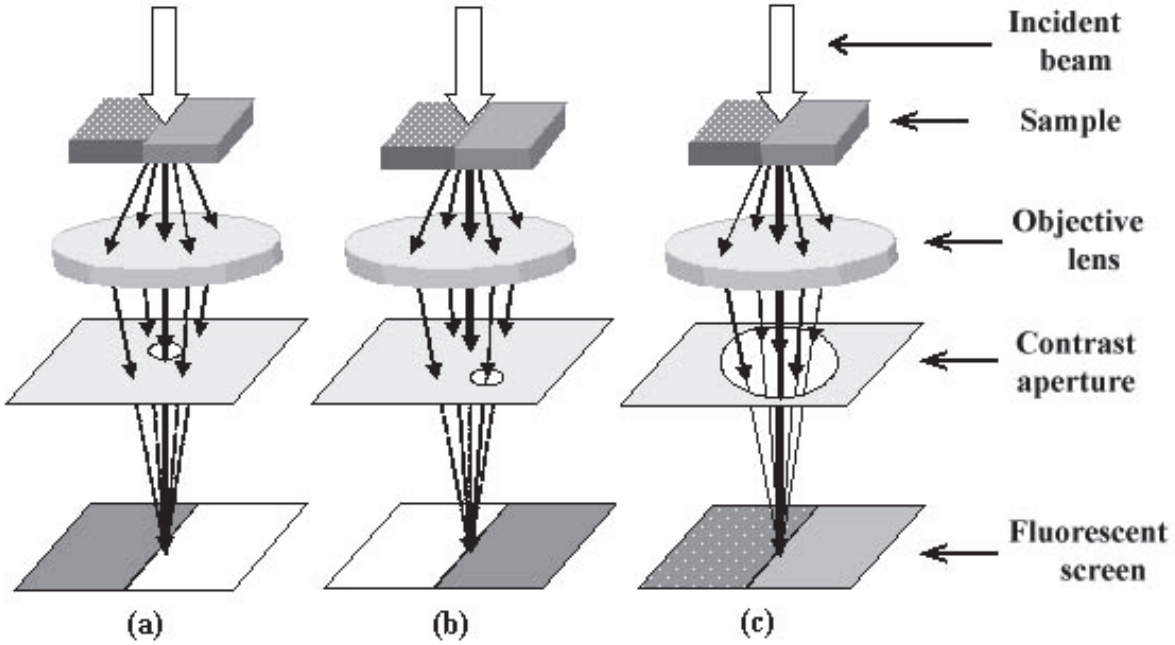

Figure II.9. Formation of a bright field (a), a dark field (b) and a high resolution (c) image.

II.2.3.2. High Resolution TEM

High-Resolution TEM (HRTEM) is a TEM mode that enables the imaging of the crystallographic structure of a sample at the atomic scale. At this level, individual atoms and crystallographic defects can be observed. In this mode, the image is obtained from the interferences between the transmitted beam and one or several beams diffracted by different families of planes (Figure II.9c). This interference phenomena leads to the visualization of the atomic columns of a crystal viewed parallel to a zone axis of observation.

The formation of HRTEM images can be explained by quantum mechanics and by physical optics in which the electrons behavior is described by a wave function.

The dynamical theory of the diffraction of electrons by crystals allows establishing the wave function Ψ_S described as a superposition of plane waves:

$$\Psi_S(r) = \sum_g a_g \, e^{i\varphi g} \cdot e^{2\pi i(g+k_0)\cdot r},$$

where **r** represents the distance from the origin, $\mathbf{k_0}$ is incident electrons wave vector, **g** is the diffraction vector and a_g , φ_g represent the amplitude and the phase of all the transmitted and diffracted beams.

a_g and φ_g depend on the crystal structure, its orientation and its thickness. The wave function Ψ_S at the exit of the crystal contains all the information regarding the object. If the microscope would be a perfect optical system, the Fourier transformation of Ψ_S, TF(Ψ_S)=$\widetilde{\Psi}_S$, would be obtained in the image focal plane. The imperfections of the optical system, particularly the aberrations of the objective lens, affect the image formation. This is translated by the action of the transfer function T(f), f being the spatial frequency (f = 1/d). So, in the focal plane we have $\widetilde{\Psi}_i(f)=T(f)\cdot\widetilde{\Psi}_S(f)$.

The optical specifications of the microscope being known, the contrast transfer function (CTF) can be calculated. On the other hand, the interactions of the electrons with the atomic potential in the sample can be simulated by different methods (Bloch waves equations, multislice approximations…) [4, 8] to calculate Ψ_S. The convolution of Ψ_S with CTF gives the image wave function Ψ_i whose modulus corresponds to the intensity in the experimental image [9].

II.2.3.3. Scanning TEM

The Scanning Transmision Electron Microscopy (STEM), like CTEM, uses the electrons that pass through a thin specimen. The difference is that, in the case of STEM, a focused electron beam is scanning the sample in a raster pattern. Two pairs of scan coils, used to deflect the beam, ensure that the scanning beam remains parallel to the optic axis. If this condition would not be satisfied, the electron scattering processes (especially diffraction) would vary with the angle between beam and sample, making the interpretation of the image contrast very difficult [8].

Just like in SEM, the signal generated at one point on the sample is collected by the electron detector and amplified. A synchronous signal is displayed at the equivalent point on the screen. The fact that there are no lenses to form the image is an advantage versus TEM because the resolution of the image is not affected by the defects of the imaging lenses (chromatic aberration in particular).

There are three detectors to obtain different types of images. The Bright-Field (BF) detector (semiconductor or scintillator) intercepts the direct beam. In this case, just like in TEM, bright-field images are obtained. If the detector is shifted off axis and a beam of scattered electrons is selected, a dark-field image is formed. The second detector is the annular dark-field (ADF) detector. Centered on the optical axis, it has a hole in the middle in

which the BF detector is placed and collects dark-field images. The advantage over the BF detector placed off-axis is that its annular shape permit the collection of more diffracted beams leading to a more intense signal. The third detector, similar with the ADF, collects the electrons scattered out to higher angles, so they are called high-angle ADF (HAADF).

II.2.3.4. X-ray analysis

X-ray spectroscopy can be associated with the electron microscopies.

Such a X-ray analysis is based on the characteristic X-rays generated by a sample hit by incident electrons to identify the constituent elements of the sample. The incident electrons interact with the electrons located on the first energy level of the atoms. These electrons are excited and then they leave the atom. At their places, holes remain which are filled by electrons from higher energy levels. The difference between the energy of higher levels and that one of lower level is freed as X-ray radiation [10]. The energy and the intensity of the released X-rays are measured by an energy dispersive spectrometer (EDS). The energy of the X-rays is characteristic of the difference in the energy of the two atomic levels and thus of the atomic structure of the element from where they are emitted.

EDS spectrometers are fit with a crystal detector (SiLi or Ge). When X-ray hits the crystal of the detector, its energy is adsorbed by a series of ionization events in the semiconductor creating electron - hole pairs. The electrons pass in the conduction band of the semiconductor and they can move in the crystal structure. The holes are free positive charges. A high extraction voltage applied between the contacts of the crystal moves the electrons and the holes to opposite electrodes. The resulting signal is proportional with the energy of the incident X-ray radiation. This spectroscopy is currently abbreviated as EDX. Its typical resolution is in the range 70 – 130 eV with respect to peak energies in the range of a few keV to 40 keV.

II.2.3.5. Electron Energy Loss Spectrometry

Electron Energy Loss Spectrometry (EELS) is a complementary technique with respect to EDX and is based on the changes in the energy and angular distribution of the monoenergetic incident electron beam due to the inelastic scatterings occurred during the transmission through a thin specimen [11].

The zero loss peak represents the signal from the electrons which pass through the specimen without energy losses or with negligible ones. The other part of the spectrum can be divided into two energy regimes. The low-loss regime corresponds to plasmon oscillations, induced by excitation of the valence electrons. The signal for this regime belongs to the domain of 1 to 50 eV. Higher energy peaks correspond to the electrons that had lost energy creating vacancies in the deeper core levels of the atoms. These energy losses are characteristic of each chemical element.

The principle of an EELS detector is the following. The electrons transmitted through the sample are focused onto the entrance plane of the spectrometer. They are then deflected by a uniform magnetic field perpendicular to their velocity vector. The radius of the circular trajectory is directly proportional to the velocity i.e to the energy of the electrons and inversely proportional to the strength of the magnetic field.

II.2.3.6. Specifications of the different TEM microscopes

TOPCON 002 B microscope, located in the Laboratoire de Physique de la Matiere Condensée et Nanostructures (LPMCN), has a point by point resolution of 0.18 nm, with possible acceleration voltage between 20 and 200 kV, magnification between 1400 and 800.000. EDX is also possible.

FEI Titan 80-300, located in Institut Materiaux Microelectronique Nanosciences de Provence and belonging to the National METSA Network, is equipped with correctors for geometrical aberrations. It is capable of a point by point resolution of 0.08 nm, with possible acceleration voltage between 80 and 300 kV, maximal magnification of 1.500.000. It is equipped with detectors for STEM – BF & DF, HAADF – STEM and with a EELS spectrometer.

II.2.3.7. Sample preparation for TEM studies

Two types of preparation protocols were achieved depending on the starting sample.

Observation of nanovectors in suspension

To characterize the morphology and the size distribution of the vectors, a droplet of 5 µl of diluted suspension was deposited on a holey carbon coated TEM copper grid and then let air-dry before introduction in the microscope.

Preparation of ex vivo tissue samples

A protocol inspired by biological TEM sample preparation was followed in several steps: fixation, dehydration, inclusion in a resin, microtomy and post-coloration.

The ex-vivo tissues were fixed in the fixer (1.5% glutaraldehyde and 1% paraformaldehyde in buffer 0.15 M cacodylate). Samples were cut in a Petri dish with a layer of fixer in several parts of order of mm^3 which were left for four hours at room temperature.

The pieces were washed four times with cacodylate buffer 0.15 M for 15 minutes each bath and they were left overnight in the buffer. Samples were placed in a bath of osmium fixer (OsO_4) 1% for 45 minutes to post-fixation: this step is very important because if the time is exceeded, artifacts can appear.

All products used must be at pH 7.4 to meet the pH of the cells.

After a quick wash with distilled water, the next step is ethylic dehydration. It is practiced at room temperature. Samples stay once in 30°, 50°, 70°, 95° alcohol baths for 5 minutes and then three times in 100° alcohol bath for 10 minutes. The purpose of this step is the elimination of water from the samples. Dehydration continues with 2 baths for 10 minutes in pure propylene oxide.

After dehydration, the inclusion in the Epon resin was achieved. Samples were first placed for one hour in a resin mixture (Epon A, Epon B, BMDA (1.7% of the mixture A + B)) and pure propylene oxide (volume/volume with A + B + BMDA mixture) for the substitution by alcohol with the resin. It was followed by a bath for 1 hour in the resin. This step was followed by impregnation in a bath for 12 hours in a mixture of Epon A, Epon B, BMDA (1.7% of the mixture A + B). The bath was renewed after 12 hours.

Samples were then placed in moulds with a mixture of impregnation freshly prepared and left a day at 37 ° C and three days at 60 ° C for the polymerization of Epon. The next step was obtaining ultra-fine sections by means of a Reichert-Jung (Leica) Ultra-cut 701701 ultramicrotome. The cuts were put on grids of nickel or copper coated with Formvar. Once the cuts obtained, they could be contrasted with uranyl acetate (10 minutes) and with lead citrate (5 minutes).

II.3. Magnetic measurements

II.3.1. Characterization of the magnetic properties of the contrast agents

The iron oxide core of the contrast agent nanoparticles has a typical magnetic behaviour. The agents are stored at the targeted site and in the main iron storage organs (liver

and spleen). As source of exogenous iron, they should suffer changes in their crystallographic structure in order to be stored in a more biocompatible form. The quantity of exogenous iron in the organs being of order of milligrams, a very sensitive technique is needed to detect the magnetic changes suffered by the iron oxide nanoparticles due to their crystallographic transformations. A SQUID magnetometer can measure very small *magnetic moment* of nanometric samples under applied field, from where the magnetization and magnetic susceptibility of the samples can be determined.

II.3.2. Principle of a SQUID magnetometer

The magnetic measurements were carried out using a Superconducting Quantum Interference Device (SQUID) magnetometer. This instrument is based on the Josephson effect. This effect consists in a flow of resistanceless current through a very thin insulator which separates two superconductors [12].

The special properties the Josephson junction cause the impedance of the SQUID loop to be a periodic function of the magnetic flux threading the SQUID so that a modulation signal applied to the bias current is used to measure the impedance and to linearize the voltage to flux relationship. The net result is that a SQUID functions as a flux to voltage converter with unrivaled energy sensitivity.

To measure the magnetic moment of our particles placed in magnetic field created by a magnet, we used a Magnetic Property Measurement System (MPMS) equipped with a SQUID detector. During a measurement, the sample is moved through the superconducting detection coil located outside the sample chamber at the center of the magnet. When the sample moves through the coils, an electric current is induced in the detection coils by the magnetic moment of the sample. The detection coils, the connecting wires and the SQUID input coil form a closed superconducting loop, so a change of magnetic flux in the detection coils produces a change in the persistent current in the detection circuit proportional to the change in magnetic flux. The SQUID acts as a highly linear current-to-voltage convertor. The variations in the current in the detection coils produce variations in the SQUID output voltage. These variations are proportional to the magnetic moment of the sample.

II.3.3. Description of the equipment

We used the Quantum Design MPMS XL-7 at the Magnetometry Center of Université Claude-Bernard, whose diagram is sketched in Figure II.10 [13]. The SQUID is located inside a small cylindrical, superconducting magnetic shield in the middle of liquid helium dewar. This minimizes helium evaporation due to excessive heating. The special geometry of the detection coil is less sensitive to the magnetic influence of distant sources. The coil is mounted at the bottom of the dewar, close to the head.

The key components of the MPMS are (Figure II.10): 1 – sample rod; 2 – sample rotator; 3 – Sample transport; 4 – probe assembly; 5 – Helium level sensor; 6 – superconducting solenoid; 7 – flow impedance; 8 – SQUID capsule with magnetic shield; 9 – superconducting pick-up coil; 10 – Dewar isolation cabinet; 11 – Dewar; 13 – magnet power supply; 14 – temperature controller; 15 – console cabinet; 16 – power distribution unit; 17 – MPMS controller; 18 – gas/magnet control unit.

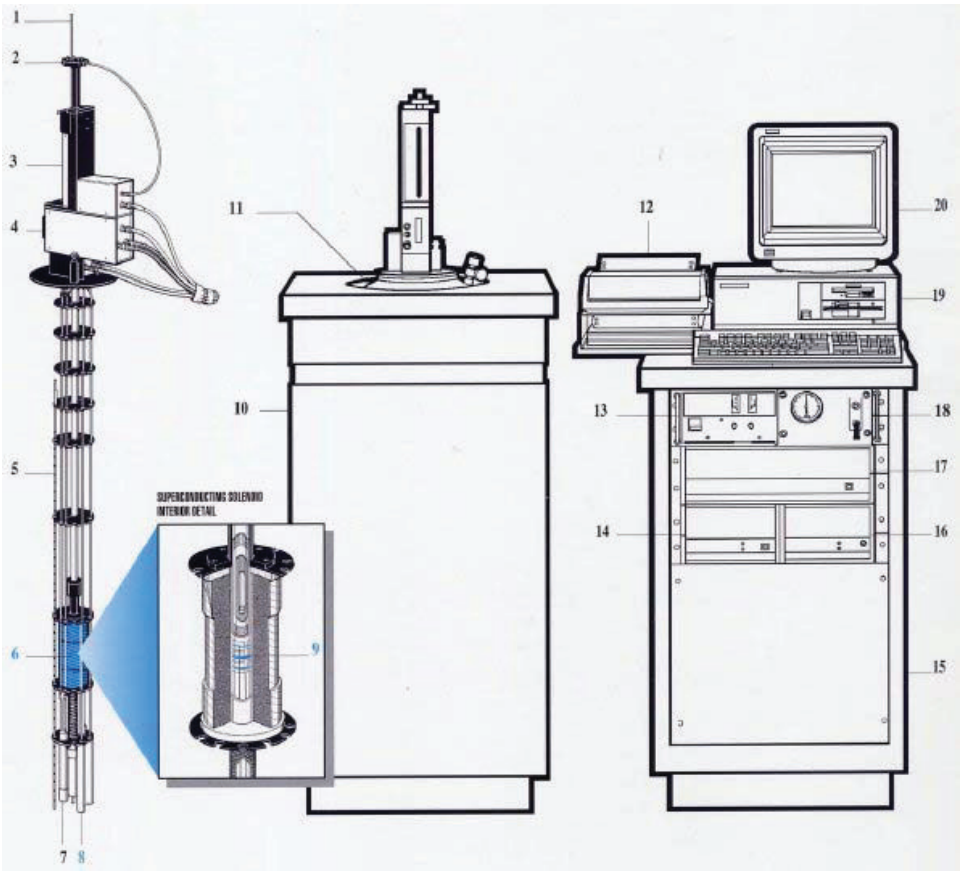

Figure II.10. Illustration of a SQUID magnetometer.

References

[1] CRUT A., Microscopie optique, 2008, Cours Master M2 "Imagerie des Microstructures", Université Claude Bernard, Lyon

[2] SO P.T.C., DONG C.Y., MASTERS B.R., BERLAND K. M., *Annu. Rev. Biomed. Eng*., 2000, 02, p. 399–429

[3] DENK, W., STRICKLER, J.H., WEBB, W.W., Two-photon laser scanning fluorescence microscopy, *Science,* 1990, 248, p. 73–76

[4] REIMER L., Transmission Electron Microscopy – second edition, 1989, Springer Verlag, Berlin

[5] DERRICK M.R., DOEHNE E.F., PARKER A.E., STULIK D.C., *Journal of the American Institute for Conservation*, 1994, 33, p. 171 - 184

[6] BOGNER A., THOLLET G., BASSET D., *et al.*, Wet STEM: A new development in environmental SEM for imaging nano-objects included in a liquid phase, *Ultramicroscopy*, 2005, 104, p. 290 - 301

[7] BOGNER A., JOUNEAU P.-H., THOLLET G., *et al.*, A history of scanning electron microscopy developments: Towards 'wet-STEM' imaging, *Micron*, 2006, 38, p. 390 – 402

[8] WILLIAMS D., CARTER C.B., Transmission Electron Microscopy: A textbook for materials science – second edition, 2009, Springer Science, New York

[9] BLANCHIN M.G., NIHOUL G., BERNSTEIN E., HREM imaging and simulation with image-processing for the study of phase-transformations in nanometric Zirconia powders, *Philosophical Magazine A*, 1992, 65, p. 683 - 705

[10] An Introduction to Energy-Dispersive and Wavelength-Dispersive X-Ray Microanalysis, 2006, *Microscopy and Analysis: X-Ray Supplement*

[11] BRUNDLE C.R., EVANS C.A., WILSON S., *Encyclopedia of materials characterization: surfaces, interfaces, thin films*, Butterworth-Heinemann, 1992

[12] BUSCHOW K.H.J. – *Concise Encyclopedia of Magnetic and Superconductivity Materials – 2Edition*, Elsevier, 2005

[13] CLARKE J., BRAGINSKI A.I. – The SQUID Handbook, vol. I&II, Wiley, 2006

CHAPTER III

Study of suspensions of magnetic nanovectors by electron microscopies: from TEM to Wet STEM

The structural characterization of nanovectors obviously requires the high resolution capabilities (down to the nanometer scale) of the electron microscopy techniques: conventional (C) and high resolution (HR) transmission electron microscopy (TEM) as well as scanning electron microscopy (SEM). But for most of their applications, the nanovectors have to be dispersed in liquid media: fluids for labs-on-chips, suspensions to be injected in the patient's body. Both the sample preparation techniques and the high vacuum environment required by the classical electron microscopies do not enable liquid media to be observed. Recently, a new generation of scanning electron microscopes was designed, which allow samples to be observed under low vacuum condition or in liquid atmosphere environment: this corresponds to what is called the Environmental Scanning Electron Microscopy (ESEM). The nanovectors can be thus observed in some humid environment using conventional ESEM. Doing so, the ionization of gas molecules after the collision with the electrons of the beam prevents the sample charging and amplifies the electron signal coming from the specimen. The best amplification is obtained for water vapor compared with other gas like: carbon dioxide, nitrogen oxide, nitrogen, helium [1]. The ESEM standard operating conditions use electrons reemitted through the sample surface in secondary electron (SE) or backscattered electron (BSE) mode, the signal being collected by the gaseous SE detector (GSED) or by the gaseous BSE detector (GAD). In this standard modes, only the secondary electrons coming from a distance of a few nanometers below the sample's surface contribute to the image with a good spatial resolution of a few nm (close to the nominal resolution of the SEM microscope). Hence conventional ESEM studies cannot provide informations about the ***internal*** structure of composite polymer nanovectors having encapsulated magnetic particles for instance nor on the structure deep inside liquid suspensions where the nanovectors can be dispersed.

To overcome this difficulty, a new ***transmission*** mode of ESEM was developed which provides transmission images of nanoparticles in liquid suspensions, so called Wet Scanning Transmission Electron Microscopy i.e. Wet STEM [2, 3, 4]. We developed application of this mode to image liquid suspensions containing composite nanovectors of two main types for current uses. Firstly we selected biocompatible polymer nanospheres having encapsulated a Re compound activable by neutron irradiation for tumoral therapy and having loaded magnetite nanoparticles for localization. Secondly we observed nanoparticles used as MRI contrast agents, consisting of a small size iron oxide core inside an organic coverage. Here are reported the capabilities of Wet STEM studies to reveal both the collective behavior (dispersion or agglomeration…) of the vectors in the liquid medium and the internal structure of individual nanovectors.

III.1. Types of vectors studied

As told before, we studied two basic types of nanovectors.

As first type, we chose polymer nanovectors for tumoral therapy. An system of PLLA nanospheres having encapsulated 23% Re w/w (2% at) and 10% w/w of magnetite (Fe_3O_4) nanoparticles, was prepared by an oil-in-water emulsion-solvent evaporation method as introduced in Chapter I and characterized by physicochemical techniques as described in [5]. Previous conventional TEM studies revealed a certain polydispersity in the size of the nanospheres ranging between about 100 and several hundreds of nanometers [6] and the magnetite nanoparticles were observed as having a mean diameter of about 10 nm, thus exhibiting a superparamagnetic behavior as confirmed by magnetic studies of the nanovectors [5]. For storage the suspensions were desiccated and the vectors stored as powder. The powder was then redispersed in distilled water to obtain the desired suspensions. For instance the suspension for injection in a patient's body corresponded to a mass of 193 mg of nanospheres per liter of water.

Vectors of second type were MRI contrast agents provided by GUERBET Laboratories. The contrast agent particles consisted of an iron oxide maghemite (gamma-Fe_2O_3) core having a mean size 5 nm, as determined by X-ray diffraction, inside an organic coverage derived from glucose. They were provided in suspensions corresponding to an iron concentration close to 350 mM. Two families M and M' were studied with coverages differing in their precise chemical composition and the hydrodynamical diameter of the coverage was 36 nm and 28 nm respectively, as determined by PCS.

For these two types of vectors, a morphological and structural study was first achieved by TEM combining different modes (CTEM, electron diffraction, HRTEM). For this purpose, a drop of the liquid suspensions was released on a TEM copper grid covered by a holey carbon film and then let dry before introduction in the microscope.

We now present the results from these investigations of which limitations highlight the need for Wet-STEM studies.

III.2. TEM structural study: performances and limitations

The TEM data for the two MRI **contrast agents** M' and M'' are summarized in Figures III.1 and III.2. It can be seen that the distribution of the nanoparticle size is large, ranging from 2 nm to 20 nm as shown by the distribution fit (Figures III.1.c and III.2.c) but the most probable sizes are 5 nm, in agreement with X-ray diffraction data.

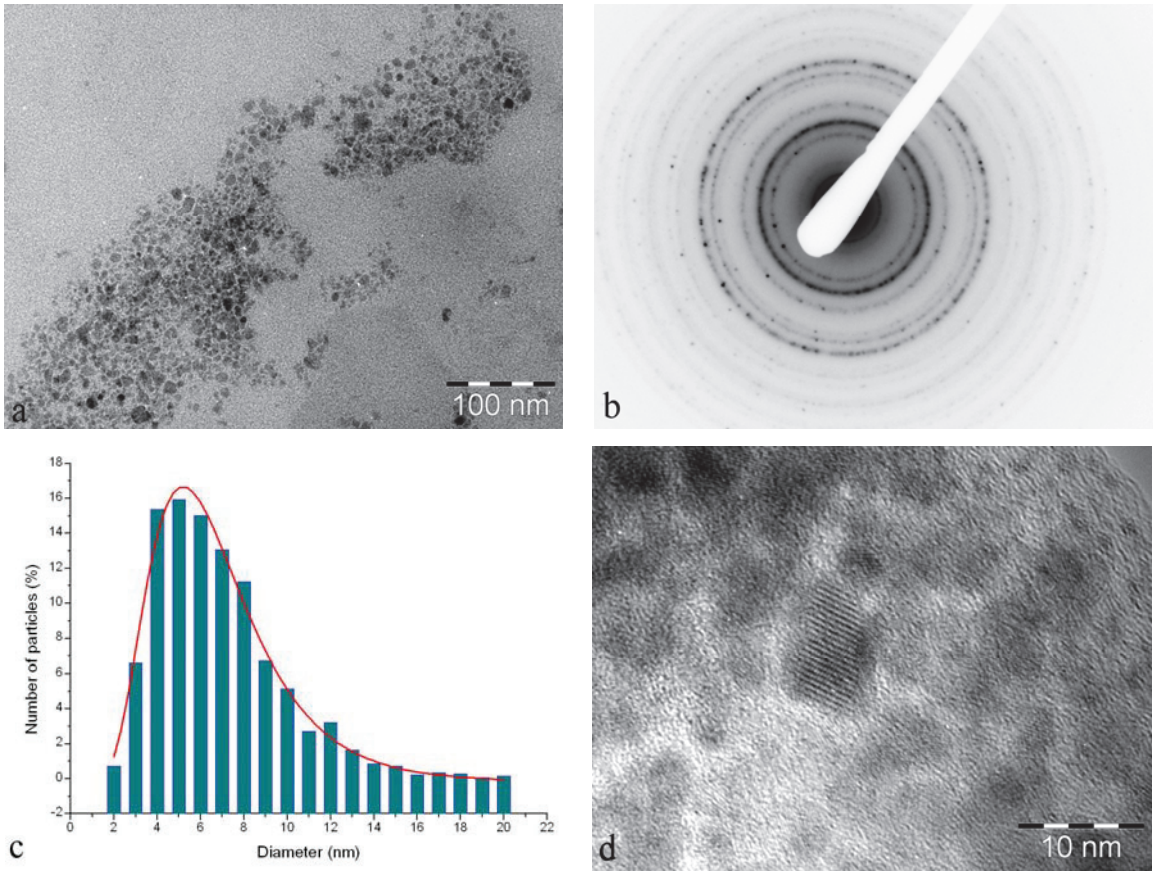

Figure III.1. TEM study of contrast agent M: CTEM (a), diffraction pattern (b), size distribution (c), HRTEM (d).

The electron diffraction patterns (Figures III.1b and III.2b) confirm that the nanoparticles are well crystallized in the maghemite structure.

Hence, the HRTEM images (Figures III.1.d and III.2.d) reveal the lattice of many particles. Most of them are rather spherically shaped, but larger ones tend to exhibit rhombohedral shape.

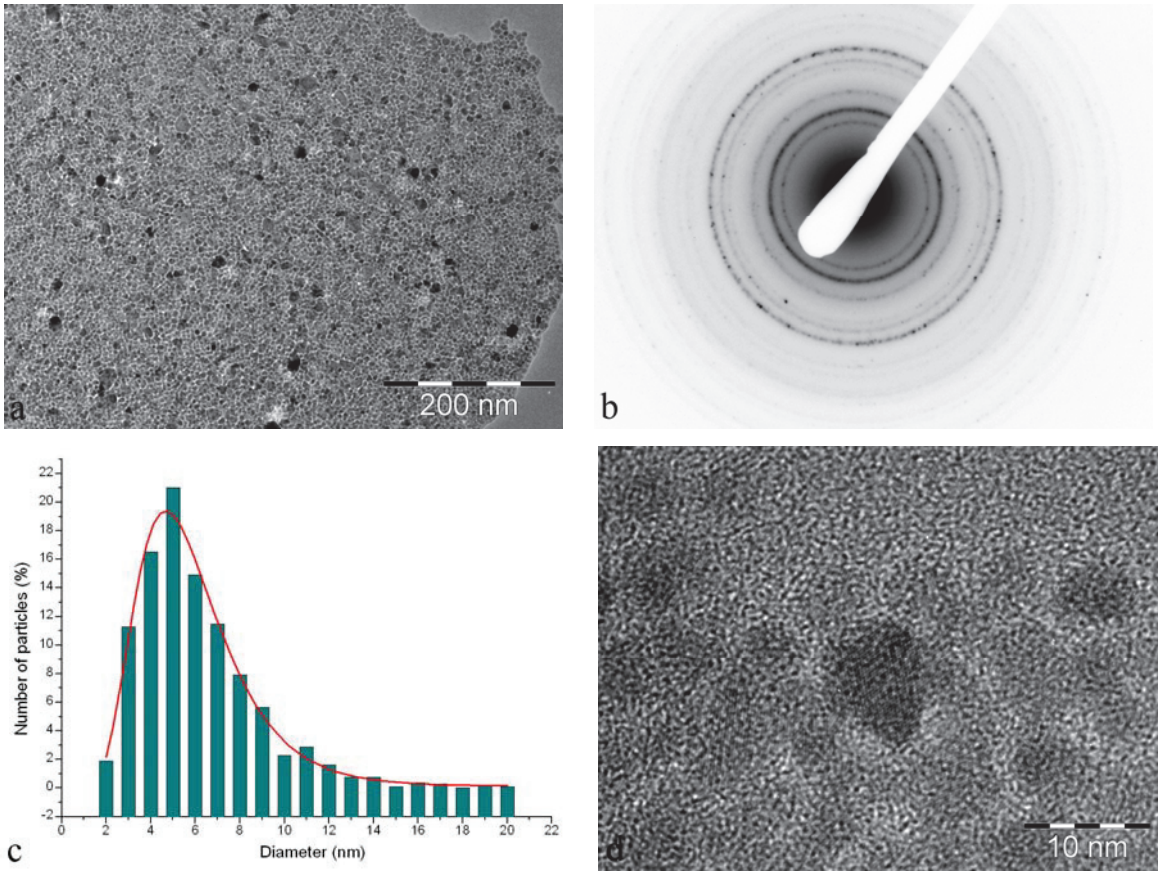

Figure III.2. TEM study of contrast agent M': CTEM (a), diffraction pattern (b), size distribution (c), HRTEM (d).

TEM study of **nanovectors for tumoral therapy** is illustrated by Figure III.3 a and b. CTEM images of well preserved PLLA nanospheres reveal the inside encapsulation of the magnetite nanoparticles whereas higher magnification image with Moiré patterns and diffraction pattern confirm that the nanoparticles are crystallized in the magnetite structure.

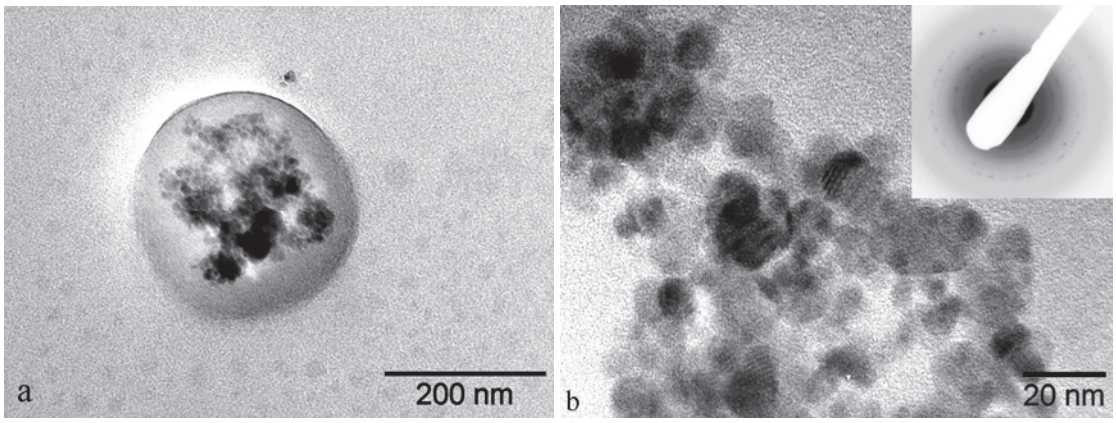

Figure III.3. CTEM images showing a well preserved PLLA nanosphere (a) and the crystallized magnetite nanoparticles viewed at larger magnification (b).

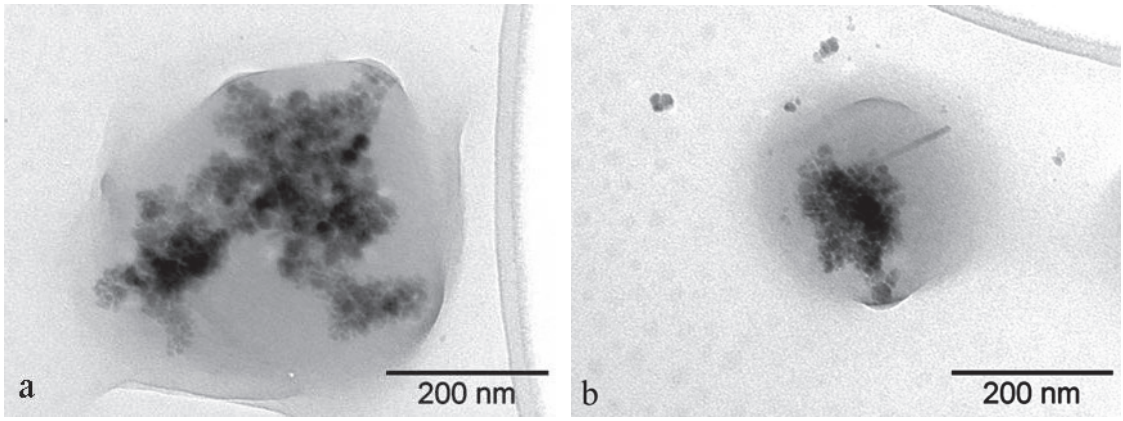

Figure III.4. CTEM images showing degraded nanospheres.

Figure III.4 reveals the first limitation of the TEM approach, i.e the degradation of the PLLA nanospheres by explosion under vacuum. The other disadvantage of the technique is that is does not allow the determination of the collective behaviour of the nanospheres in the liquid suspension, in which they are injected into the patient's body. To characterize this behaviour, another technique of observation is required.

III.3. Interest of Wet STEM for study of suspensions

III.3.1. Experimental procedure

A FEI XL 30 FEG ESEM microscope operated at 30 kV was used, its nominal resolution being 2 nm. The set up designed for Wet STEM studies was placed below the GAD detector (which remains also available) in the microscope chamber and is sketched on Figure III.3a. A TEM copper grid (coated with a holey carbon film) was linked to the Peltier stage (1) mounted on the head of a TEM sample holder (2), being irradiated by the incident electron beam *i*. A circular semiconductor detector made of two semiconductor diodes (3) normally used for backscattered electrons (BSE) was placed below the sample allowing the collection of electrons scattered at energies between 5 and 30 keV. The distance between the copper grid and the detector being 7 mm, the electrons passing through the sample were collected in solid angles between 20° and 47° and the corresponding signals were summed over the two diodes. Such operating conditions are those of annular dark field imaging, the electrons transmitted through the specimen along and close to the incident beam direction being not collected. Such values of the operating parameters were practically determined [2] to increase the signal and enhance the contrast from light element specimens like polymers.

The starting specimen consisted of a droplet of 5 µl of the diluted suspensions containing the nanovectors, deposited with a micropipette on the backside of the holey carbon film coated TEM copper grid so that the carbon film within the copper squares acted as retention basin.

On the basis of previous studies by Bogner et al [2, 3], an optimized pump down sequence was used in order to prevent evaporation from or condensation on to the sample droplet. When the required partial pressure of water less than 10 torr is reached, pressure and temperature can be adjusted to evaporate a very small amount of water from the droplet. The endothermic evaporation reaction can be followed by checking the difference between the setting temperature of the Peltier stage and the measured value. Thin films of wet samples are then obtained in situ, their thickness being controlled by evaporation from the initial droplet. The water layer can thus be thinned until the incident electrons can pass through it to form the Wet STEM image. Then a desired layer thickness can be kept constant on the basis of the (p,T) equilibrium water phase diagram of Figure III.3b. For instance, a pressure of 5.3 torr is required at a sample temperature of 2°C to maintain the sample in a uniform liquid water layer.

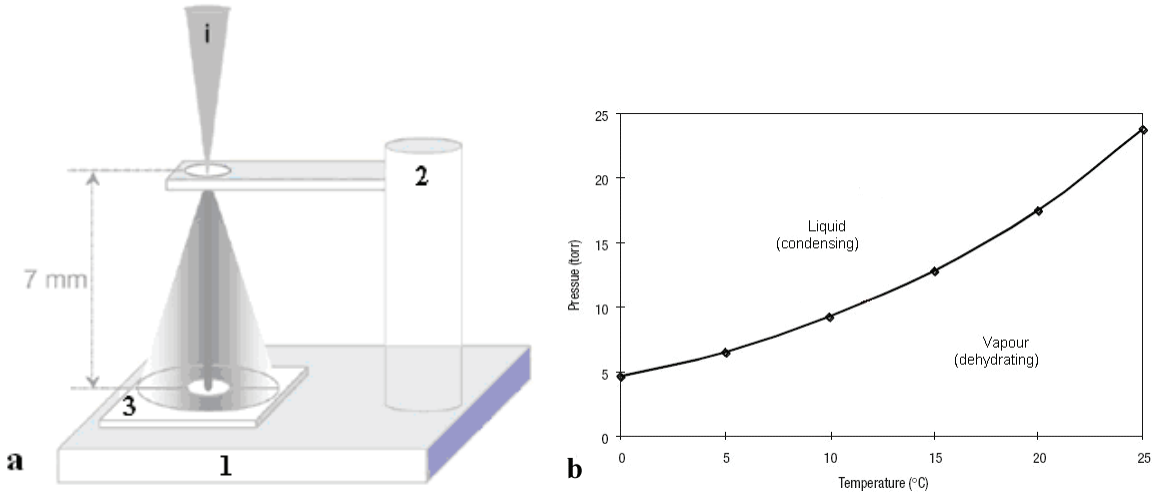

Figure III.3. Experimental set up used for the ESEM/ Wet STEM studies (a). Water phase diagram(b).Courtesy from Agnes Bogner (Bogner et al. 2006) and Elsevier.

III.3.2. Experimental results

III.3.2.1. Nanovectors for tumoral therapy

We first observed droplets from suspensions corresponding to a nanovector concentration suitable for injection in patient's body (Figure III.4a) and then from suspensions rediluted with distilled water (Figure III.4b and c) to favor study of individual nanospheres under optimal conditions.

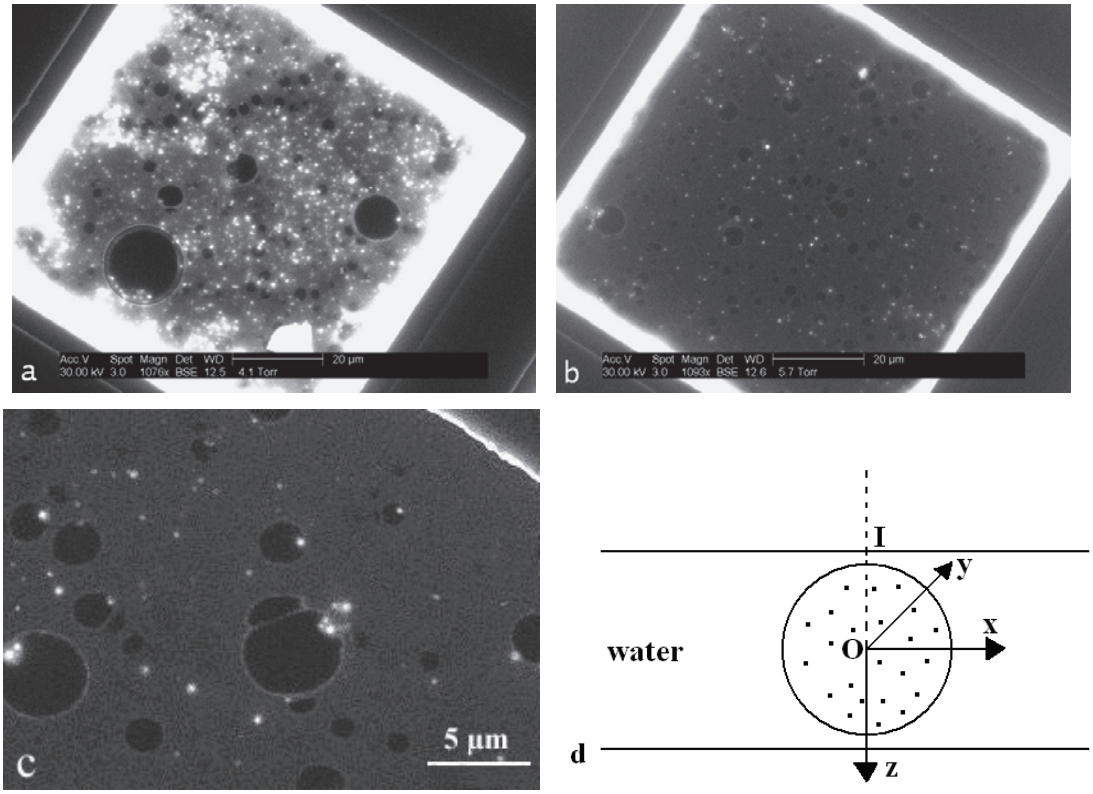

Figure III.4. Sequence of Wet STEM images (a,b,c) revealing the nanovectors as bright spots on the holey carbon film as the water film thickness decreases; sketch for the system consisting of a nanovectors sphere in a water film (d), IO being the direction of the incident electron beam.

At the beginning of the experiment, the setting temperature of the Peltier stage is 2°C and the water droplet covers the entire TEM grid. By means of the upper GAD detector the presence of water can be observed as a uniform constant covering all the grid squares. As the pressure is decreased gradually, the water in droplet starts evaporating. At a certain thickness the water film becomes transparent enough with respect to the grid bars and the imaging mode is then switched to Wet STEM by means of the BSE detector. Then the holey carbon film in each grid square can be imaged in Wet STEM mode (Figure III.4a) and superimposed on the carbon film, the nanospheres are seen as white spots. On such images, the spheres can be observed rather well dispersed and non agglomerated in this case. If the pressure is decreased further more in the case of diluted suspensions, the width of the bright band due to the water meniscus around the bars of the grid squares diminishes (Figure III.4b), what means that the water evaporation continues. A convenient thickness of the water film is reached when a narrow bright line (Figure III.4c) is observed around the bars of the grid square. The nanospheres are still observed over the holes of the carbon film: the water layer then covers the whole surface of the carbon film.

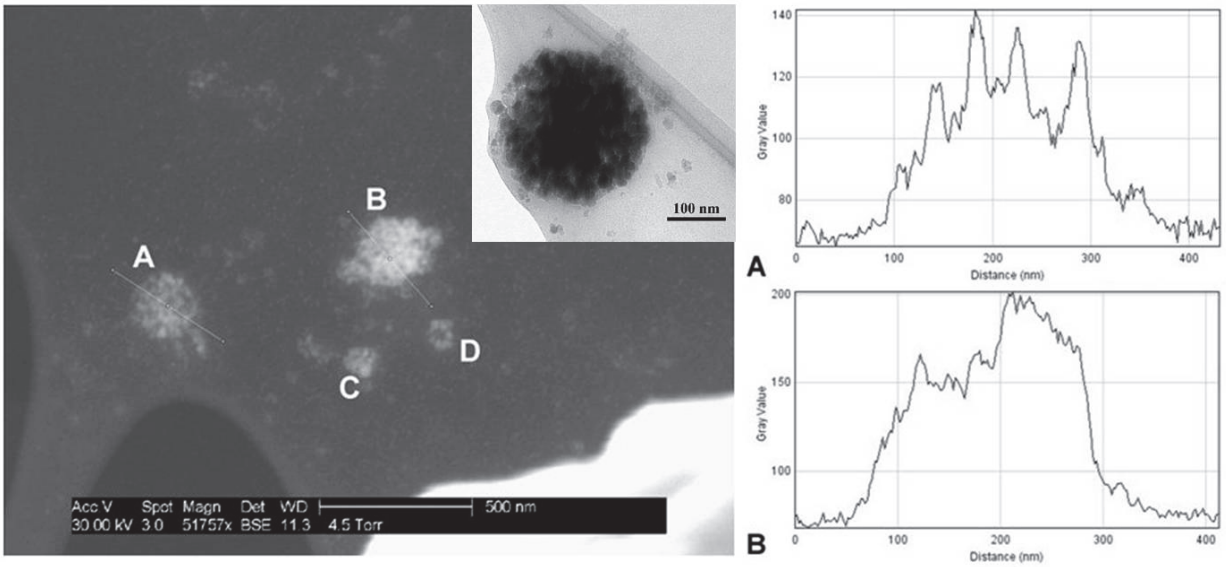

Figure III.5. Magnetite loaded PLLA/Re nanospheres (with TEM bright field image as insert) viewed at larger magnification in Wet STEM mode and experimental image profiles A and B (right side) corresponding to the line tracks marked across spheres A and B respectively.

At increasing image magnification, individual spheres can be studied like A and B (~200 nm in diameter) in Figure III.5. The contrast inside these spheres suggests the presence of brighter nanoparticles with a diameter consistent with that one of the magnetite nanoparticles (about 10 nm) in a darker matrix and this is well depicted by the experimental image profiles A and B (Figure III.5 right). This interpretation is also consistent with the TEM images from the same nanospheres (see an example in insert): however it should be reminded here that TEM images are recorded in bright field whereas Wet STEM images correspond to a dark field mode. Similar nanospheres having a smaller diameter can be also seen, in C and D (Figure III.5) for instance. Such images appeared to be stable over quite a long time during observations and image recording. Clearly the distribution and the total density of the magnetite nanoparticles can be assessed as being different inside sphere A or sphere B for instance.

III.3.2.2. MRI contrast agents

The other advantage of Wet STEM technique over TEM is that it can reveal also the collective behavior of the nanoparticles in the liquid environment. This advantage is well illustrated in the Figure III.6. It can be observed that contrast agent nanoparticles of the M family are well dispersed in the suspension, while those of M' family exhibit a tendency to flocculation.

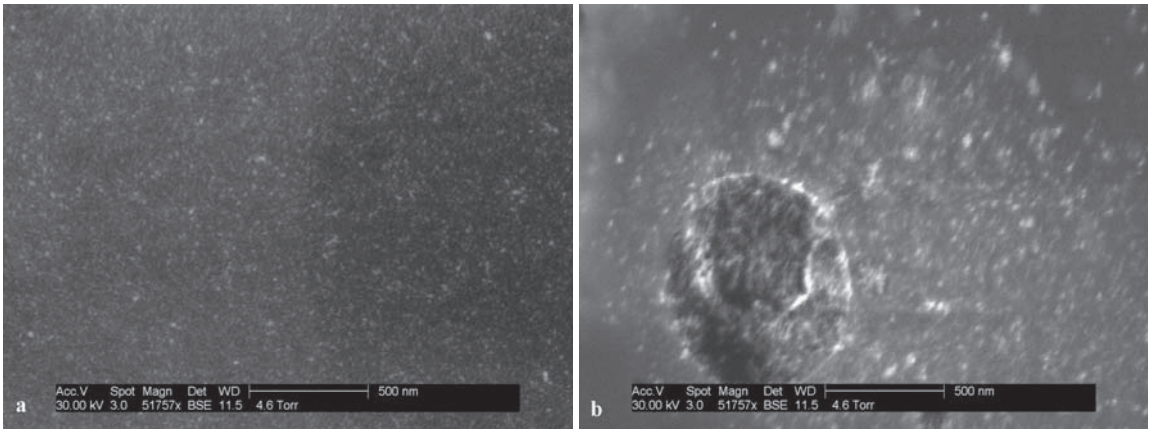

Figure III.6. Wet STEM images of two contrast agents: M (a) and M' (b).

III.3.3. Contrast interpretation by Monte Carlo simulations

To simulate the trajectories of the electrons diffused through the specimen, a software package designed by the SamX Co. (Saint Laurent du Var, France) was used, called Hurricane. This software is based on evolved Monte Carlo models in which each elastic and inelastic interaction is treated individually within a computation unit cell which is triperiodically repeated [21]. The acceleration voltage was 30 keV and the number of electrons incident on to the sample was 100 000, the computation unit cell being $10\times10\times10$ nm^3.

The specimen was defined by the chemical data concerning its compounds (chemical elements of the compound with their atomic ratio and mass per volume of the compound) and by geometrical coordinates within a triedra (Figure III.4d) where the z axis corresponds to the direction of the incident electron beam. Basically our specimens consisted of a water film of finite thickness along the z direction with spheres of fixed radius located at the center 0 of the water film, which is also the origin of the triedra.

Simulations were conducted for scans of the incident electron beam in the x direction by steps of 3 nm. For each beam impact at each step, all the electrons which exit through the nanosphere / water film sample with an energy between 5 keV and 30 keV and diffused at angles between 20° and 47° were detected and counted. The results were expressed as the percentage (with respect to the total number of incident electrons) of collected electrons depending on the distance of the beam impact from the intersection I of the vertical z axis passing by the center O of the sphere, with the specimen surface (Figure III.4d). At each step all the electrons reaching the detector are detected as they create electron-hole pairs in the silicon diodes (~ 2700 pairs by each 10 keV electron incident on the detector), the resulting electrical charge being collected from the biased p-n junctions of the detector, which monitor the image display system. Such

profiles of collected electron percentage versus distance from I origin correspond to the variation of the intensity in the Wet-STEM images, i.e. to the image contrast profiles.

On Figure III.6 are displayed the contrast profiles simulated for the basic components of the ***nanovectors for tumoral therapies*** : spheres (radius = 100 nm) of PLLA or of PLLA with 2 % at Re on one hand and nanoparticles of magnetite with radius 5 nm on the other hand, in a water film of thickness z varying between 100 and 400 nm. The percentage of diffused electrons far away from the spheres or particles corresponds to that one by the water film. It can be seen that the contrast is mainly controlled by three parameters: the atomic number Z of the elements in the material which correlates with its electron scattering power, the mass of material per unit of volume (density of scattering atoms) and the thickness of material through which the electrons are scattered (number of scattering events). Hence the magnetite particle induce a bright contrast with respect to the water films whereas a PLLA sphere having a radius of 100 nm could not be distinguished from water without the presence of heavy atoms of Re. Our calculations (details not reported here) showed that a pure PLLA sphere should reach a radius of about 400 nm in a 800 nm thick water film to induce a slightly visible contrast.

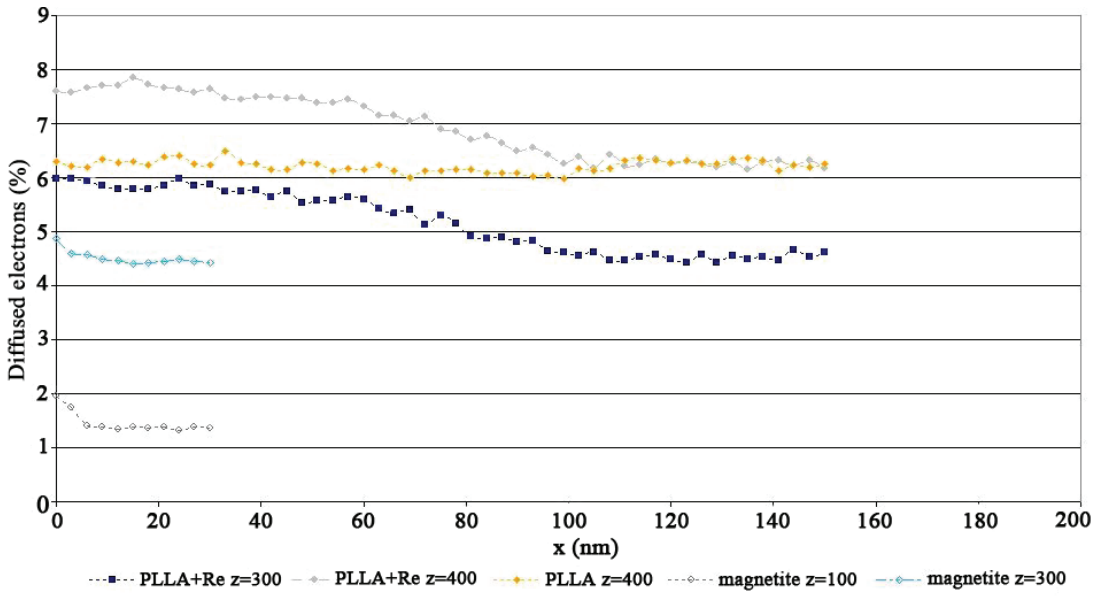

Figure III.6. Computer simulated profiles for a 5 nm radius magnetite sphere in a water film with 100 or 300 nm thickness and for 100 nm radius PLLA or PLLA /(2% at) Re spheres in a water film with 300 or 400 nm thickness.

On Figure III.7 is depicted the 3D model which was used to simulate the composite nanovector system: a sphere of PLLA / 2% at Re of radius 100 nm loaded with 112 magnetite

nanoparticles of radius 5 nm. In order to avoid prohibiting times for data input and calculation, the weight percentage of magnetite (hence the number of nanoparticles) was limited to 5%.

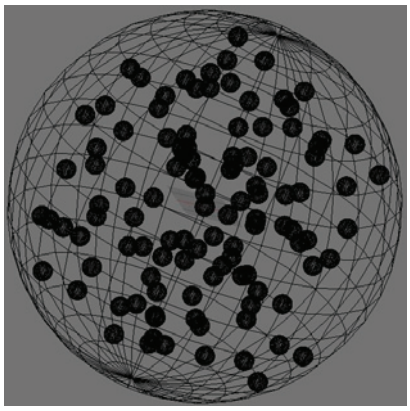

Figure III.7. The 3D model used to simulate the contrast of Wet-STEM images.

Figure III.8a to b displays the contrast profiles for the section y=0 of the model sphere or of the other spheres, depending on the thickness of the water film. Correspondingly, the inserts display the magnetite particles located in the corresponding slice y= 0 ±5 nm of the model sphere: these magnetite nanoparticles are the primary scattering centers with the largest Z for electrons travelling along or very close to the incident direction through the sphere. With respect to the background level due to the water film, the contrast of the model sphere clearly corresponds to a component due to the PLLA/Re matrix and to peaks due to the magnetite nanoparticles (see Figures 8a and b); the amplitude of those peaks can be of the same order of magnitude as the matrix component. Increasing the water thickness induces a diminution of the contrast of both components.

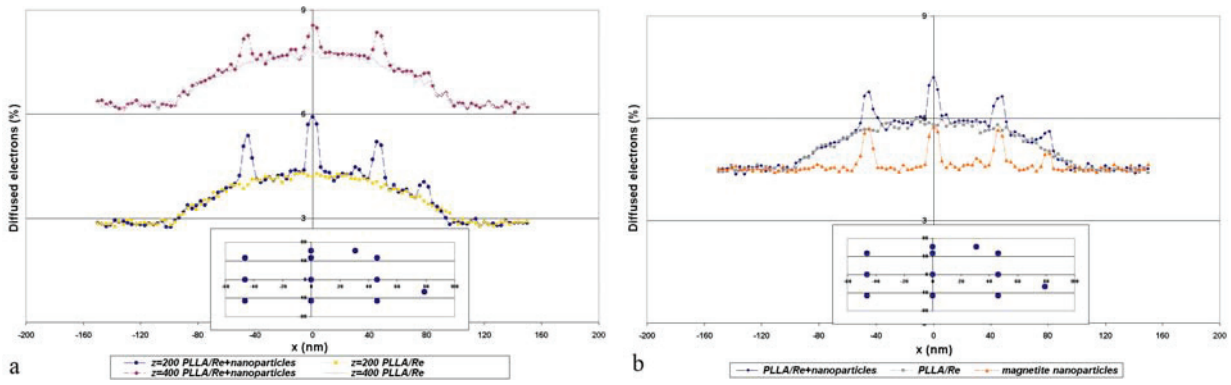

Figure III.8. Computer simulated profiles at section y=0 nm for the model sphere or for spheres with same diameter consisting of PLLA/Re only, or magnetite particles only, in a water film of which thickness can vary: 200 nm (a), 300 nm (b), 400 nm (a).

Figure III.9a and b displays profiles corresponding to other sections (y=-13 nm and y=-49nm) of the PLLA/Re model sphere (with inserts displaying magnetite particles located in the corresponding slices of the model sphere), in a water film with thickness of 300 nm.

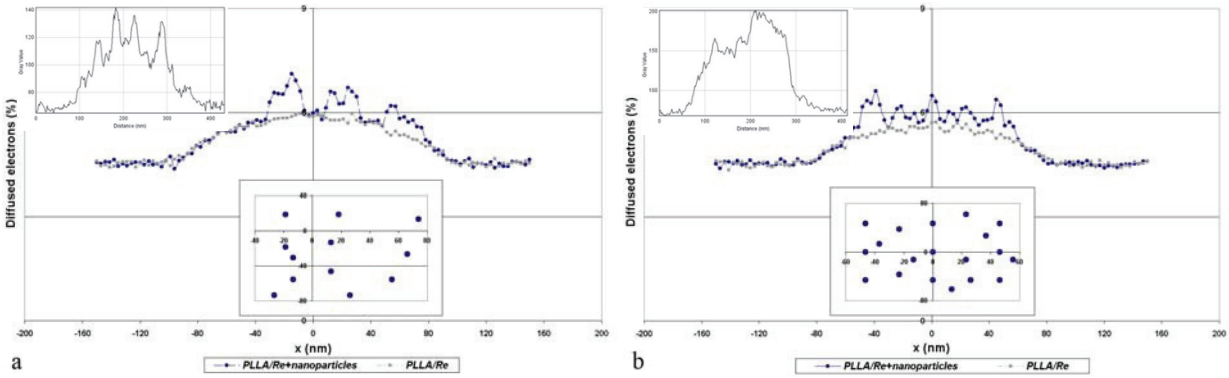

Figure III.9. Computer simulated profiles for a PLLA/Re or a PLLA/Re sphere loaded with magnetite nanoparticles in a water film with 300 nm thickness at sections y=-13 nm (a) and y=-49 nm (b) of the spheres. In inserts, the experimental profiles.

Indeed it is shown here that typical experimental profiles like A and B (Figure III.5) do agree with computer simulated ones: profile A appears consistent with the case of Figure III.8 whereas profile B displays features from cases a and b in Figure III.9, the thickness of the water film being likely about 300 nm. Of course it is extremely difficult for the model to match exactly the 3D spatial distribution of the magnetite particles of which the real weight percentage is closer to 10% than to 5%.

To assess further the resolution capabilities of this new mode with respect to smaller size systems the two types of ***MRI contrast agents*** M and M' were imaged as displayed in Figure III.10. For the corresponding Wet STEM images both overviews and enlargements are reproduced here. In the case of the suspension M (Figure III.10a) particles of mean size 5 nm (see the smallest bright spots in the enlargement insert) are seen well isolated whereas a flocculation effect is observed in the case of M' (Figure III.10b).

For comparison a TEM (bright field) image of M in dry environment (Figure III.10c) is reproduced showing the maghemite (iron oxide) cores whose the most probable size value is 5 nm. It can be thus concluded that such maghemite (iron oxide) nanoparticles with a size close to 5 nm can be detected in a water film of a few hundreds of nm thick. This is consistent with the fact that the 2 nm nominal resolution of the microscope is certainly lowered by the vibrations of the Peltier stage. According to these experimental data profiles for systems having a 5 or 10 nm

maghemite core in a 18 nm radius spherical envelop consisting of glucose have been simulated (Figure III.10d): as expected the glucose coverages made of light elements are not revealed, only the maghemite cores can be detected.

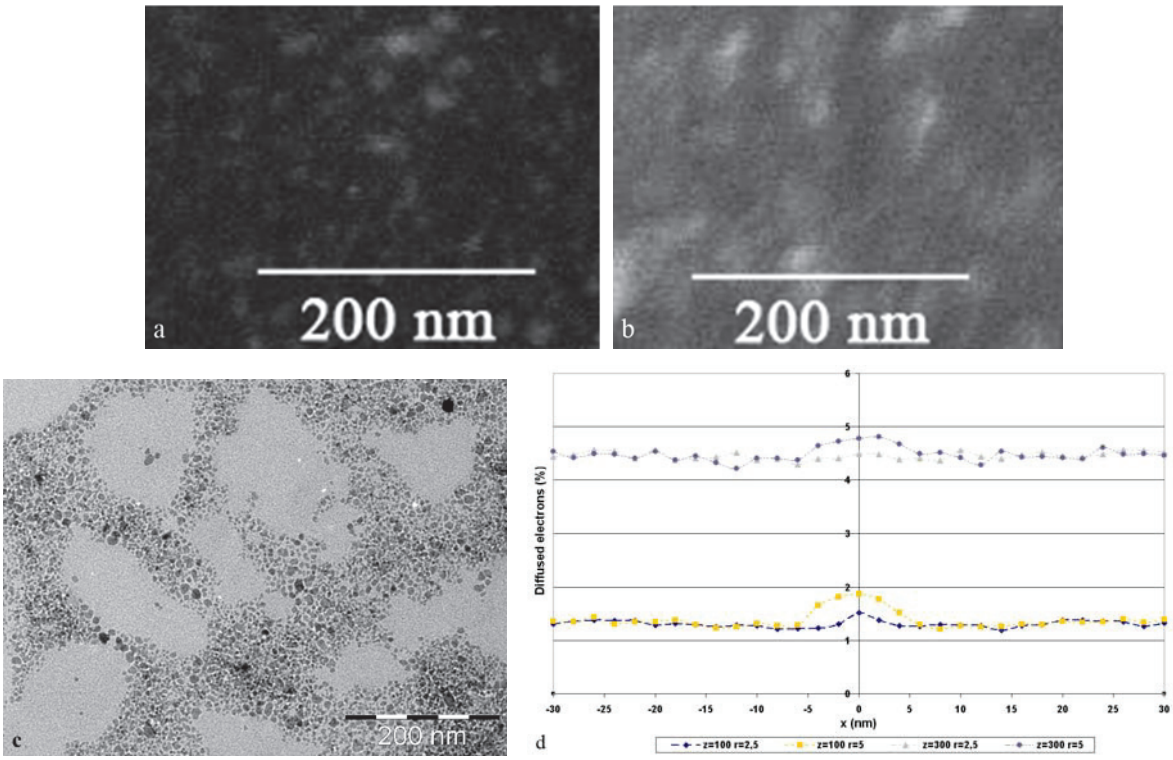

Figure III.10. Wet-STEM images (a, b) from the two agents M and M' with enlargements in inserts; TEM bright field image from M (c); simulated profiles for a 2.5 or 5 nm radius maghemite particle inside a 18 nm radius glucose coverage in a water film of 100 or 300 nm thickness.

Nevertheless differences in the collective behaviour of the agents likely due to differences in the chemical composition of the coverages can be clearly detected through the positions of the iron oxides cores.

References

[1] FLETCHER A.L., THIEL B.L., DONALD A.M., Amplification measurements of alternative imaging gases in environmental SEM, *J. Phys. D: Appl. Phys.,* 1997, 30, p. 2249 - 2257

[2] BOGNER A., THOLLET G., BASSET D., *et al.*, Wet STEM: A new development in environmental SEM for imaging nano-objects included in a liquid phase, *Ultramicroscopy*, 2005, 104, p. 290 - 301

[3] BOGNER A., JOUNEAU P.-H., THOLLET G., *et al.*, A history of scanning electron microscopy developments: Towards 'wet-STEM' imaging, *Micron*, 2006, 38, p. 390 – 402

[4] DONALD A.M., Environmental scanning electron microscopy for the study of 'wet' systems, *Current Opinion in Colloid & Interface Science*, 1998, 3, p. 143-147

[5] HAMOUDEH Misara, SALIM H., BARBOS Dumitru, *et al.*, Preparation and characterization of radioactive dirhenium decacarbonyl-loaded PLLA nanoparticles for radionuclide intra-tumoral therapy, *European Journal of Pharmaceutics and Biopharmaceutics*, 2007, 67, p. 597-611

[6] HAMOUDEH M., AL FARAJ A., CANET-SOULAS E., *et al.*, Elaboration of PLLA-based superparamagnetic nanoparticles : Characterization, magnetic behaviour study and in vitro relaxivity evaluation, *International Journal of Pharmaceutics*, 2007, 338, p. 248-257

CHAPTER IV

Introducing iron oxide contrast agents for MRI of atherotic inflammation

IV.1. Mortality by vascular inflammation and the atherotic plaque, its structure and development

Cardiovascular diseases (CVD) represent one of the most prominent health problems in the modern world. According to the World Health Organization, an estimated number of 17.1 million people died in 2004 from CVD i.e. 29% of the global rate of deaths, so that CVD represent the main cause of death globally. CVD are also the first cause of disability worldwide. The main source of CVD is atherosclerosis, a syndrome affecting arteries which leads to a thickening of the arterial wall thus by restricting the blood flow.

The first stage of atherosclerosis is the formation of the atheroma in the arterial wall. The atheroma or atherotic plaque develops with occurrence of several components: 1) connective tissue extracellular matrix (collagen, proteoglycans and fibronectine elastic fibbers); 2) phospholipids and crystalline cholesterol; 3) cells (macrophages, T-lymphocyte, smooth muscle cells); 4) thrombotic material with platelets and fibrin deposition.[1] These components are found in the intima, but can also appear in the media and adventice. Later evolution of the plaque takes place through the extension of the lipidic core and the accumulation of macrophages at the boarder of the plaque which leads to the formation of a fibrous cap which is the source of rupture.

The plaque starts with a dysfunction of the endothelium which is an autocrine and paracrine organ. Its role is to regulate the antiinflammatory, mitogenic and contractile activities of the blood vessel wall and the haemostatic processes in the vessel lumen. The molecule responsible for all these regulatory processes is the nitric oxide. Biomechanical shear forces enhanced by hypertension, hypercholesterolemia, circulatory vasoactive amines, immmunocomplexes, and chemical irritants in tobacco smoke are risk factors which can induce the dysfunction of the endothelium. Once the synthesis of the nitric oxide starts to diminish, the vessel wall penetration, the oxidation of the circulant lipoproteins, the proliferation of the smooth muscle cells, the monocyte penetration, the deposition of extracellular matrix are favoured.

Low-density lipoproteins (LDL) can penetrate the arterial endothelium until the intima. Oxidized LDL interact with the proteoglycans leading to retention of the lipoproteins and to LDL intravascular aggregation with chemical modifications. As a consequence inflammation is induced. The first response of the organism to inflammation is the innate immunity which relies on macrophages and dendritic cells. When the presence of oxidized LDL is detected by SR-A and CD-36 scavenger receptors, monocyte migration cycle and

formation of foam cells initiated by macrophages begin. The close smooth muscle cells are activated by the cytokines produced by the foam cells leading to extracellular formations and fibroses.

The presence of the proatherogenic environment thus favours the development of the plaque by increasing the monocyte chemotaxis which leads to the accumulation of lipids and the formation of the 'fibrous cap'. At this stage, the atherotic plaque consists of a large lipidic core, a small number of smooth muscle cells and the increased infiltration of macrophages. The media and adventitia tunica also suffer changes.

Clearly an efficient strategy against diseases induced by atheroma's occurrence relies on efficient diagnostic of the incipient stages of the plaque development. Among the non invasive techniques for diagnostic, MRI has this potentiality, especially if its detection efficiency is improved due to dedicated contrast agents.

To achieve such an approach, we took part in the collaborative research project INFLAM, dedicated to study vascular and cerebral inflammation and granted by the ANR French Research Agency. Hereafter is given the example of MRI examination of the atherotic aorta in a murine model for mice given a high-fat diet which favors occurrence and development of atheroma.

IV.2. MRI study of atherotic aorta in a murine model

In the frame of the INFLAM project, this study was conducted by Dr. M. Sigovan and Prof.E. Canet-Soulas (CREATIS LRMN Laboratory, Université Claude-Bernard)

IV.2.1. Animal model

A total number of 10 ApoE-/- mice (C57BL/6 background) received from GUERBET, France were used in the study. Animals were started on a high-fat diet (Western Diet, 0.5% cholique acid and 1.25% cholesterol) at 6 weeks of age. At 28 weeks of age, 8 out of the 10 animals were administered a dose of 1000 μmol Fe/kg of the P904 contrast agent. The two remaining animals were considered as the control group.

The MRI study was performed over 5 time points as follows: baseline (day 0/ control group) and Days 2, 20, 28 and 48 after administration of contrast agents. While under deep anesthesia, 2 mice per time point were sacrificed by cervical dislocation and samples of the ascending aorta were taken for microscopy sample preparation.

IV.2.2. MRI studies

Baseline MRI was performed on 5 randomly chosen animals. One mouse per time point underwent a second imaging session for the observation of the contrast induced by the accumulation of the contrast agent in the atherotic plaque. The MR imaging system was a 4.7 Tesla Bruker magnet (Bruker Biospin GmbH, Rheinstetten, Germany) equipped with a 10 cm bore actively-shielded and 250 mT/m gradient set. An in-house 'Alderman and Grant' emission-reception volume radio frequency (RF) coil (length=30 mm, inner diameter=26 mm) was used for good RF homogeneity over the volume of interest. Double cardiac and respiratory gated acquisitions were obtained with an in-house gating system developed with Matlab software. Three patch electrodes placed on the animal's paws were used to collect the ECG signal and a pressure sensor was used for the respiratory signal.

A bright-blood cine-mode FLASH sequence (Figure IV.1) was used for aortic arch localization, performed on 7 transverse joined slices centered on the base of the heart. These reference slices were acquired with a gradient echo (GE) sequence (TR/TE = 1R-R interval / 6.7 ms, field of view (FOV) = 3.8×3.8 cm, matrix = 256×256, bandwidth (BW) = 25 kHz, slice thickness = 1.11 mm, number of averages (NA) =1). The same FLASH sequence was then used in an oblique plane to obtain a slice right above the aortic sinus perpendicular to the vessel wall. The parameters for the FLASH sequence were as follows: TR/TE = 10/ 2.7 ms, FOV = 3×3 cm, matrix = 128×128, BW = 25 kHz, slice thickness = 1 mm, NA = 4.

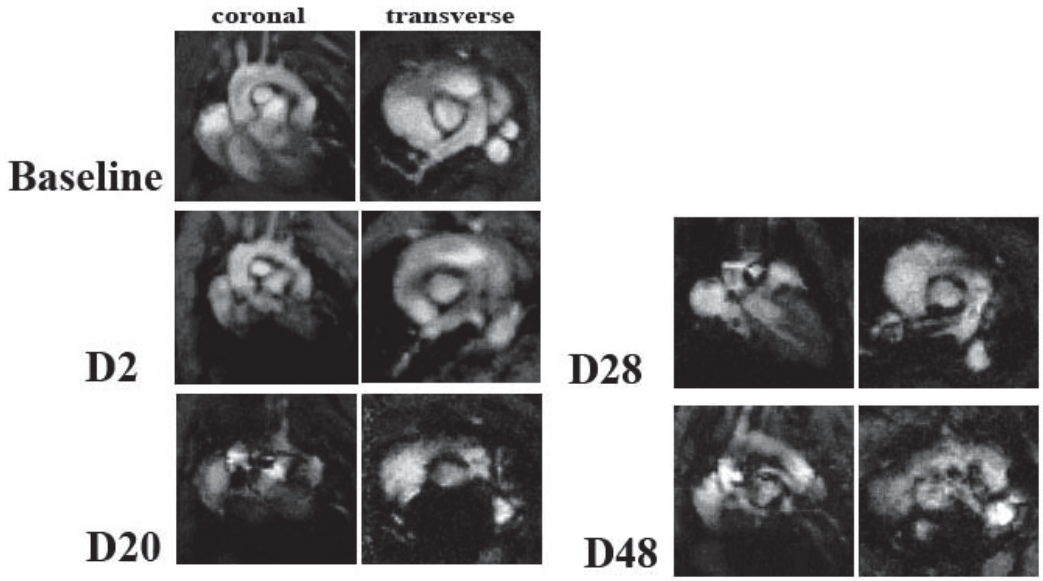

Figure IV.1. MR images from mouse's aorta, including coronal and transverse views, before (baseline) and and at differents Days (D) after injection of the P904 contrast agent.

All baseline MRI images clearly showed the aortic arch. Signal loss regions in the shape of "blooming artifacts" were identified around the bright lumen, in the aortic sinus, indicating focal accumulation of iron in the vessel wall. They were clearly visible at Days 2, 20 and 28 after particle administration, less visible at the last imaging point (Fig IV.2).

Considering the efficiency of the contrast agent for MRI examination of the atherotic plaque, one has to be concerned also with the consequences of the introduction and of the stay of the agents in the organism.

IV.3. Iron oxide contrast agents and iron metabolism

IV.3.1. Composition of studied agents

It is recalled that the P904 a contrast agent is currently developed by Guerbet SA, intended for the MRI detection of macrophages involved in inflammatory diseases [3]. It has a magnetic core of maghemite (γ-Fe_2O_3). Aminoalcohol derivative of glucose are grafted to the surface via phosphonate ligands. Both negative surface charges and steric hindrance ensure the colloidal stability of P904, with a hydrodynamic size of 23 – 25 nm.

IV.3.2. Iron cycles in the organism

Iron is a crucial element for the human organism. It plays a key role in vital biochemical activities. In the haemoglobin, it helps at the detection and transport of the oxygen and in the myoglobin at the storage and diffusion of the oxygen. It also plays an important role in the erythropoiesis and in the catalysis of certain enzymatic reaction.

For a healthy adult, the normal iron absorption is 1-2 mg/day [4]. This absorption compensates the losses by the skin and intestine cells desquamation. A dose of 30 mg of iron are necessary for the erythropoiesis daily.

The human body has an iron recycling mechanism: the reticuloendothelial macrophages ingest the red blood cells and eliminate the iron in the Fe^{2+} state through the ferroportin, Fe^{2+} which further is oxidized by ceruloplasmin and bound to the circulant transferrin. With this mechanism, around 25 mg of iron are recycled daily. The liver is the main organ that stores the excess iron in form of ferritin, hemosiderin and free iron pool. Most of this iron is ferric tied by citrate or adenosine diphosphate. The rest of the iron is ferrous and it is responsible for oxidation-reduction and Fenton reactions.

At the duodenum level, the iron Fe^{2+} reduced from Fe^{3+} by duodenal cytochrome B (Dcytb), a reductase enzyme of the cell`s membrane, is transported into the cell with the aid of the divalent metal transporter 1 (DMT1) [5]. When exiting the cell, the iron Fe^{2+} is transported through the membrane by ferroportin and transformed by hephaestin into Fe^{3+} state which is bound to the plasma transferrin.

In healthy adult male organism (in the developed countries), there are 3-5 grams of iron. A dose of 2 to 3.3 grams is stored in the red cells, 0.5 to 1 gram stored as ferritin and hemosiderin, 400 mg are used to store the oxygen and take part in the redox reactions, 3-4 mgs are contained by the plasma, bound to the transferrin.

IV.3.3. Iron containing species

IV.3.3.1. Haemoproteins

Haemoproteins are a group of iron containing species which contains at least one haem prosthetic group, an iron atom at the centre of a large heterocyclic organic ring called porphyrin. The haemoproteins are involved in the transportation of gases, chemical catalysis and electron transfer. They are divided in: haemoglobins, myoglobins and cytoshromes [6]. Most of the body iron is contained in haemoglobins.

Haemoglobin is a protein found in erythrocytes. Its role is to bind and transport the oxygen from the lung to the peripheral tissues and to transport the CO_2 in the opposite direction. Most of the haemoglobins contain iron in ferrous state (Fe^{2+}), but there ones where iron is in ferric state (Fe^{3+}). The magnetic properties of the haemoglobins are affected by the chemical coordination of iron. If the haemoglobins bound oxygen (oxyhaemoglobin), it exhibit a diamagnetic behaviour, while, in the case when do not bound oxygen (deoxyhaemoglobin), it exhibit a paramagnetic behaviour.

Myoglobins, a family of haemoproteins mainly found in muscle tissues, contain one haem prosthetic group and represent an intracellular storage site for oxygen. Like the haemoglobins, the binding of oxygen to the iron atom influences the magnetic behaviour.

Cytochromes are a group of haemoproteins acting for electron transport.

IV.3.3.2. Other iron containg species

A. Ferritins

The ferritin is an iron storage protein. It consists of 24 sub-units of heavy polypeptide Ft-H (MW≈21 kDa) and of light polypeptide Ft-L (MW≈19 kDa), and of an iron core [3]. The structure without the core is called apoferritin (Figure IV.2). The inner diameter is 5-7 nm and the outer diameter is 12-14 nm. The ferritin is found in the liver, spleen, bone marrow and blood (serum ferritin), scattered in the cytoplasm and in the lysosomal bodies.[7] The heavy polypeptide is a catalyst for the oxidation of Fe^{3+} and the light polypeptide facilitates the mineralisation of the iron core. The ferritin is soluble in water.

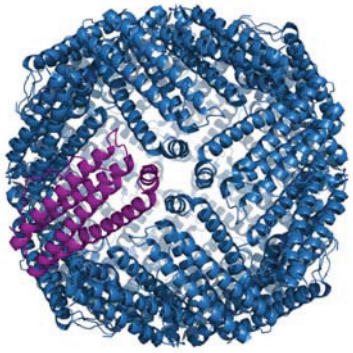

Figure IV.2. Structure of apoferritin.

The iron core can be crystallized in the following structures [8, 9]:

- Hexagonal ferrihydrite with the lattice parameters a=0.508 nm, c=0.94 nm;
- Fcc structure with parameter a=0.43 nm;
- Haematite with the lattice spacings in the range 0.361-0.374, 0.269, 0.184-0.189 nm;
- Iron oxides: Magnetite (Fe_3O_4) or Maghemite (γ-Fe_2O_3);
- Disordered structure with large density of stacking faults.

The core contains one crystallite or a few smaller crystallites, all with the same crystalline phase.

B. Transferrin

Transferrins (Tf) (Figure IV.3) form a family of proteins (serum transferrin, lactoferrin, melanotransferrin) [10] whose role is controlling the iron concentration in the body fluids to ensure an antibiotic effect.

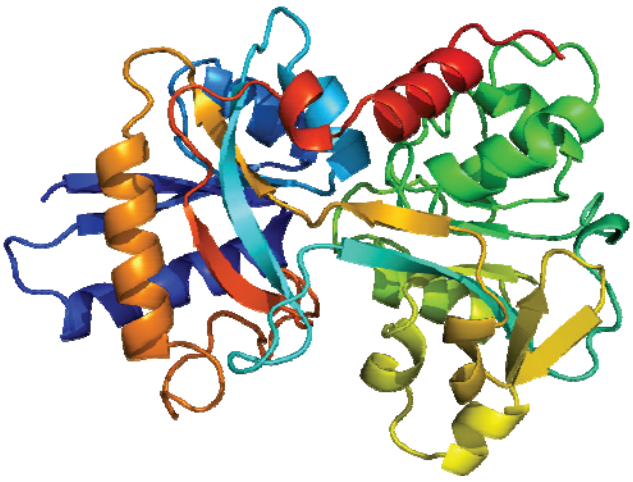

Figure IV.3. The structure of apo-transferrin.

The most abundant member of this family in the human body is the serum transferrin (siderophilin), whose role is binding and transporting the iron from the absorption site (intestinal mucosa) to the cells. At the extracellular pH of 7.4, one or two ferric (Fe^{3+}) ions can be bounded to the transferrin [11]. A transferrin receptor (TfR) is involved to ensure the endocytose of transferrin by the cell. The iron is released due to the acidic pH of the endosomal lumen and the complex Tf – TfR is returned to the cell surface where it dissociates.

C. Haemosiderin

The haemosiderin is an insoluble iron storage system which is mainly a derivative product from the lysosomale degradation of ferritin (MW≈12.9 ÷ 17.8 kDa). It is founded in the cells of the reticular-endothelial system, in the cytoplasm of the macrophages (then called siderophage) and in special cells (epithelial – hepatocyte or conjunctive – cardiomyocyte).

D. Non transferrin bound iron

Non transferrin bound iron represent the serum iron which is not associated to transferrin, serum ferritin or haemoglobins. It has a heterogeneous composition which makes it highly toxic, in some cases, leading to the possible generation of free radicals.

IV.3.3.3. Iron oxides and oxyhydroxides

Mineralised iron found in biological systems is in the form of iron oxides or oxyhydroxides. They exhibit different magnetic behaviours depending on the crystalline structure. A list of the iron oxides and oxyhydroxides with their characteristic magnetic behaviour is summarized in Table IV.1.

Mineral	Formula	Magnetic behaviour	Biological occurence
Goethite	α-FeOOH	Antiferromagnetic	Limpets Human (liver)
Lepidocrocite	γ-FeOOH	Antiferromagnetic	Sponges Chitons
Ferrihydrite	$Fe_5HO_8 \cdot 4H_2O$	Speromagnetic	Ferritin Chitons
Haematite	α-Fe_2O_3	Antiferromagnetic or weakly ferromagnetic	Ferritin
Magnetite	Fe_3O_4	Ferrimagnetic	Ferritin
Maghemite	γ-Fe_2O_3	Ferrimagnetic	Ferritin
Wüstite	FeO	Antiferromagnetic	Ferritin

Table IV.1. Forms of mineralised iron.

References:

[1] FUSTER V., MORENO P.R., FAYAD Z.A., *et al.*, Atherothrombosis and High-Risk Plaque Part I: Evolving Concepts, Journal of the American College of Cardiology 2005, 46 (6), p. 937–954.

[2] SANZ J., FAYAD Z.A., Imaging of atherosclerotic cardiovascular disease, 2008, Nature, 451, p. 953 - 957

[3] SIGOVAN M., BOUSSEL L., SULAIMAN A., *et al.*, Rapid-clearance iron nanoparticles for inflammation imaging of atherosclerotic plaque: initial experience in animal model, *Radiology*, 2009, 252, p. 401-409.

[4] PAPANIKOLAOU G., PANTOPOULOS K., Iron metabolism and toxicity, *Toxicology and Applied Pharmacology,* 2005, 202, p. 199–211

[5] BEAUMONT C., Mécanismes moléculaires de l'homéostasie du fer, *Medecine/Sciences*, 2004, 20, p. 68-72

[6] CRICHTON R., Inorganic Biochemistry of Iron Metabolism, From molecular mechanisms to clinical consequences, 2001, John Wiley & Sons, LTD

[7] COWLEY J.M., JANNEY D.E., GERKIN R.C., BUSECK P.R., The Structure of Ferritin Cores Determined by Electron Nanodiffraction, *Journal of Structural Biology*, 2000, 131 p. 210-216

[8] QUINTANA C., BELLEFQIH S., LAVAL J.Y., *et al.*, Study of the localization of iron, ferritin, and hemosiderin in Alzheimer's disease hippocampus by analytical microscopy at the subcellular level, *Journal of Structural Biology*, 2006, 153, p. 42-54

[9] QUINTANA C., COWLEY J.M., MARHIC C., Electron nanodiffraction and high-resolution electron microscopy studies of the structure and composition of physiological and pathological ferritin, *Journal of Structural Biology*, 2004, 147, p. 166-78

[10] *Protein Data Bank, Research Collaboratory for Structural Bioinformatics, Rutgers University, New Brunswick, NJ (http://www.rcsb.org/)*

[11] CHENG Y., ZAK O., AISEN P., *et al.*, Structure of the human transferrin receptor-transferrin complex, *Cell*, 2004, 116, p. 565–76

CHAPTER V

Aging of the contrast agents in an acidic medium to investigate their degradability in a model of lysosomal environment

V.1. Lysosomal metabolism and simulation by aging in acidic medium

In order to process the foreign substances (iron oxide nanoparticles in our case), the cells must internalize them through the endocytosis pathway. The endocytosis is the process by which the cells internalise the substances which cannot pass through the cell membrane. The Figure V.1 illustrates the stages by which magnetic nanoparticles are internalized [1]. At first, small clusters are formed after the accumulation of magnetic nanoparticles at the vicinity of the cell membrane. The membrane surrounds the clusters forming the so called "early endosomes" (* in the Figure), which are up to 1 μm in diameter and correspond to a moderate acid pH medium. Several early endosomes can fuse to form a "late endosome" (**) which has an acidic environment (approx. pH 5.5). These endosomes fuse with the last compartment of the endocytic pathway, the lysosomes (#). These are larger vacuoles (approx. diameter 1-2 μm) with a pH around 4.8. Their role is to digest the waste substances (dying cells, microbes, larger extracellular material).

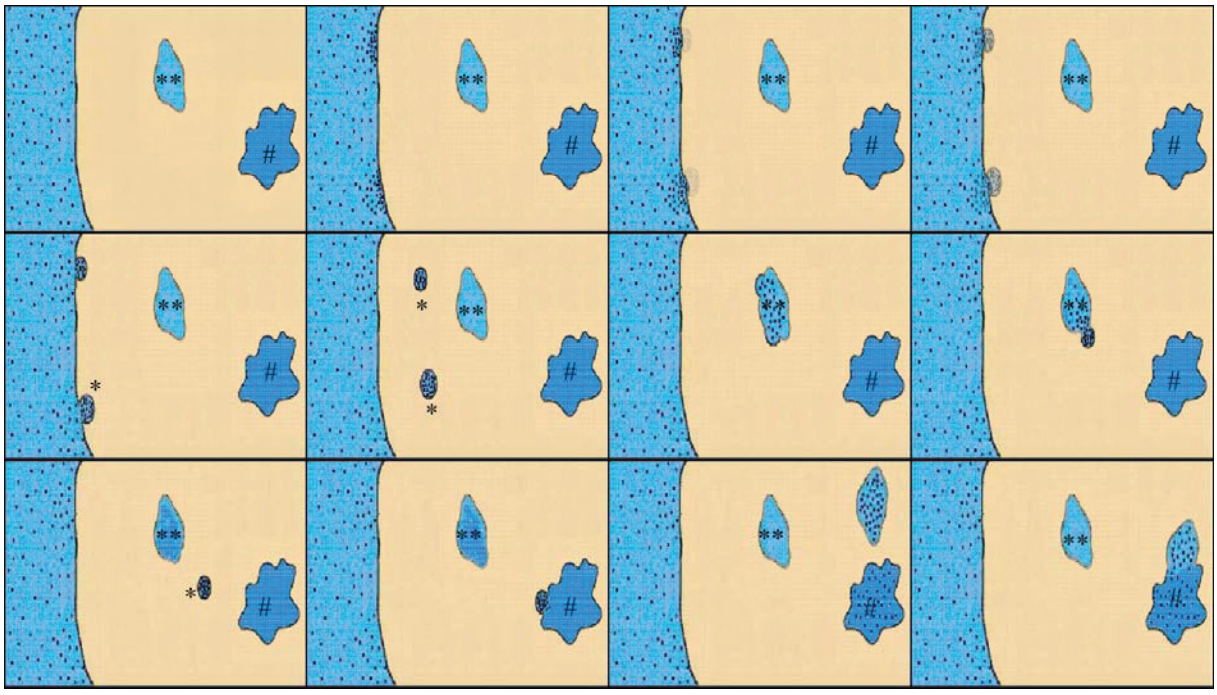

Figure V.1. Schematic illustration of the internalisation by phagocytosis.

As an example, reproduced in Figure V.2, all these stages for the internalisation of AMNP iron oxide nanoparticles in mesenchymal stem cells (MSC) have been observed during one of our TEM studies.

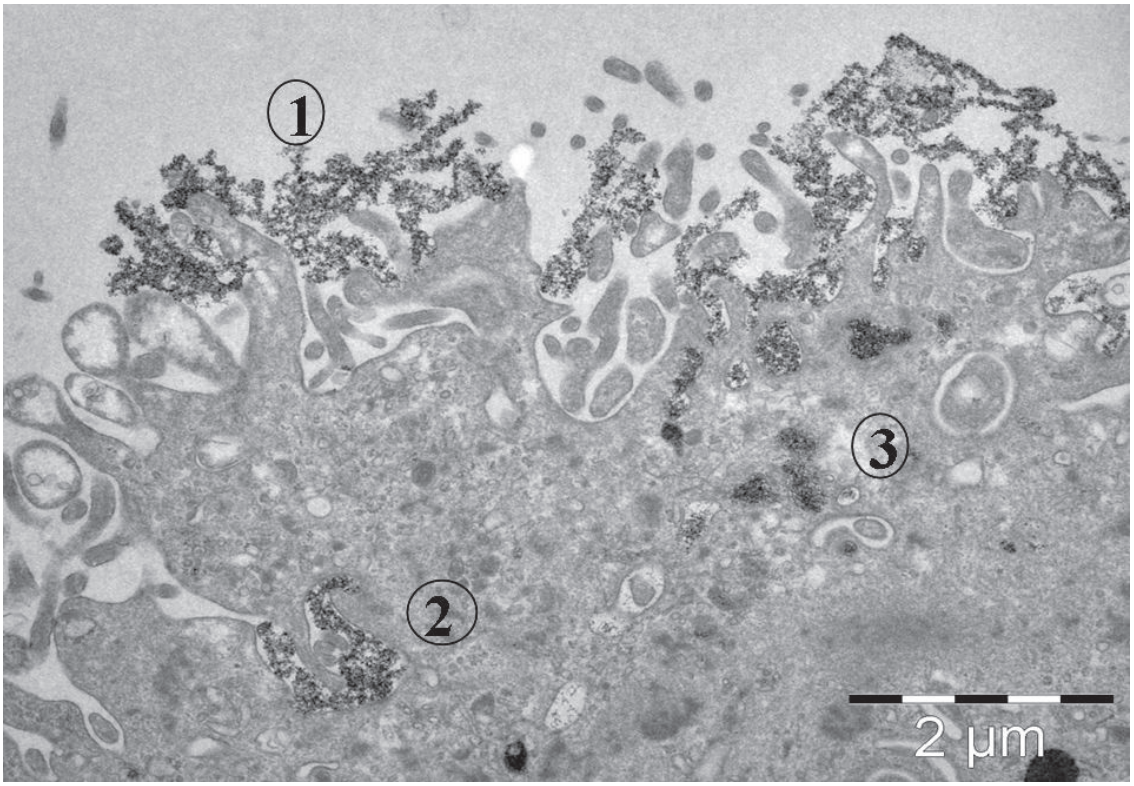

Figure V.2. CTEM image showing the different stages of cell internalisation for AMNP nanoparticles in MSC's.

As described in chapter IV, the iron metabolism displays different stages in order that the organism can maintain a physiological level of labile iron and store the excess iron for cellular requirements [2]. Due to this fact, iron oxide nanoparticles are proved to be less toxic than other inorganic crystals and they have greater chances of being transformed and degraded by cellular homeostasis [3, 4]. The resident and circulating macrophages are the first cells that capture the injected iron oxide nanoparticles [5], but the nanoparticles can be internalized *in vivo* by any cell type following the endocytosis pathways and they are confined into lysosomes [6].

So the contrast agent nanoparticles get confined in the lysosomes where they are exposed to the combined effect of acidic pH, lysosomal hydrolases and eventually iron chelators involved in iron regulation, but the mechanism and time course of nanoparticle degradation are unknown. The purpose of our study achieved in the frame of the INFLAM project was thus to monitor the physical state of magnetic nanoparticles in an acidic medium mimicking the lysosomal environment. The different iron oxide nanoparticles having rather similar magnetic cores different surface coatings were exposed to media of variable acidity supplemented with citrate as iron chelator [7]: these media were chosen to mimick the lysosomal environment as first proposed by Arbab et al. [8]. As pointed out by this author, it

has been stated in literature that the transport of iron from the endosome into the cytosol is accomplished by binding of the iron to various low-molecular weight compounds (citrate, isocitrate). It is thought that these dicarboxylic acid chelates form complexes with the free iron.

Several complementary methods were used to investigate the degradation course. The morphological and structural characteristics of the nanoparticles were investigated by TEM throughout the degradation course. SQUID magnetic measurements and ferromagnetic resonance (FMR) allowed the quantification of the magnetization decrease in the acidic suspensions and the assessment of the size distribution of the nanoparticles under degradation [7]. The quantification of the amount of iron released by the nanoparticles upon degradation was achieved with UV-visible absorption spectrometry [7].

V.2. Morphological and structural TEM studies

For the TEM study, drops (5 μl) were extracted from the different nanoparticle suspensions at different times in the buffer medium. The drops were deposited on TEM grids covered with holey carbon films and allowed to dry for several minutes before introduction into the electron microscope. A TOPCON EM 002B microscope operated at 200 kV was used in the conventional (C) bright field (BF) or high resolution (HR), with 0.18 nm spatial resolution, imaging modes as well as in the electron diffraction mode to assess the crystallographic structure of the nanoparticles. CBF overview pictures were analyzed using standard image processing software packages to determine the size distribution of the nanoparticles (apparent diameters from 2D measurements). In the HR imaging mode the crystal lattice of the particles could be directly visualized at magnifications larger than 300.000×.

V.2.1. Characterization of the nanoparticles before aging

The morphology and crystalline structure of the nanoparticles in their initial state before aging was revealed by combination of CTEM, electron diffraction and HRTEM, as reproduced in Figure V.3 a to c for the three families: Sinerem, AMNP and P904. The core of AMNP and P904 has the maghemite structure (display the electron diffraction pattern from P 904 especially at high magnification) whereas the core structure of Sinerem is magnetite.

Log normal fit of the size distributions measured by CTEM gave the following values for the median diameters: 6.8, 8.5 and 6.7 nm for Sinerem, AMNP and P904 respectively.

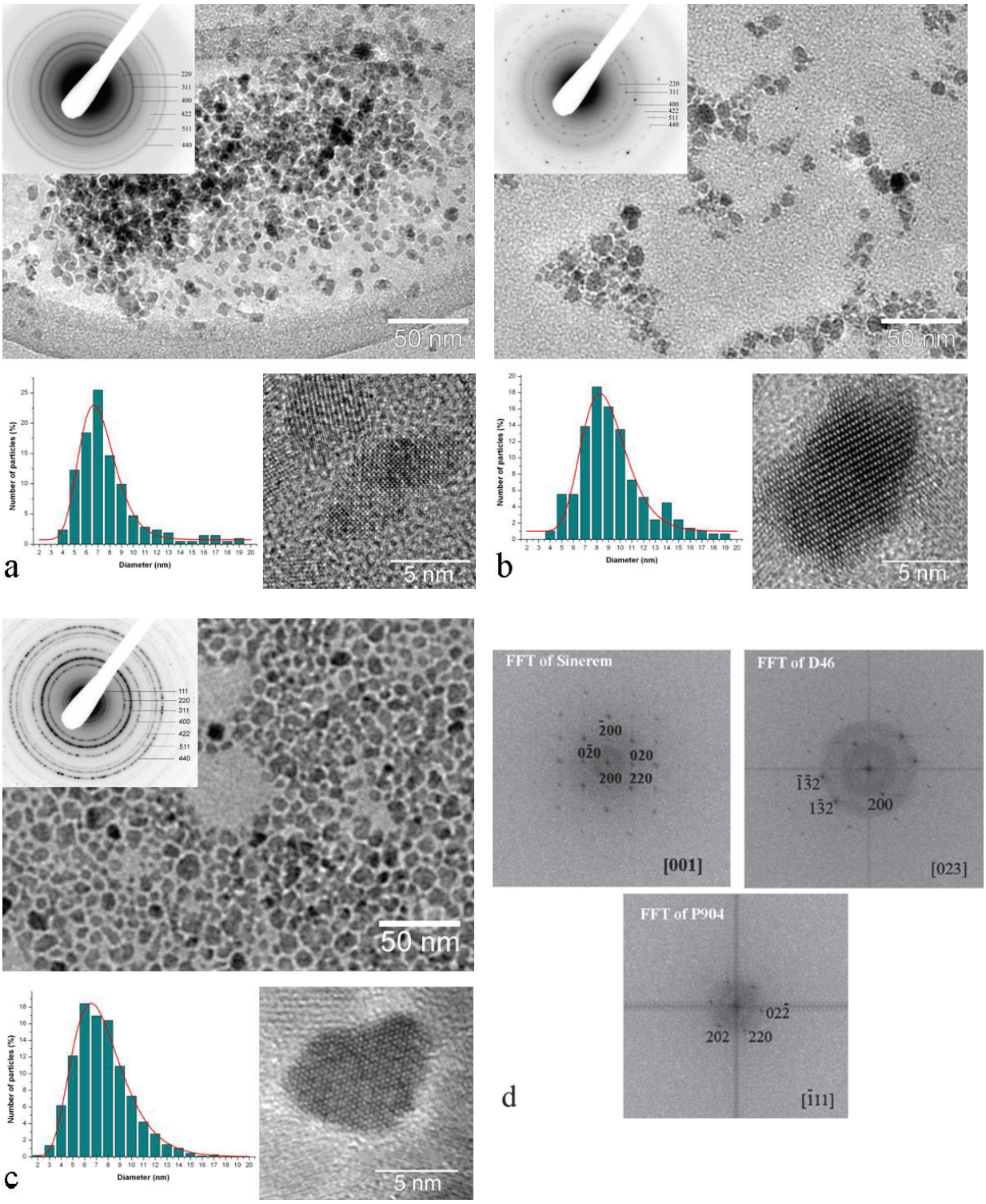

Figure V.3. Morphology, size distribution and crystalline structure of initial Sinerem (a), AMNP (b) and P904 (c) as determined by CTEM, electron diffraction and HRTEM , with FFT of the HRTEM images confirming the crystal structure and revealing the orientation of the nanoparticles imaged (particle in the center of the HRTEM image for Sinerem).

These results are consistent with those from measurements of magnetic properties conducted by M. LEVY and Dr. F. GAZEAU (Laboratoire Matière et Systèmes Complexes, Universiité Paris Diderot) and reported in Figure V.4.

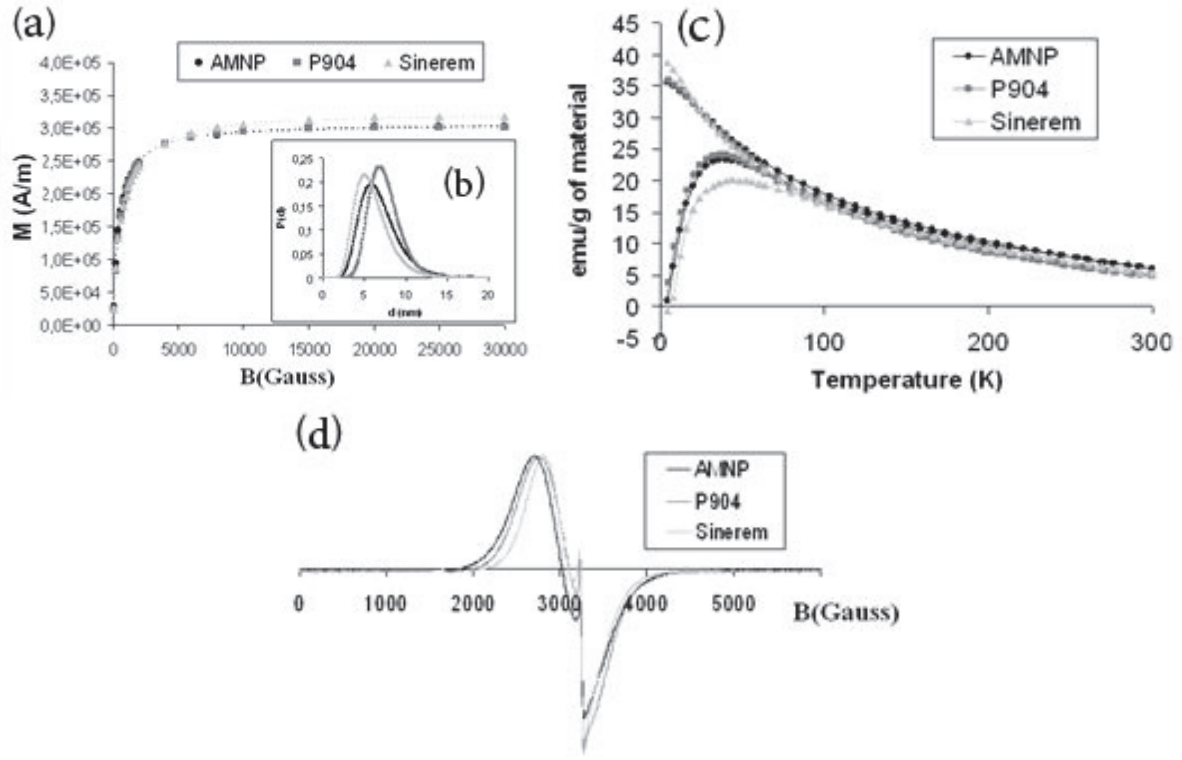

Figure V.4. Magnetic properties of initial nanoparticles. (a) Magnetization curve, (b) particles size distributions deduced from the fit of magnetization curves, (c) temperature dependency of the field cooled (FC) and zero field cooled (ZFC) magnetization, (d) FMR spectrum at room.

The initial AMNP and P904 present closed magnetization curves at room temperature (Figure V.4a), while Sinerem has a slightly higher saturation magnetization. Using a Langevin function, the magnetization curves were fitted and the theoretical curves superposed the experimental ones for the following values of the characteristic diameter: d_0 = 5.7 nm (Sinerem), d_0 = 7.2 nm (P904), d_0 = 6.5 nm (AMNP). These results are compared TEM determinations in Table I. Field cooled (FC) and zero field cooled (ZFC) magnetization curves are similar for the three types of nanoparticles (Figure V.4c). The determined blocking temperatures for studied nanoparticles were: 44 K (Sinerem), 36 K (P904) and 40 K (AMNP). All three FMR spectra (Figure V.4d) present a wide line centered around 3000 G and a narrow line at 3300 G.

V.2.2. Follow up of aging

To study the aging of the contrast agent in an acidic environment, the nanoparticles were left to degrade at room temperature up to 53 days in different solutions: 20 mM citric acid at pH 2.4 or in citrate buffers of different concentrations and pH (20 mM citrate at pH 3, 4 or 4.7, and 50 mM citrate at pH 3.5). The citrate buffers were prepared by mixing appropriate volumes of 25 mM or 50 mM aqueous solutions of citric acid ($C_6H_8O_7$, Fluka, >99.5%) and sodium citrate monobasic ($C_6H_7NaO_7$, Fluka, >99.5%) or sodium citrate monobasic and sodium citrate dibasic ($C_6H_6Na_2O_7 \cdot 5H_2O$ Fluka, >99%) to achieve the final desired pH. The final iron concentration was 1 or 10 mM.

The P904 agent and the AMNP having closely similar core, the TEM study was restricted to Sinerem and AMNP. CTEM, electron diffraction and HRTEM show that after 9 and 30 days in the acidic environment, the morphological and structural characteristics of the nanoparticles remained basically unchanged (Figure V.5 and V.6). After 30 days at pH = 4, the mean diameter had slightly decreased in the case of AMNP (Figure V.7), but remained constant in the case of Sinerem. Such results for the nanoparticle sizes were confirmed by the FMR spectra. The core of the nanoparticles remained well crystallized in the crystalline spinel lattice of the maghemite/magnetite according to the electron diffraction patterns and HRTEM micrographs.

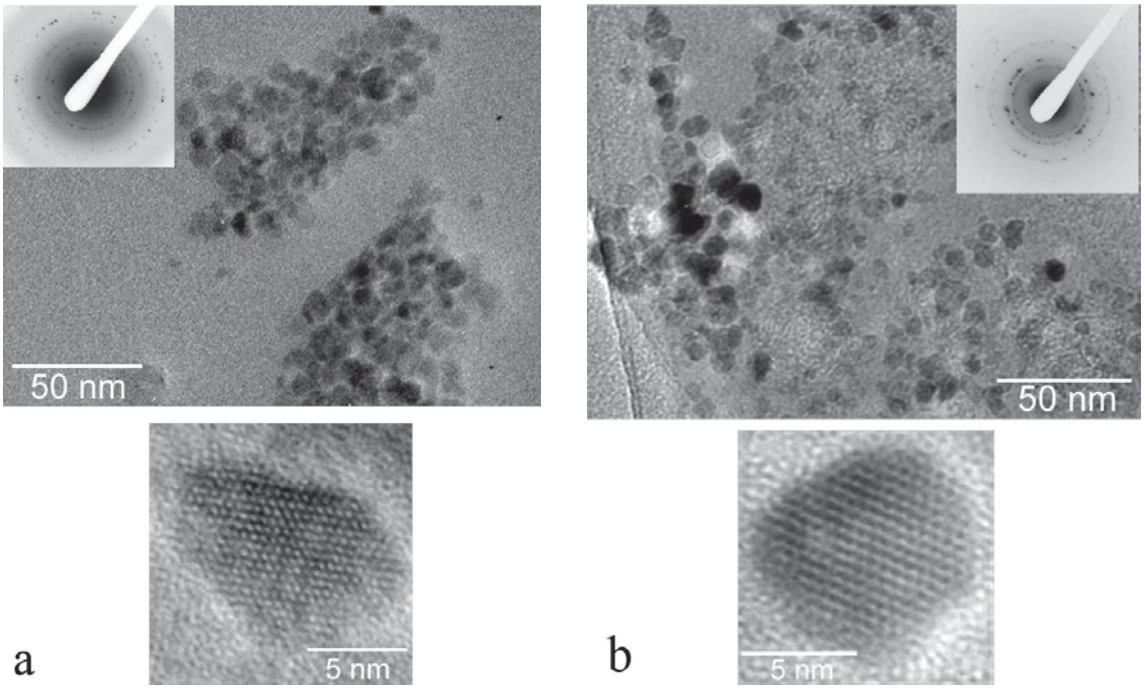

Figure V.5. Evolution of the morphology and of the crystalline structure of AMNP at D9 (a) and D30 (b) in pH = 4 citrate buffer.

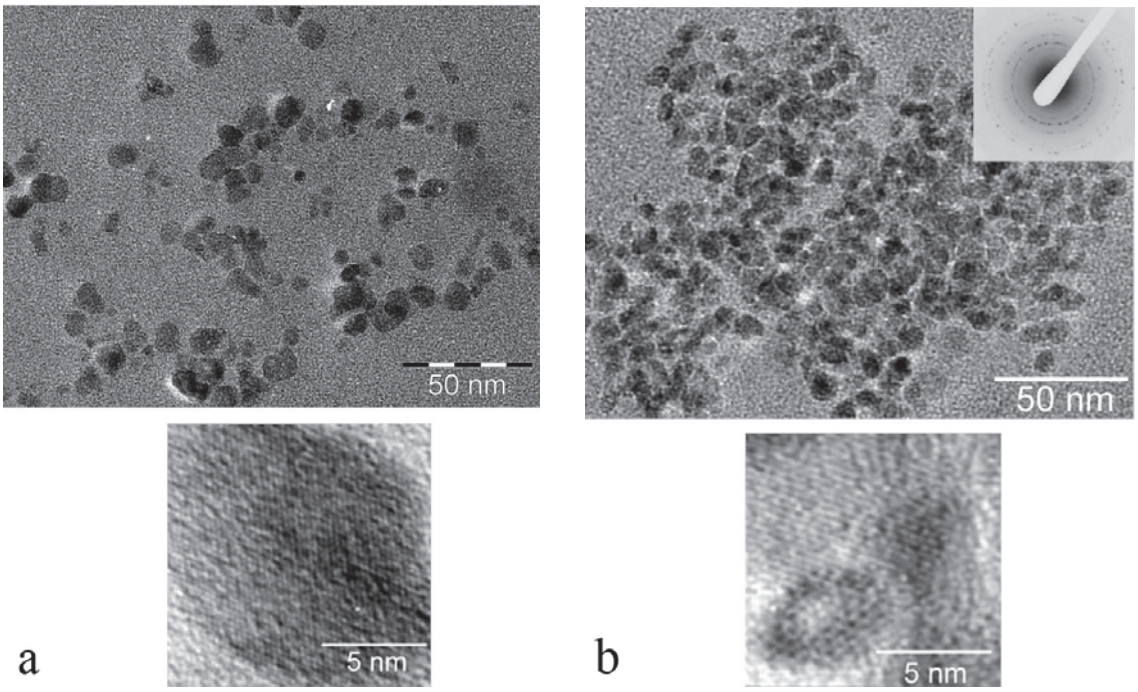

Figure V.6. Evolution of the morphology and of the crystalline structure of Sinerem contrast agent at D9 (a) and D30 (b) in the pH = 4 citrate buffer.

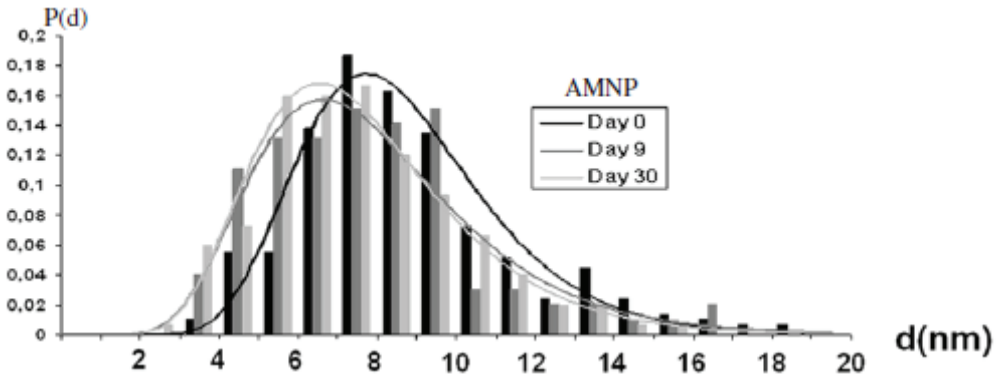

Figure V.7. Size distribution for the AMNP nanoparticles at different times in pH = 4 citrate buffer.

V.3. Follow-up of degradation by spectroscopies and discussion

The total iron released by the nanoparticles upon degradation was quantified by UV-visible absorption spectrometry after the reduction of Fe(III)–Fe(II) by ascorbate and the formation of a red complex between Fe(II) and phenanthroline: these investigations were conducted by Dr. F. Lagarde (Laboratoire des Sciences Analityques, Universite Claude Bernard Lyon) for the INFLAM project.

The colour of the solutions change their with time at all the pH values (Figure V.8), from reddish-brown (typical for maghemite solution) or brown (for magnetite) to yellow, which denote more free Fe(III) ions in the solution.

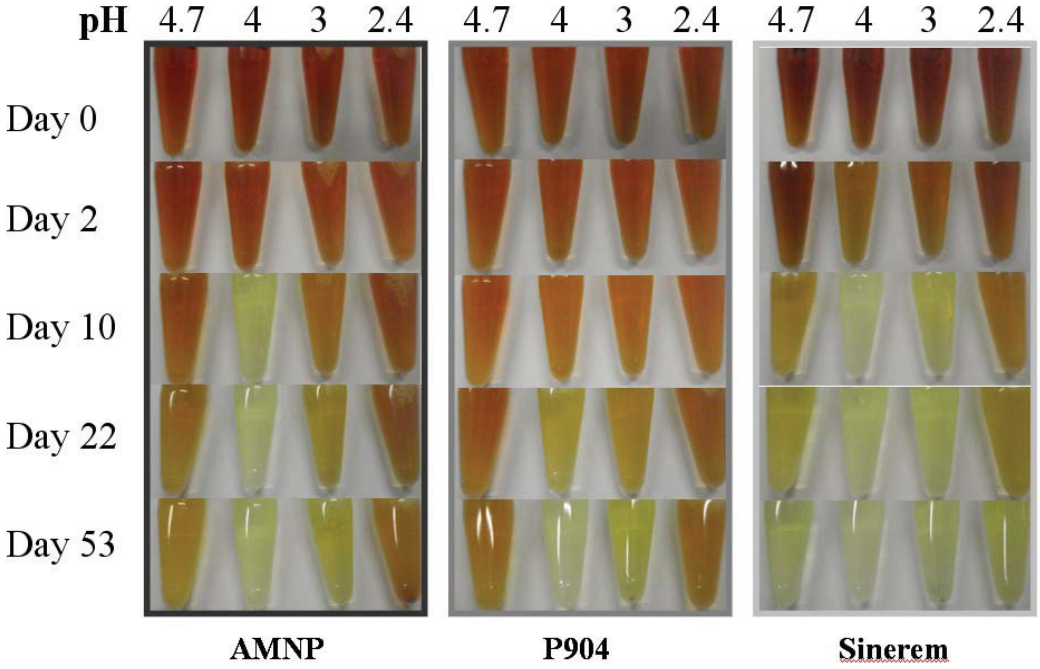

Figure V.8. Visual follow-up of iron oxide degradation in the acidic medium with citrate chelate.

Two complementary techniques, FMR which characterize the solid part of the suspensions and UV-visible absorption spectroscopy which characterize the liquid phase, confirm the visual observations. Since the released free iron species (Fe^{3+} and Fe^{2+} ions) do not present a ferromagnetic order, the FMR spectra are directly related with the mass of the ferromagnetic **crystals** remaining in suspension (Figure V.9.a). The free iron species released in the suspensions can be characterized by a colorimetric method after complexation with phenanthroline (Figure V.9.b).

The consistent results obtained by these two methods show that the degradation rate independently of pH follows the order: Sinerem > AMNP > P904 and that the degradation rate regardless of the type of nanoparticles follows the order: pH 4 > pH 3 > pH 4.7 > pH 2.

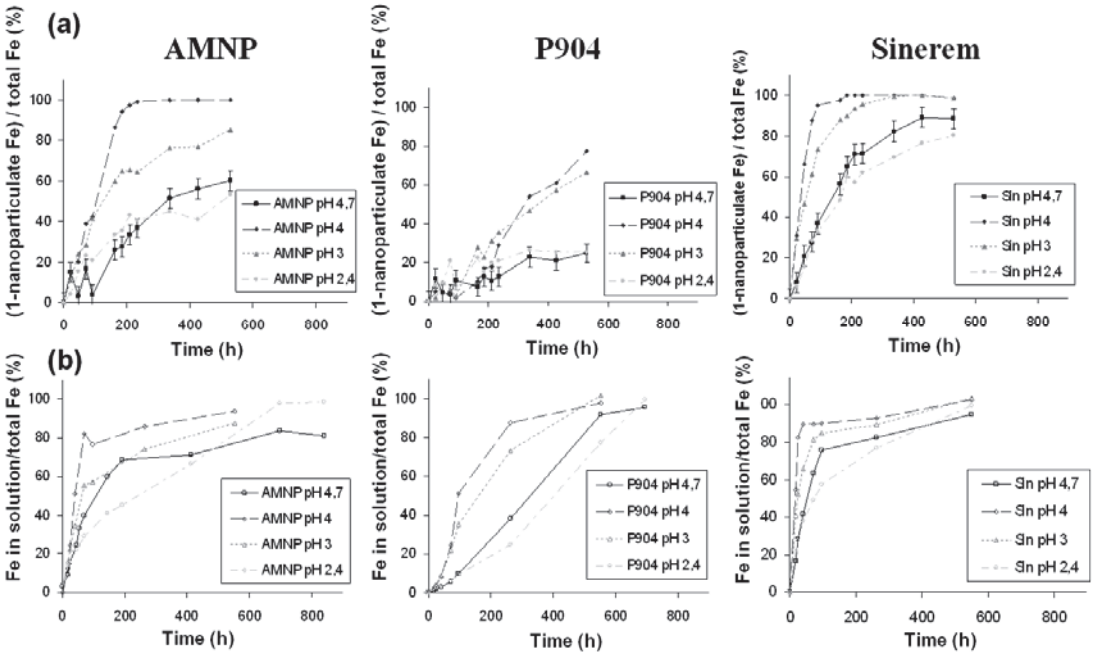

Figure V.9. Time and pH dependencies of iron oxide nanoparticles concentration determined by FMR measurements (a) and of free iron species (Fe(II) and Fe(III)) released from iron oxide nanoparticles, quantified by UV-visible spectrometry.

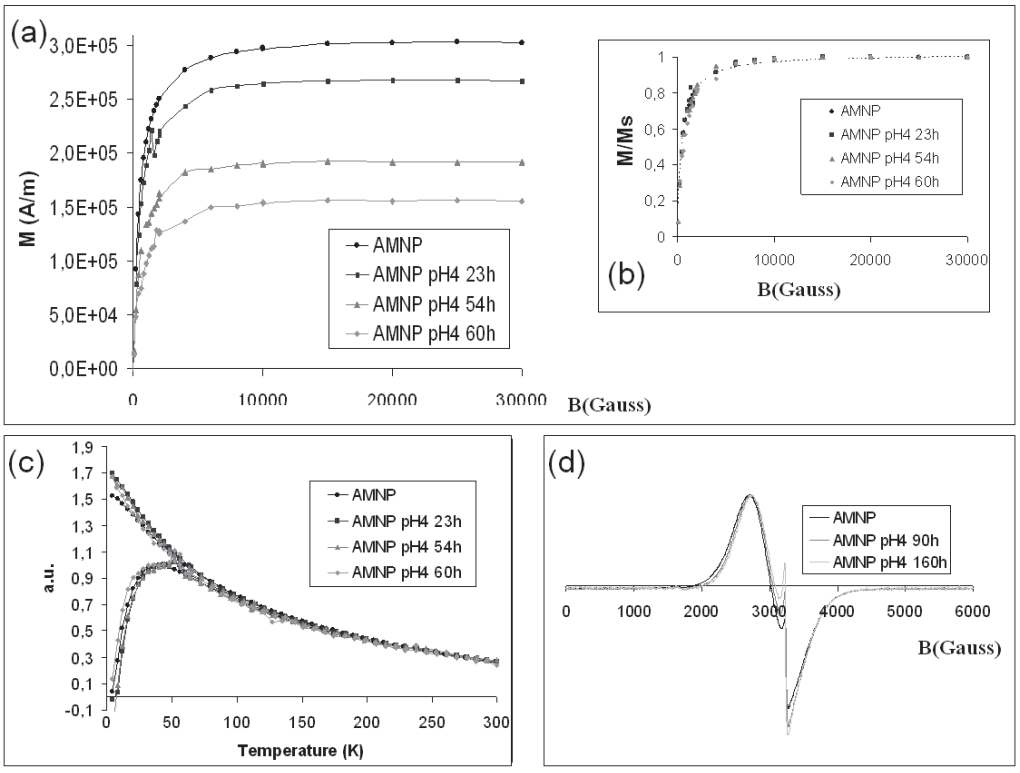

Figure V.10. Follow up of the AMNP magnetic properties throughout degradation at pH = 4 citrate buffer: (a) magnetization curves; (b) superimposition of the normalized magnetization curves; (c) temperature dependency of the FC/ZFC magnetization; (d) FMR spectrum.

The total magnetization of the AMNP suspension decreases with time at pH4 (Figure V.10.a), while the magnetization curves normalized to the saturation magnetization superimpose with time (Figure V.10.b). The blocking temperature deduced from the FC / ZFC curves remains unchanged in time (Figure V.10.c). These results indicate that the size of the remaining nanoparticles doesn't suffer significantly changes during degradation.

This study shows that there are different kinetics for the degradation but controlled by the pH value and the coating of the nanoparticles.

A non-intuitive result of the magnetic measurements, well corroborated by TEM analysis, is that the nanoparticle structure and size distribution do not change in the course of the degradation despite the release of free iron ions. This finding is evidenced by three independent characterizations - magnetization curve, FC/ZFC curves and FMR spectra. While the magnetic properties (per particle) remain unchanged, the global magnetization of the suspension actually decreases because of the dissolution of some nanoparticles. This suggests a peculiar mechanism of degradation, where the nanoparticles first attacked by the citrate iron ligand will completely dissolve, whereas other nanoparticles will remain structurally intact, as confirmed by HRTEM and electron diffraction. The probability for being attacked seems not to depend on the initial particle size. This process is likely limited by the number of available chelating molecules per nanoparticle, consistently with accelerated kinetics for lower nanoparticles/citrate concentrations.

References:

[1] RIVIERE C., WILHELM C., COUSIN F., *et al.*, Internal structure of magnetic endosomes, *Eur. Phys. J. E*, 2007, 22, p. 1 – 10

[2] MACKENZIE E.L., IWASAKI K., TSUJI Y., Intracellular iron transport and storage: from molecular mechanisms to health implications, *Antioxid. Redox Signal.I,* 2008, 10, p. 997 – 1030

[3] BRILEY-SAEKO K., BJORNERUD A., GRANT D., *et al.*, Hepatic cellular distribution and degradation of iron oxide nanoparticles following single intravenous injection in rats: implications for magnetic resonance imaging, *Cell Tissue Res.*, 2004, 316, p. 315–23

[4] OKON E., POULIQUEN D., OKON P., *et al*., Biodegradation of magnetite dextran nanoparticles in the rat. A histologic and biophysical study, *Lab. Invest.*, 1994, 71, p. 895 – 903

[5] SCHULZE E., FERRUCCI J.T. Jr., POSS K., *et al.*, Cellular uptake and trafficking of a prototypical magnetic iron oxide label *in vitro, Invest. Radiol.,* 1995, 30, p. 604 – 610

[6] WILHELM C., GAZEAU F., Universal cell labelling with anionic magnetic nanoparticles *Biomaterials*, 2008, 29, p. 3161 – 3174

[7] LEVY M., LAGARDE F., MARALOIU A., *et al.*, Degradability of superparamagnetic nanoparticles in a model of intracellular environment: follow-up of magnetic, structural and chemical properties, *Nanotechnology*, 2010, 21, p. 1 – 11

[8] ARBAB A.S., WILSON L.B., ASHARI P., *et al.*, A model of lysosomal metabolism of dextran coated superparamagnetic iron oxide (SPIO) nanoparticles: implication for cellular magnetic resonance imaging, *NMR Biomed.*, 2005, 18, p. 383 - 389

CHAPTER VI

Biodistribution and biotransformations of the P904 agent in the atherotic mouse: a study from ex vivo samples

We first recall here the results acquired by MRI and introduce those brought by photonic microscopy concerning the examination of the aorta's atheroma in mice injected with P904 contrast agent. These data provided us a basis to develop further studies of the atherotic plaque: by bi-photon microscopy using a fluorescent version of the P904 contrast agent, then by TEM (CTEM, HRTEM and STEM) and by magnetic measurements. Features evidenced in the aorta were analyzed by reference to those observed in the spleen of the same injected mice.

VI.1. The atherotic plaque of the mouse's aorta studied by MRI and visible light microscopy

VI.1.1. MRI examination

As reported in Chapter IV, a total number of 10 ApoE-/- mice (C57BL/6 background) were used in the study. Animals were started on a high-fat diet (Western Diet, 0.5% cholique acid and 1.25% cholesterol) at 6 weeks of age. At 28 weeks of age, 8 out of the 10 animals were administered a dose of 1000 μmol Fe/kg of the P904 contrast agent. The two remaining animals were considered as the control group.

All baseline MRI images (Figure VI.1) clearly showed the aortic arch on coronal as well as transverse views. Signal loss regions in the shape of "blooming artifacts" (indicated by arrows in Figure VI.1) were identified around the bright lumen, in the aortic sinus, indicating focal accumulation of iron in the vessel wall. They were clearly visible at Days 2, 20 and 28 after particle administration, less visible at the last imaging point (Fig IV.1).

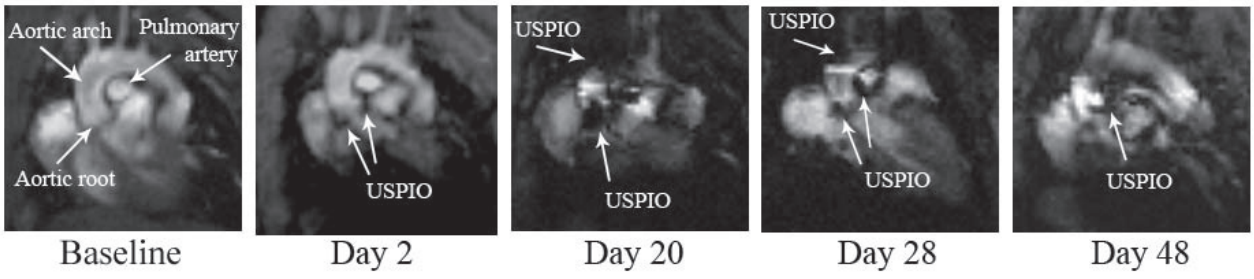

Figure VI.1. MR images (coronal views) from mouse's aorta before (baseline) and at different Days (D) after injection of the P904 contrast agent.

VI.1.2. Visible light microscopy

Semithin sections of samples taken ex vivo from atherotic aorta and prepared for TEM as described in Chapter II were studied by visible light microscopy.

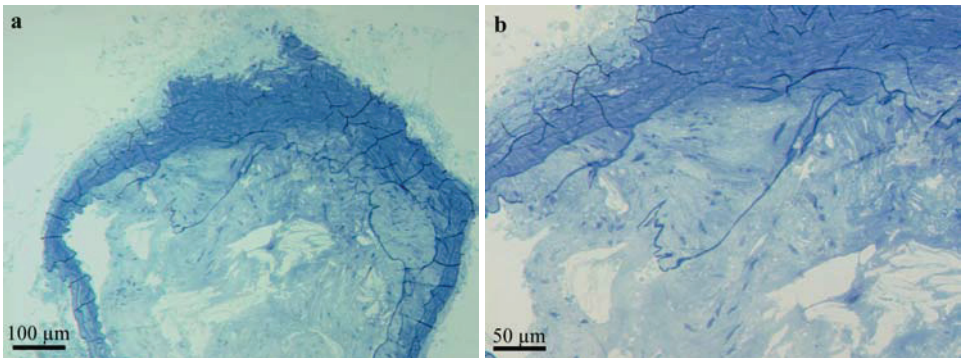

Figure VI.2. Visible light observation of the aorta.

Examples of aorta's views recorded at Day 2 after injection of P904 agent are reproduced in Figure VI.2. In Figure VI.2a, the aortic wall and the plaque can be clearly seen: here the plaque covers almost the aorta's lumen. At higher magnification, the nuclei of the smooth muscle cells in the plaque can be observed (Figure VI.2b).

VI.2. Distribution of the contrast agent studied in aorta and spleen by bi-photon microscopy

This study was achieved using a fluorescent version of the P904 agent, the fluorescence being excited by addition of two IR photons, as described in Chapter II.

VI.2.1. Experimental procedure

VI.2.1.1. Animal model and fluorescent agent for injection

The fluorescent contrast agent was provided by GUERBET Laboratories. It was derived from the standard P904 formula by grafting at the surface of the coverage a fluorescent dye belonging to the Rhodamine family; the emission wavelength is expected close to 600 nm [1, 2].

A total number of 8 ApoE-/- mice (C57BL/6 background) were used in the study. Animals were started on a high-fat diet (Western Diet, 0.5% cholique acid and 1.25% cholesterol) at 12 weeks of age. At 32 weeks of age, 3 of the animals were administered with the same dose of 1000 µmol Fe/kg (**high dose**) as for MRI studies and 3 of them with 600 µmol Fe/kg (**low dose**) by injection of the appropriate dose of P904 contrast agent. The two remaining animals were considered as the control group.

At the desired dates Days 0 (before injection) and 4, 8 and 15 (after injection), the aorta and the spleen of the mice were removed and fixed in a 1.5% glutaraldehyde, 1%

paraformaldehyde in buffer 0.15 M cacodylate solution. The ex vivo tissue samples were kept at 4°C until the observation by bi-photon microscopy was possible.

VI.2.1.2. Bi-photon experiments

A Ti: sapphire laser with an incident power of 3200 mW was used for excitation. The excitation wavelength λ was first varied between 650 and 900 nm to search for the maximum fluorescence intensity in the irradiated samples, which was obtained for λ=800 nm kept for the experiments. The fluorescence in the samples was detected by means of 3 PMT detectors in epi-collection, covering the ranges 374 – 486 nm (blue), 506 – 578 nm (green) and 576 – 660 nm (red). Thus the whole fluorescence emitted in the visible range 347 – 660 nm was detected, from what the color (C) images were obtained. The black and white (BW) images were deduced from the C images by converting the total intensity per pixel in grey level.

The images were acquired slice by slice in the sample depth (z-axis). Depth steps of 3 to 5 μm were used to form depth stacks of several tens of slices.

For a given stack, the z-projection images were obtained by averaging the pixel intensities over the depth of the stack. Orthogonal views along a given line in a given image were also recorded: they correspond to the distribution of the intensity in a slice perpendicular to the initial image plane. They are displayed parallel to the chosen line with respect to the initial image

VI.2.2. Experimental results

The results concerning the aorta in mice injected with high and low dose of fluorescent agent will be reported first and then the results concerning the spleen from mice injected with the high dose only due to limitation in time.

VI.2.2.1. Study of the aorta

a) Control mouse

Images of the atheromatous aorta from a non-injected mouse were recorded as a reference (Figure VI.3 a and b).

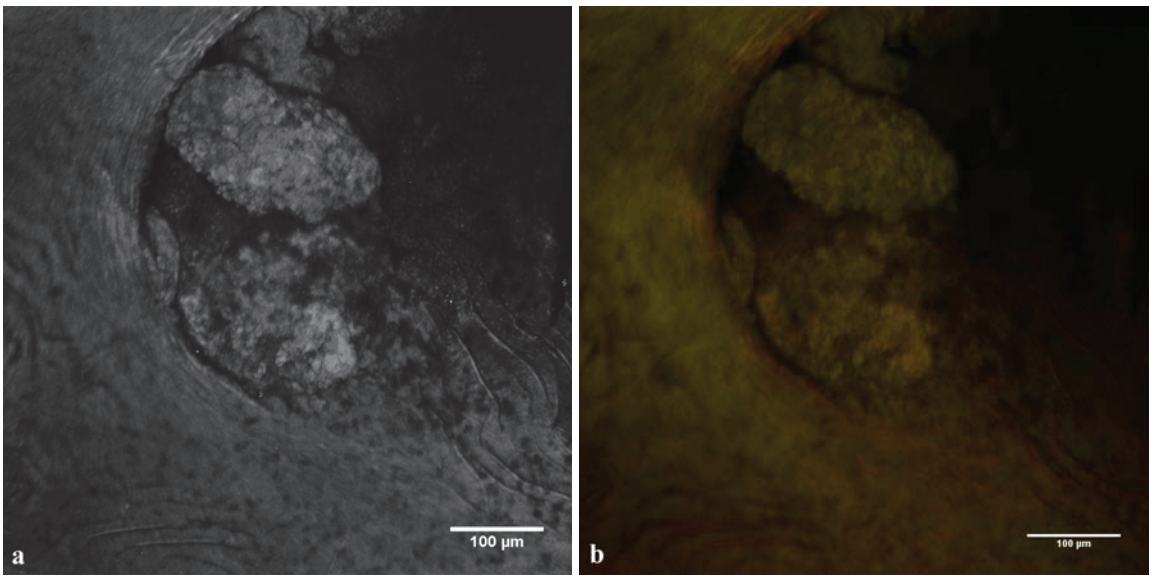

Figure VI.3. Images of an atheromatous aorta from a non-injected mouse.

On both the BW (a) and C (b) images, the aortic wall surrounding the atherotic plaque is well evidenced. On the C image, the elastin fibers, for instance, in the wall can be seen giving rise to an endofluorescence in the orange-red range [3, 4]. Nevertheless it must be emphasized here that the colors corresponding to different components are not those which would be observed from fresh tissues, due to the fixation process.

b) Mice injected with the high dose of contrast agent

On images from aorta's samples taken ex vivo 4 days after injection (Figure VI.4), the healthy arterial wall can be observed. Attached to it, a well developed atherotic plaque contains bright fluorescent spots with sizes between 2 and 10 µm, the fluorescence emission being in the yellow-orange range. All these features suggest that these are agglomerates of contrast agent nanoparticles. On the BW image (a), the contrast of the agglomerates is enhanced. The orthogonal views with respect to the C image (b) show that these agglomerates are embedded in the plaque.

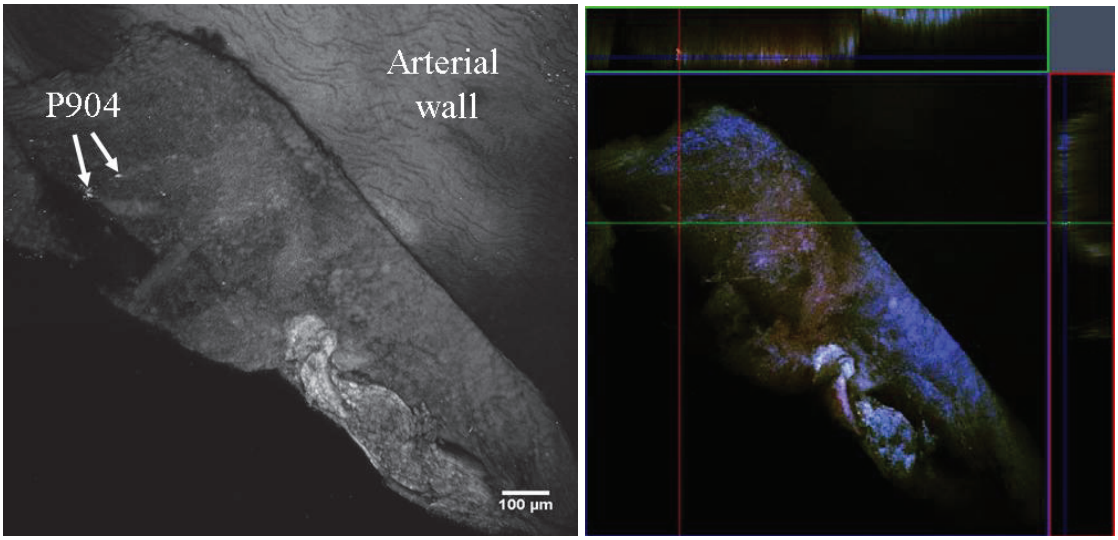

Figure VI.4. Images of an atheromatous aorta observed 4 days after injection of the contrast agent (high dose).

Images from an atheromatous aorta taken 15 days after injection (Figure VI.5) reveal an increase in the density and the size of the agglomerates. In the recorded image, their size varies in the range of 2 to 30 µm. Agglomerates are also seen in the arterial wall, the orthogonal view confirming the embedding in the tissue.

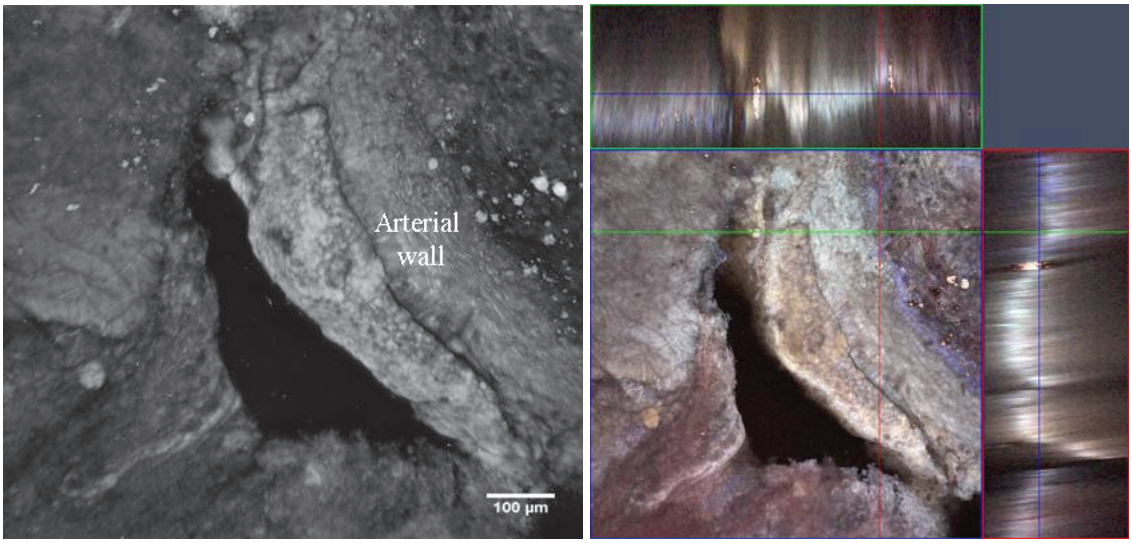

Figure VI.5. Image of an atheromatous aorta observed 15 days after injection of the agent (high dose).

c) Mice injected with the low dose of contrast agent

The images of Figure VI.6 were recorded from an atheromatous aorta 4 days after injection showing the plaque attached to the arterial wall. Besides a low density of small

agglomerates, some very big fluorescent spots are seen, which correspond to large agglomerates of agent nanoparticles. Orthogonal views confirm that they are embedded in the plaque.

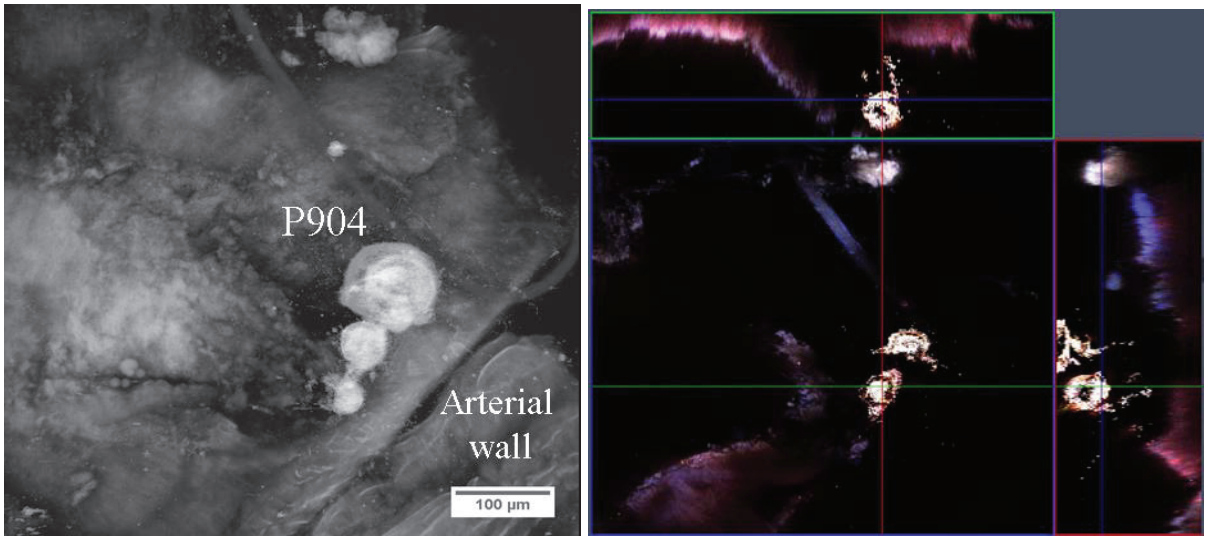

Figure VI.6. Images of an atheromatous aorta observed 4 days after injection of the contrast agent (low dose).

On images of Figure VI.7 recorded 8 days after injection, only the plaque is seen revealing an increase in the density and the size of the agglomerates.

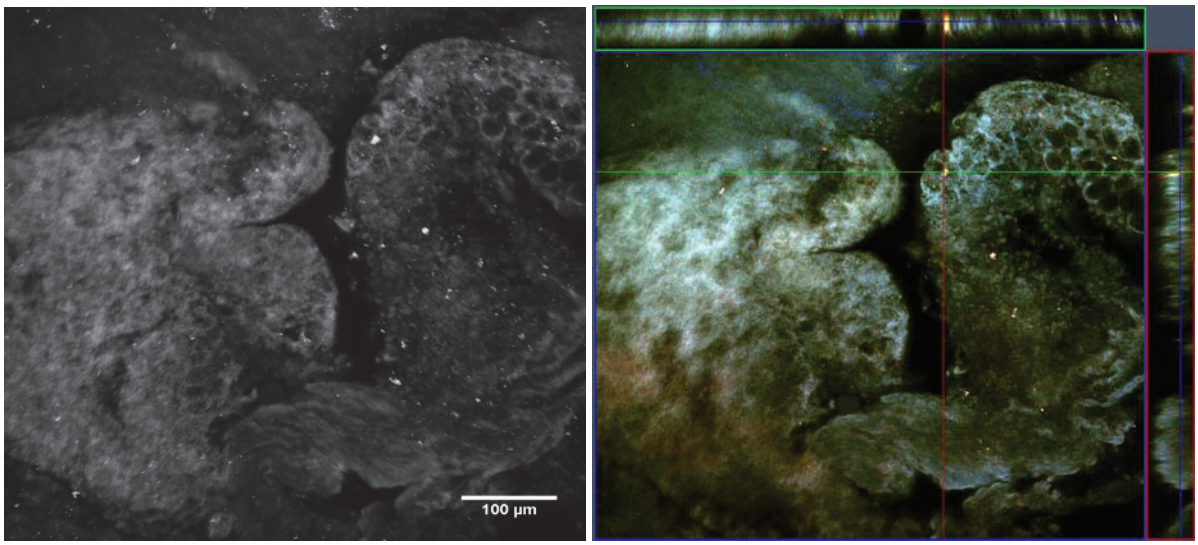

Figure VI.7. Image of an atheromatous aorta recorded 8 days after injection of the contrast agent (low dose).

Images from an atheromatous aorta recorded 15 days after injection show fluorescent spots in the plaque attached to the wall (Figure VI.8a). Figure VI.8b reveals the size

distribution of the agglomerates, which are embedded in the plaque (Figure VI.8c). At high magnification (Figure VI.8d), details of the fluorescent spots are shown whose size is expected to correspond to vesicles in macrophages.

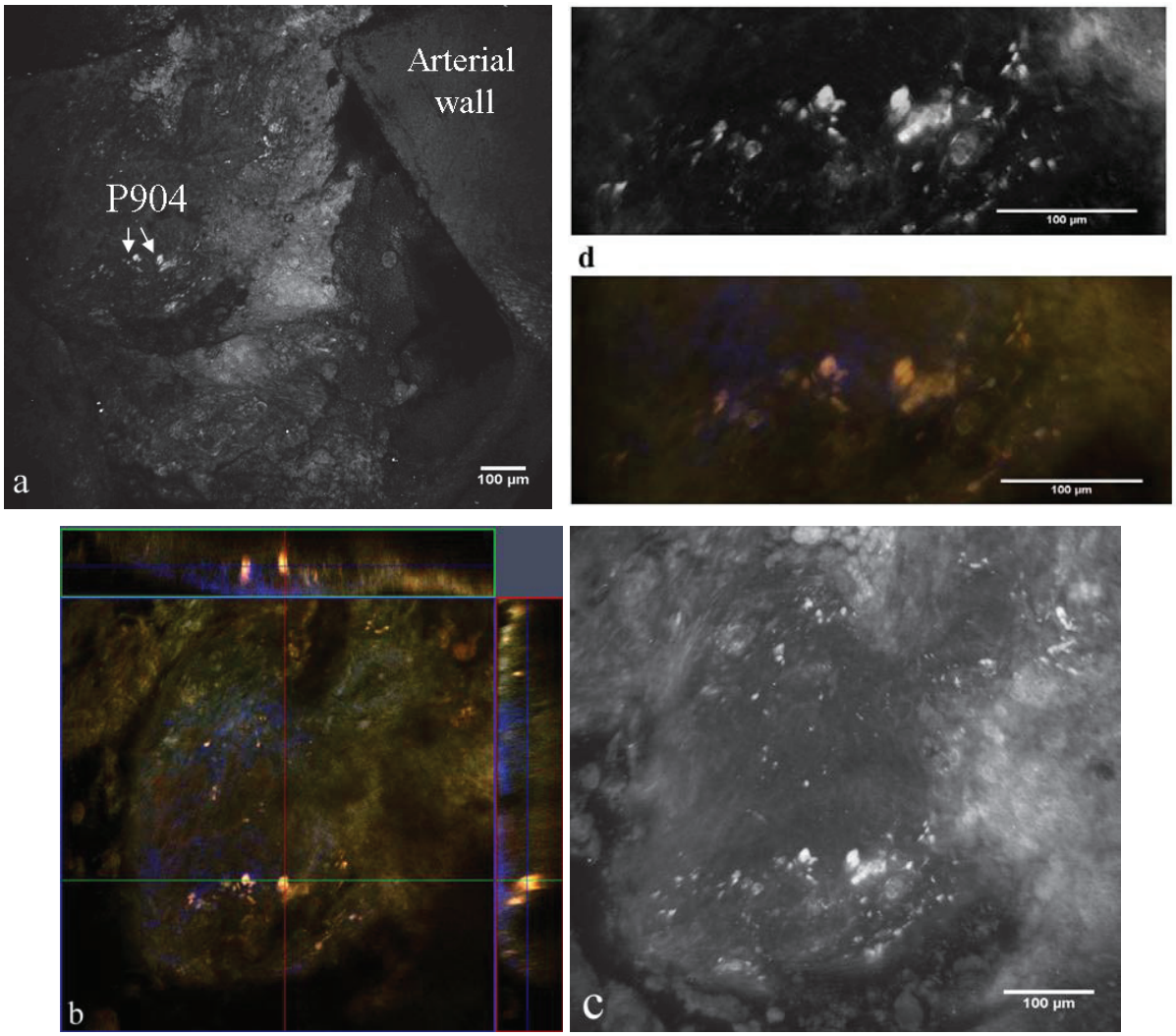

Figure VI.8. Images of an atheromatous aorta recorded 15 days after injection of the contrast agent (low dose).

The ability of bi-photon microscopy to reveal small to large agglomerates of fluorescent contrast agent nanoparticles has been demonstrated; the distribution and the variation in size of the agglomerates in the atherotic aorta can be studied up to high magnifications relevant to cell scale (macrophages). Bi-photon microscopy appears to be sensitive to smaller doses of contrast agent with respect to MRI. Indeed, the present experiments achieved after high dose injection proved to be less informative but this can be simply due to a poor quality of the ex vivo samples (small number of trials).

VI.2.2.2. Study of spleen in mice injected with the high dose of agent

Figure VI.9 first displays reference images from a non-injected mouse.

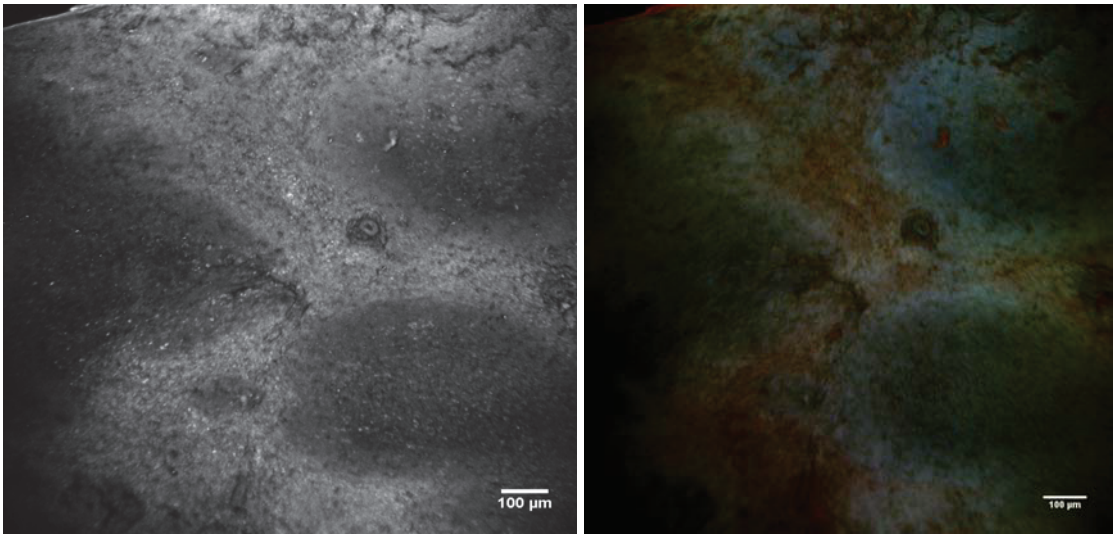

Figure VI.9. Images of the spleen from a control mouse.

With respect to Figure VI.9, images of Figures VI.10 and 11 evidence agglomerates with size between about one µm and a few ten µm. Many of them are located at the boarder of darker areas. Orthogonal views confirm that they are embedded in the organ.

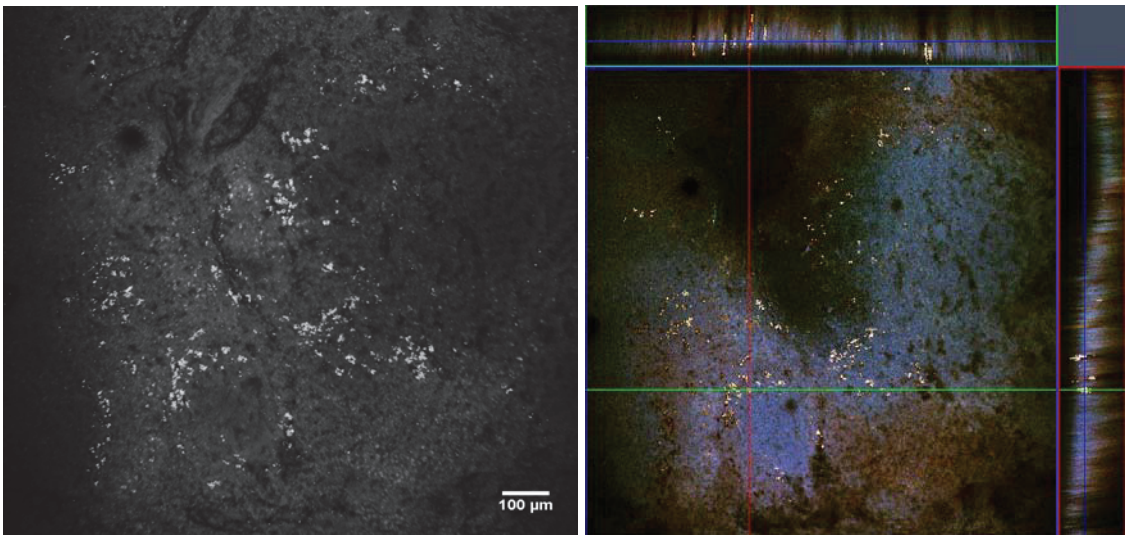

Figure VI.10. Images of the spleen recorded 4 days after injection of the agent (high dose).

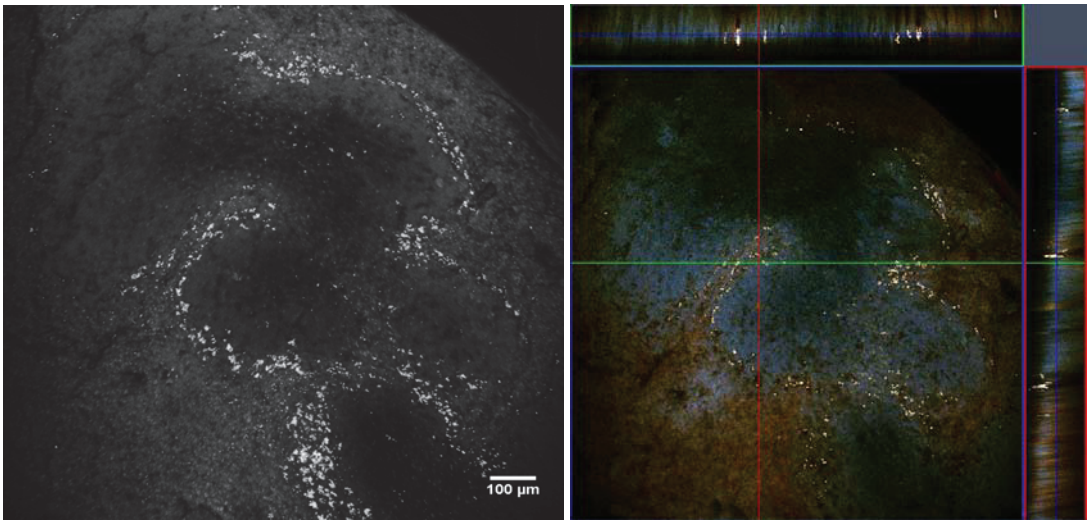

Figure VI.11. Image of the spleen recorded 15 days after injection of the agent (high dose).

VI.3. Structural studies by TEM

The aim of the study was to determine the biodistribution and the biotransformations of the contrast agent nanoparticles in the aorta and the spleen from mice injected with the (non fluorescent) P904 agent. The preparation of the corresponding ex vivo samples for TEM studies has been described in Chapter II, section II.2.3.7. For the ultrathin specimens on grids obtained by inclusion in resin and ultramicrotomy, a protocol of coloration known as a standard one for investigations in biology was first planned. This protocol is conceived to reveal the features of tissular and cellular environments, but its use of chemicals containing heavy atom compounds (lead citrate and uranyl acetate) proved to induce dark contrast artefacts on TEM images, some of them with submicrometric size possibly confusing for detection of contrast agent nanoparticles. So we treated our thin specimens with very weak coloration or no coloration at all. In turn, the tissular and cellular environment in our TEM images could not be easily analyzed most of the time.

VI.3.1. Characterization of the P904 agent before injection

The features of the P904 agent are recalled here as reference data.

The characterization was first achieved by Wet STEM technique (as reported in Chapter II) to reveal the behaviour of the nanoparticles in liquid suspension. An example of Wet STEM image from a diluted suspension (Figure VI.12a) confirms that there is no strong tendency to flocculation. The iron oxide core nanoparticles are seen as white spots in the

liquid; a large fraction of the population exhibits a size in the range 7 – 10 nm, what does correspond to the diameter of the agent core as reported by GUERBET.

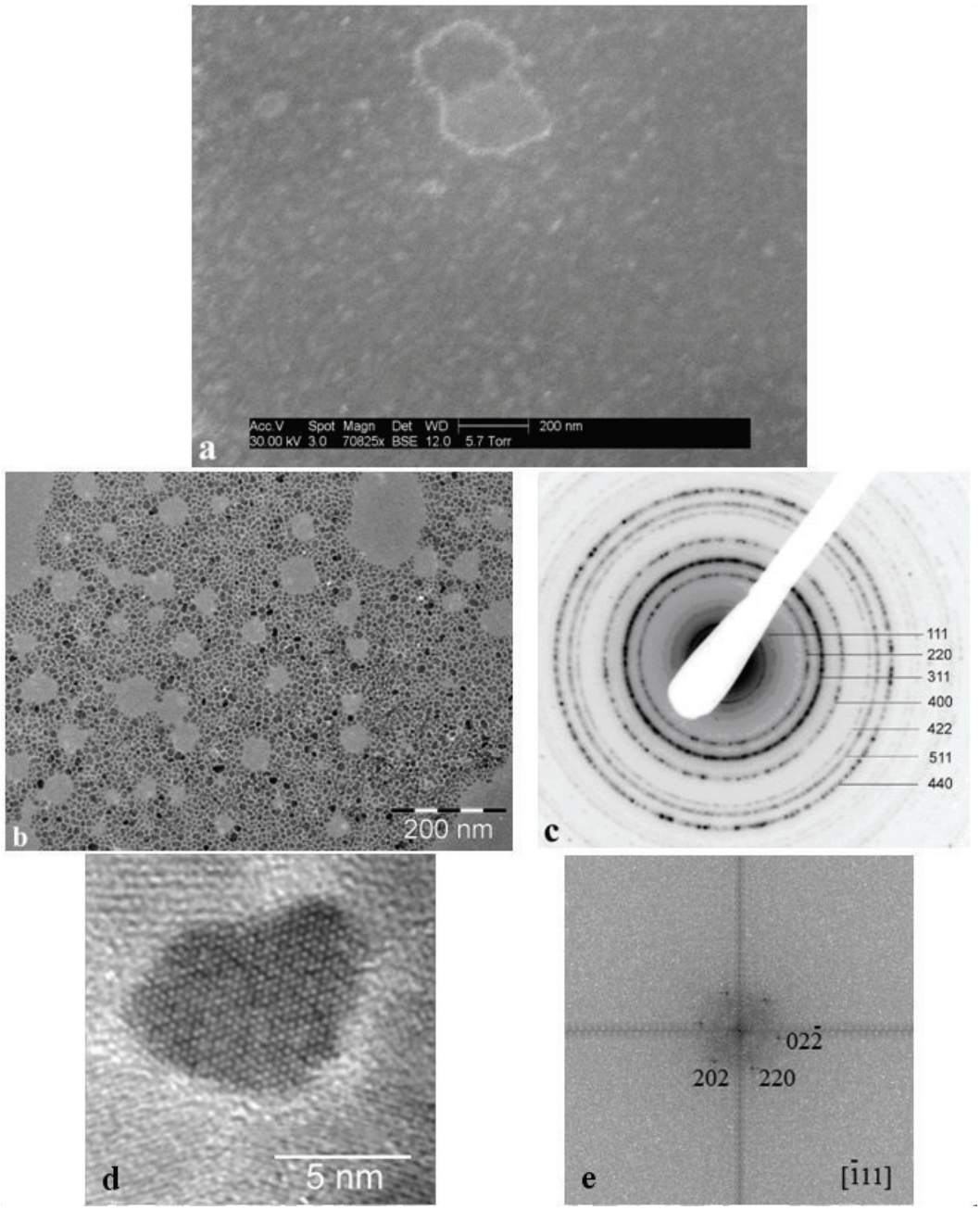

Figure VI.12. Initial features of the P904 agent studied by Wet STEM (a), CTEM (b), electron diffraction (c) and HRTEM (d) with FFT (e) of the HRTEM image confirming the maghemite structure and revealing the orientation of the nanoparticle imaged.

In Figure VI.12 b to e are reproduced the results from the TEM study of the agent nanoparticles after dry deposition. The diffraction pattern (c) from the CTEM overview (b) evidences the maghemite structure (see faint extra reflexions between 111 and 220). An example of high magnification HRTEM image from a nanoparticle (d) and its FFT (e) confirm the good crystallization of the nanoparticle core.

VI.3.2. Distribution and structure of the agent in the aorta

The results from study of the aorta removed at Day (D) 2 after the injection of the contrast agent are illustrated by Figure VI.13. On the CTEM image (Figure VI.13 up) only a few nanoparticles forming a small agglomerate (arrowed) are seen which could be identified as P904 agent nanoparticles. This typical example is significant of the very heterogeneous occurrence of agent nanoparticles in the aorta at this stage. The HRTEM image and its FFT (Figure VI.13 bottom) show that these nanoparticles have kept their crystalline maghemite structure and their size. The EDX spectrum (Figure VI.13 up right) recorded from the agglomerate confirms the presence of the iron element (see enlargements of the circled regions of interest). Of course the oxygen element (among other ones) is also detected, but the Fe:O ratio cannot be analyzed with respect to the composition of the nanoparticles since oxygen is also present in the organ and the preparation products (resin...).

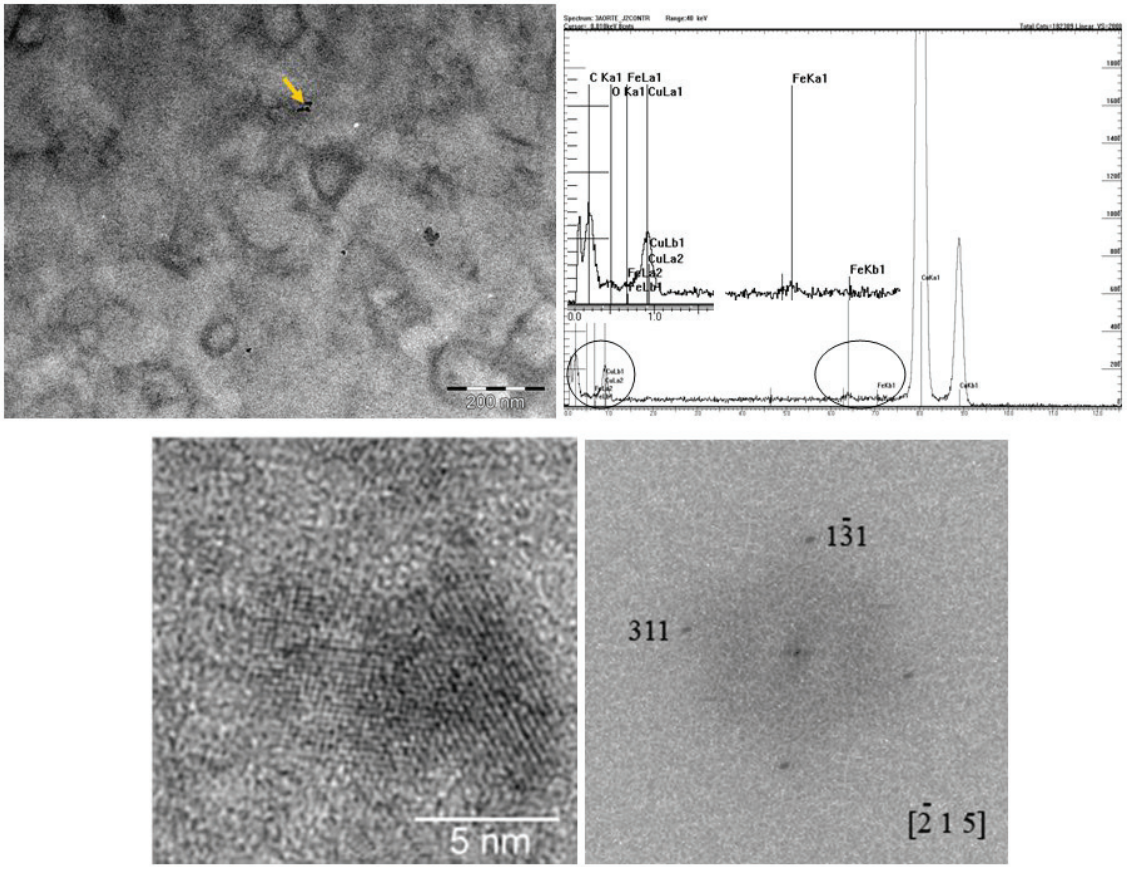

Figure VI.13. TEM study of contrast agent nanoparticles in the aorta at D2: CTEM image revealing a small agglomerate of a few nanoparticles (arrowed), with corresponding EDX spectrum (*upper part*); HRTEM image of two of these nanoparticles with FFT from the central particle confirming its maghemite structure and revealing its orientation (*lower par*t).

At Day 20 after the injection, the nanoparticles have started agglomerating in vesicles (Figure VI.14 up), some of them being endosomes and some of them phagolysosomes. In the strongly contrasted (black and white) part of such vesicles the particles remain crystallized in the maghemite structure according to the corresponding electron diffraction pattern and to details of the HRTEM view together with FFTs of the HRTEM images of the nanoparticles in the vesicle (Figure VI.14 bottom).

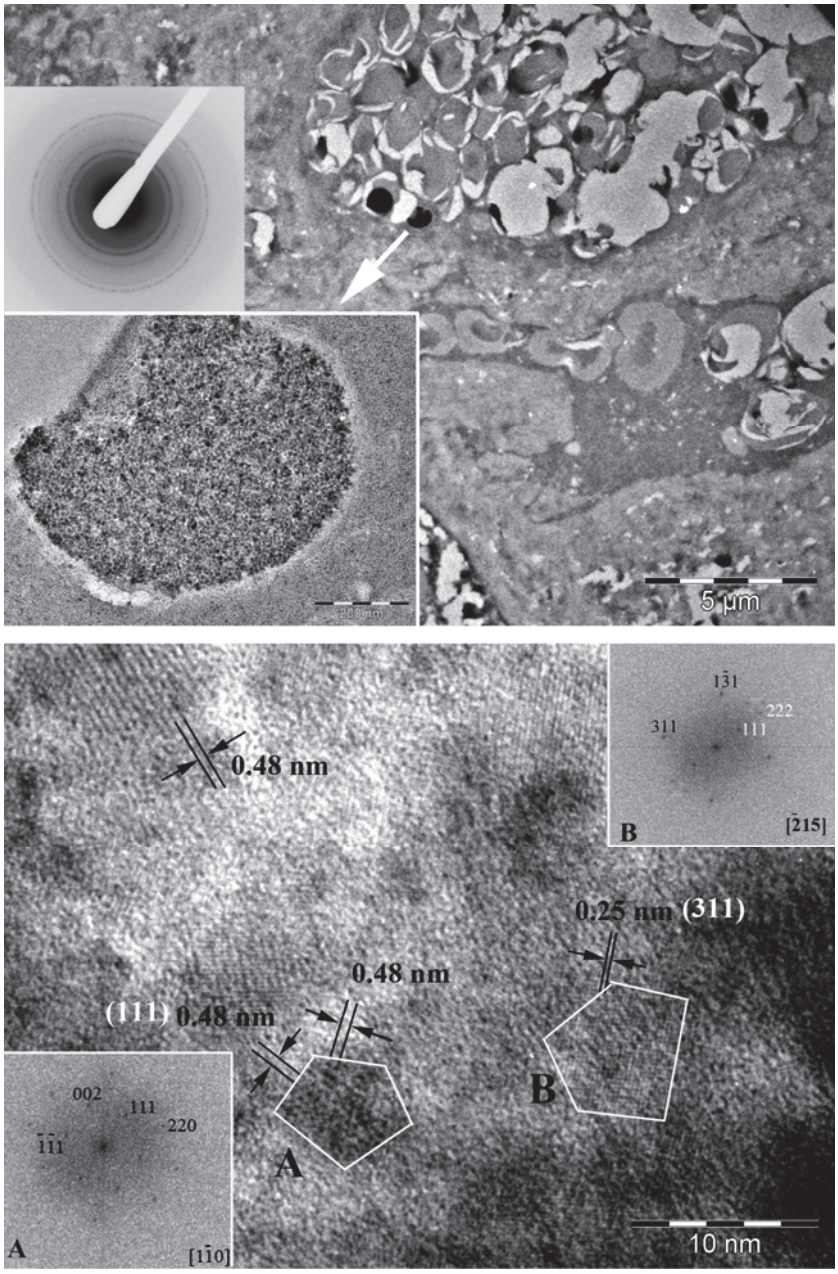

Figure VI.14. TEM study of contrast agent nanoparticles in the aorta at D20: in the *upper part* a central vesicle having internalised nanoparticles (arrowed) is seen enlarged in the inset, with corresponding electron diffaction pattern above; in the *lower part* a high magnification HRTEM image from the vesicle reveals details of crystallized nanoparticles , with FFT confirming the maghemite structure and revealing the orientation of the particles A and B (in FFT from B, 111 and 222 reflexions arising from another particle nearby are detected also).

At Day 49 after injection the occurrence of dense vesicles is confirmed. In Figure VI.15 up an example of agglomeration of nanoparticles in a phagolysosome is observed surrounded by collagen fibers. The corresponding electron diffraction pattern confirms that many nanoparticles therein have remained crystallized in the maghemite structure. The crystallinity of such nanoparticles is further evidenced by details of the high magnification HRTEM images together with the corresponding FFT (Figure VI.15 down).

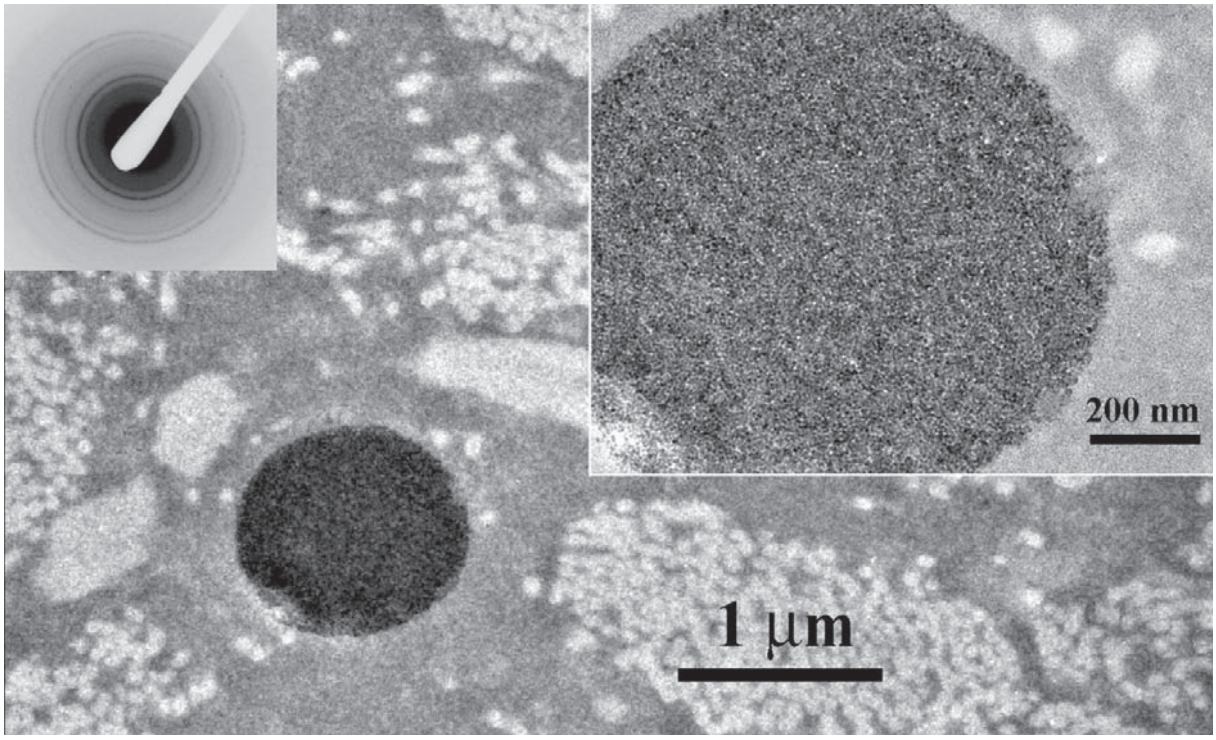

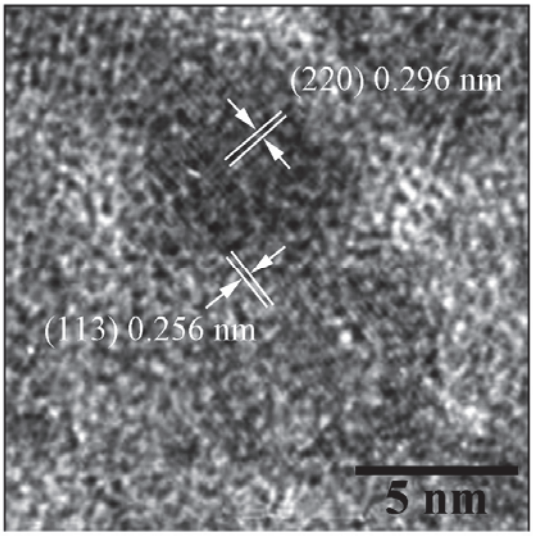

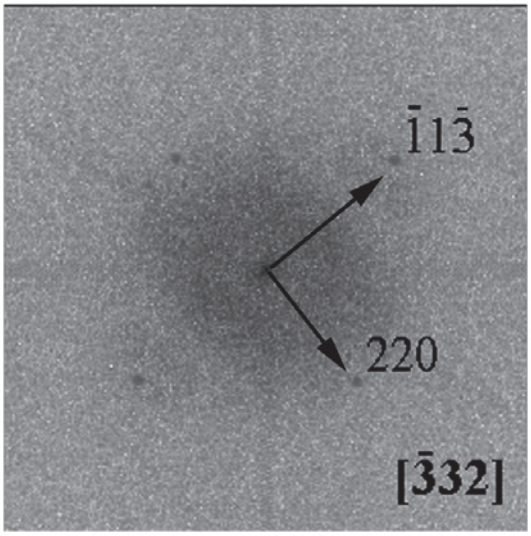

Figure VI.15. TEM study of the aorta at D49: CTEM image of a phagolysosome seen enlarged in the right inset, with corresponding electron diffraction pattern in the left inset (*upper part*); high magnification HRTEM image from the phagolysosome evidencing the crystallized state of some nanoparticles , with FFT confirming the maghemite structure and revealing the orientation of the central particle (*lower part*).

Using ImageJ software, the size distribution of the P904 nanoparticles evidenced in the atherotic aorta has been statistically measured from medium magnification TEM images and fitted with LogNormal statistical distribution using Origin software. The corresponding results are displayed in Figure VI.16 for particles before injection (initial) and at different dates post injection; the corresponding values of the median diameters D_m were: 6.7 nm (initial), 5.8 nm (D2), 6.43 nm (D20) and 7.26 nm (D49).

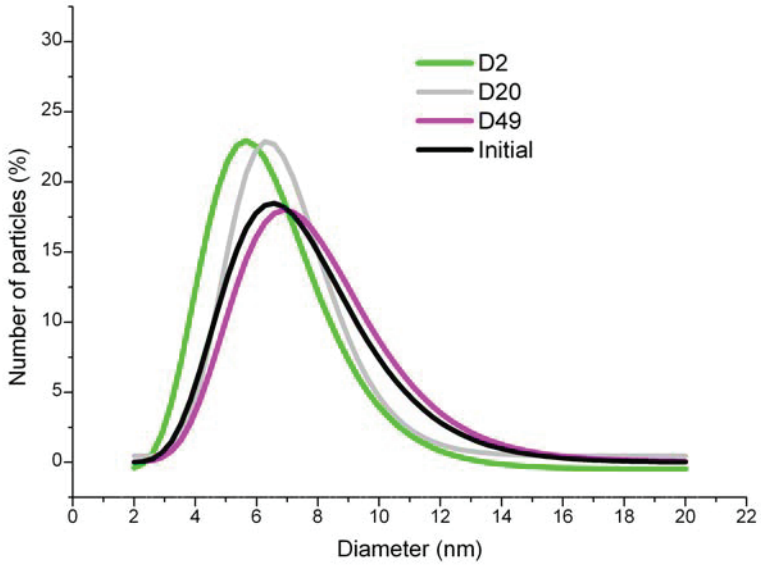

Figure VI.16. Size distribution of P904 nanoparticles in the atherotic aorta.

VI.3.3. Distribution and structure of the agent in the spleen

Since vesicular agglomerations are known to occur currently in the spleen, a correlated TEM study of this storage organ was undertaken for the same mice.

Images recorded from the spleen at Day 2 after injection (Figure VI.17) show large vesicular agglomerations (here with a diameter between 0.9 and 1.9 μm) of P904 nanoparticles. These vesicles exhibit strongly contrasted domains and rather blank ones. The nanoparticles in the contrasted domains are well crystallized (HRTEM image) in the maghemite structure (electron diffraction pattern). The presence of iron is confirmed by EDX spectra (with enlargements of the circled regions of interest) recorded from these vesicles.

An example of study at Day 20 after injection is reproduced in Figure VI.18. A cell with its nucleus (marked N) and several vesicles can be clearly distinguished in the CTEM image. One of these vesicles (seen enlarged) is of particular interest, with three different areas. As shown by the corresponding electron diffraction patterns, well crystallized P904 nanoparticles are agglomerated in the left area (marked 1). From the right area (marked 3) a

readily different diffraction pattern is recorded: it corresponds to ferritin structure [5]. The central area (marked 2) corresponds to a structure intermediate between maghemite and ferritin. This vesicle is a phagolysosome [6].

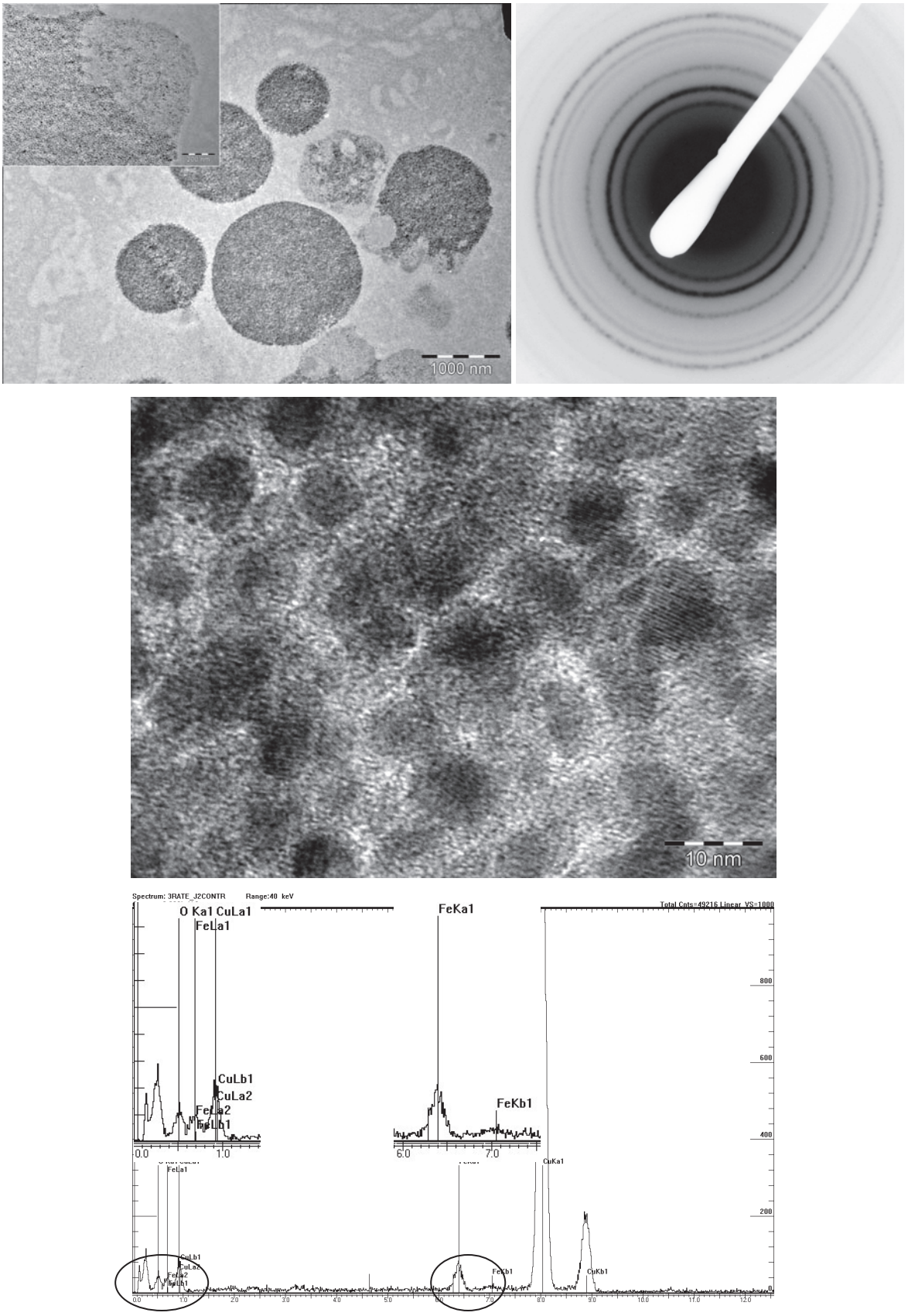

Figure VI.17. TEM study of the spleen at D2.

Agglomerations of P904 nanoparticles are also found at longer periods of time after injection. In the example of Figure VI.19 recorded at Day 40, a round shape vesicle with dark contrast is observed. The corresponding diffraction pattern is characteristic of nanoparticles crystallized in the maghemite structure. The presence of iron is confirmed by the corresponding EDX spectrum (with enlargements of the circled regions of interest).

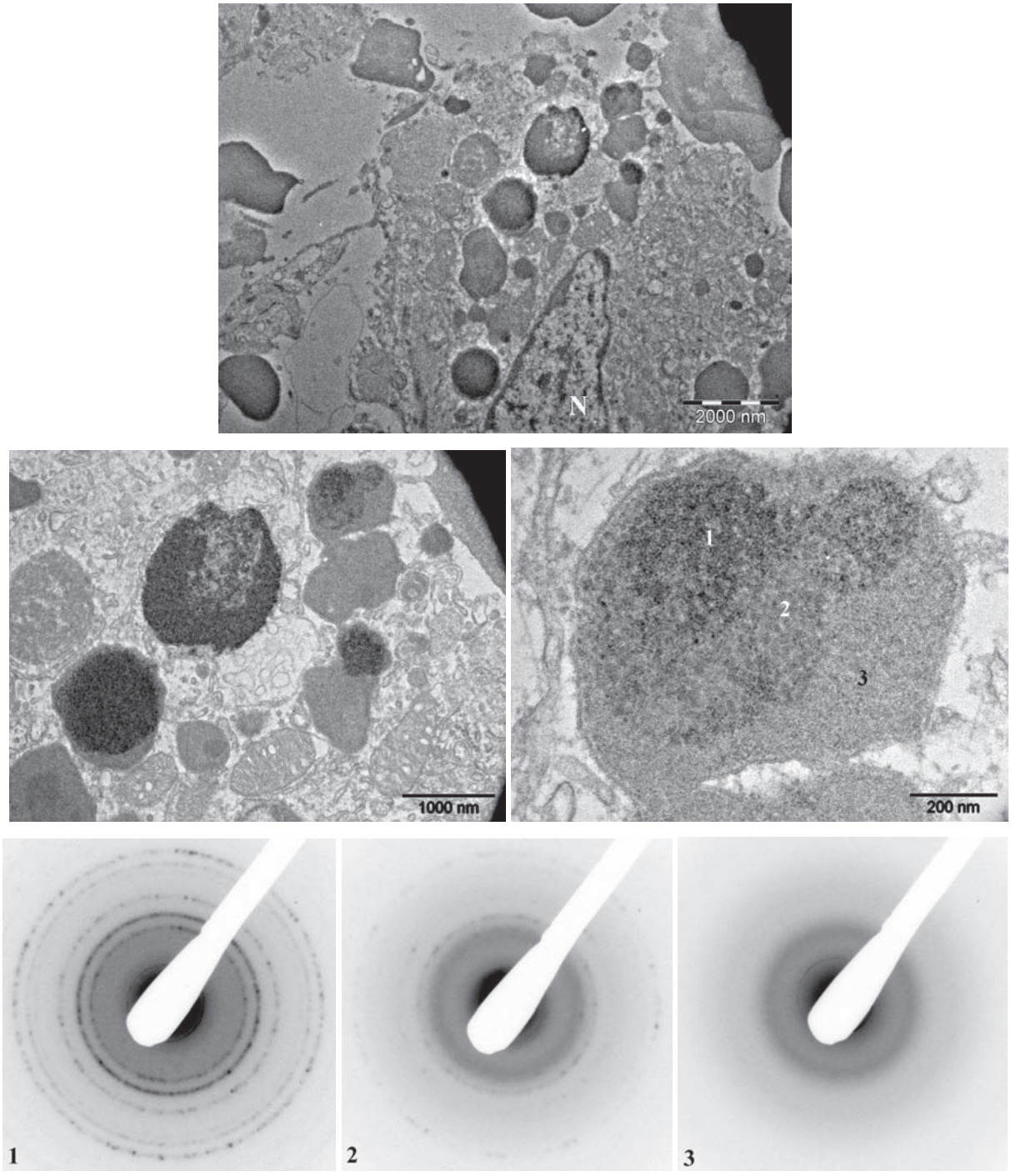

Figure VI.18. TEM study of the spleen at D20.

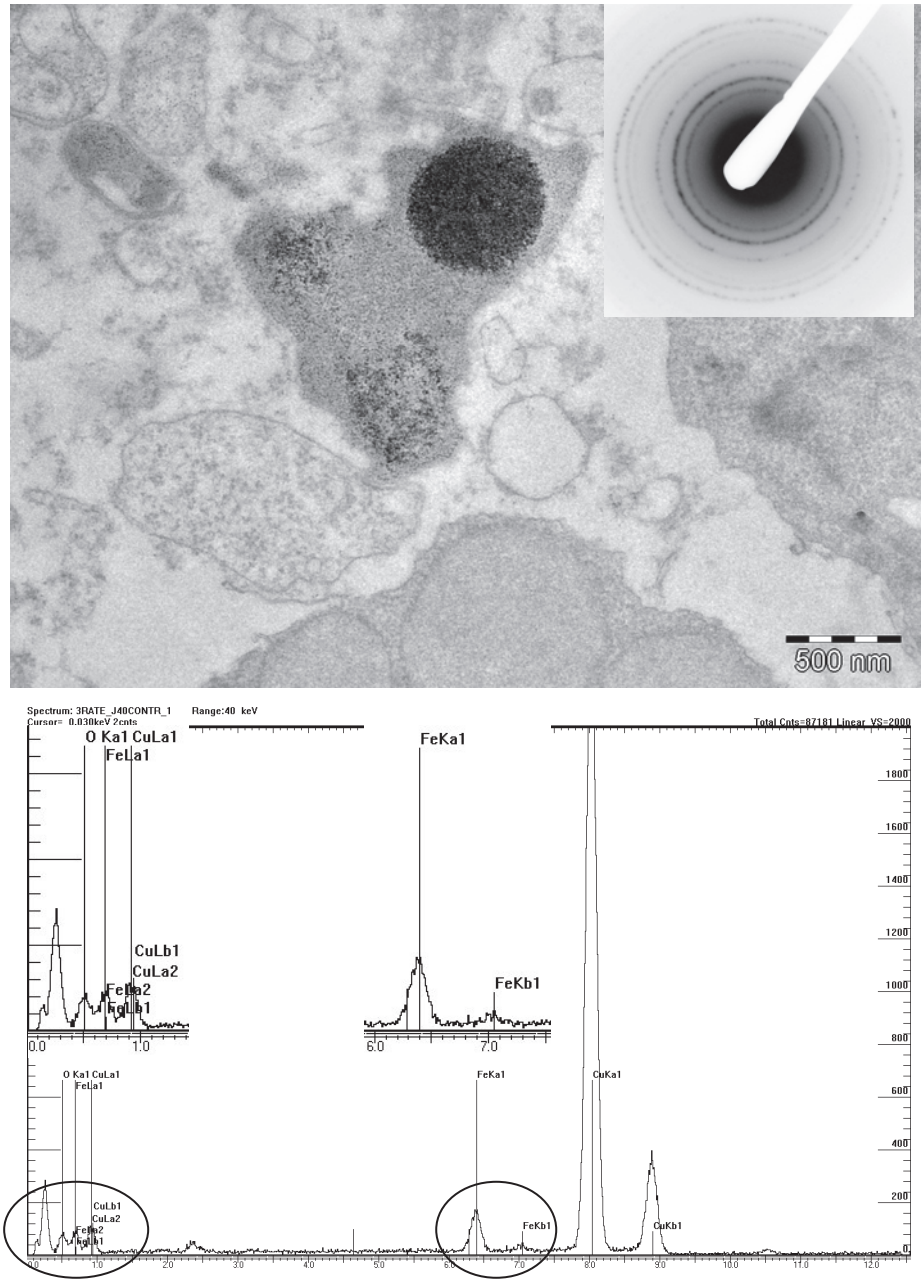

Figure VI.19. TEM study of the spleen at D40.

From the CTEM images at medium magnification, a statistical size distribution of the P904 nanoparticles evidenced in the spleen was achieved using the ImageJ software. These experimental distributions were fitted with LogNormal statistical distribution using Origin software. The corresponding curves are displayed in Figure VI.20 for particles before injection (initial) and at different dates post injection; the median diameters D_m corresponding to those distributions were: 6.7 nm (initial and D2), 6.1 nm (D20) and 7.4 nm (D30).

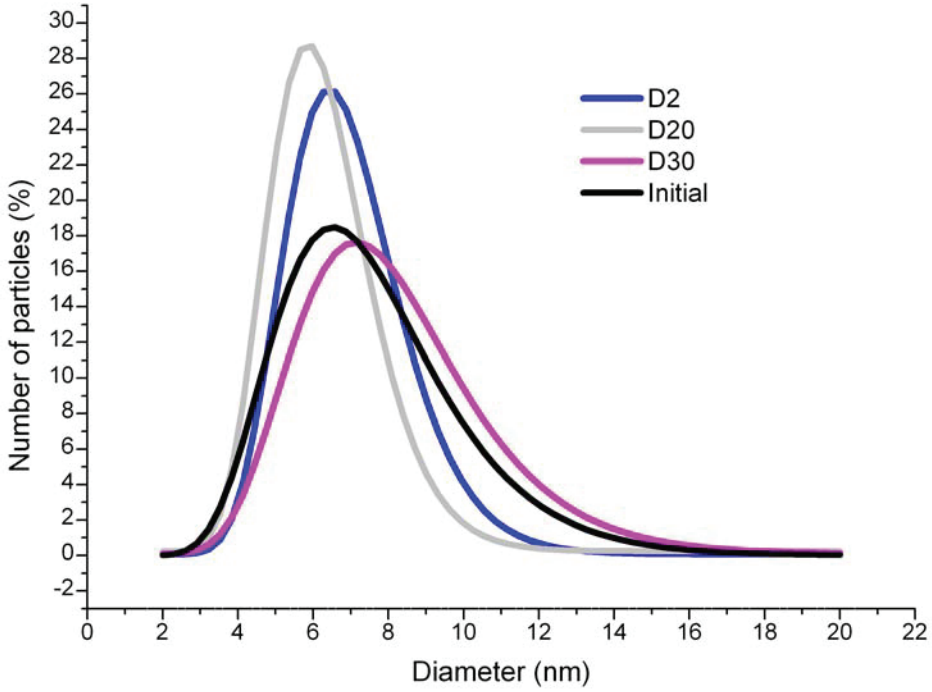

Figure VI.20. Size distribution of P904 nanoparticles in the spleen of atheromatous mice.

VI.4. STEM study of the spleen

A STEM-HAADF study was achieved on ex vivo spleen samples removed at D2 from a mouse injected with the P904 agent. An example of these results is reproduced in Figure VI.21 where the left part shows an overview of a phagolysosome exhibiting very bright spots corresponding to iron oxide core (Z contrast) nanoparticles therein and darker areas. The right part of the Figure VI.21 reproduces a high magnification enlargement recorded at the boarder between a dark and a bright area: at the bottom is imaged a bright crystallized nanoparticle with a diameter about 6 nm, where (220) reticular planes of maghemite, corresponding to the interplanar distance 0.296 nm, are identified; above the particle white zig zag contrasts are observed, possibly corresponding to the ferrihydrite (ferritin) structure [7, 8].

An example of a EELS spectra recorded over these imaged regions is reproduced in Figure VI.22. On such spectra the peaks characteristic of the Fe $L_{2/3}$ edge can be recognized, due to a majority of iron atoms in the Fe^{3+} configuration.

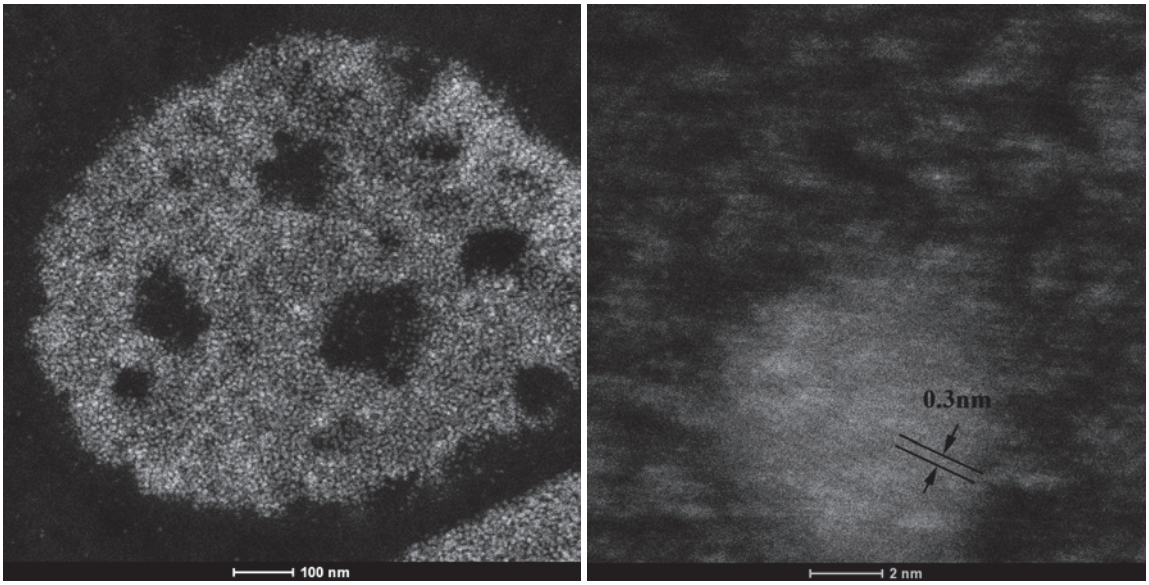

Figure VI.21. STEM study of the spleen at D2: overview of a phagolysosome featuring bright and dark areas (*left*) - high magnification image at the boarder of a dark area revealing a bright crystallized nanoparticle where (220) reticular planes of maghemite, with interplanar distance 0.296 nm, are identified; the particle is surrounded by zig zag contrasts possibly corresponding to the ferrihydrite (ferritin) structure (*right*).

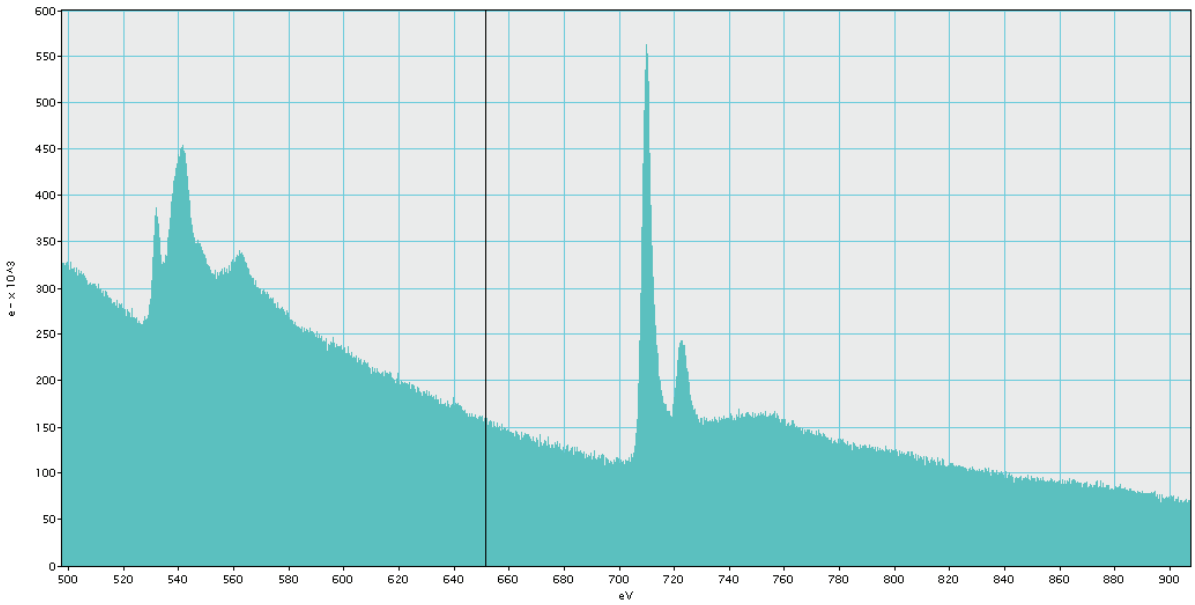

Figure VI.22. An example of EELS spectrum recorded over the regions imaged in Figure VI.21.

VI.5. Magnetic measurements

As reported in the previous section, the results from the TEM studies suggest that the size, the agglomeration state and finally the core structure (transformation in ferritin) of the P904 agent nanoparticles internalized in the aorta or the spleen of the mice can vary depending on time after injection. All these parameters can control the magnetic properties of such nanoparticles of which iron oxide core is expected to exhibit superparamagnetic behavior for sizes smaller than 50 nm. Therefore we planned to compare our TEM data with characterization of magnetic properties by SQUID measurements (see Chapter II).

This study has been undertaken in the frame of a collaboration with Centre de Magnétométrie at UCBL (V. Dupuis, A. Tamion – LPMCN, M. Hillenkamp – LASIM). We have developed sample preparation dedicated to such magnetic measurements which have been conducted by A. Hillion and M. Hillenkamp.

VI.5.1. Sample preparation

The P904 contrast agent before injection was studied in the initial suspension ready for injection, but also at different dilutions of that initial suspension. The suspensions were freeze-dried resulting in a sponge-like material.

Magnetic measurements were also performed on ex vivo samples from aorta or spleen. These ex vivo samples were taken from a control mouse and then at D(ays) 0 (3 hours), 2, 7, 13, 34 and 47 after injection. The desired tissues were extracted and they were desiccated in an oven at 64°C until they had lost at least 80% of their initial mass. Afterwards, they were milled in a mortar, to produce a powder.

The sponge-like material or the tissue powders were put to fill up the holder for magnetic measurements.

VI.5.2. Experimental measurements

The magnetic behavior of the samples was deduced from three experimental curves (like in Figure VI.23). The first one (Figure VI.23 inset) displays the magnetization depending on the external applied magnetic field at room temperature (300 K). The second one and third one display the variation of the magnetization depending on temperature for samples having been cooled down to 4K in absence (ZFC) or in presence of an weak applied magnetic field (FC), typically 10 Oe.

The team at Centre de Magnétométrie developed a method of fitting, named simultaneous triple fit [9]. The fitting of simulated curves with the experimental ones is optimized by adjusting different parameters: number of particles N_t, the constant of magnetic anisotropy K, the distribution of the magnetic diameter of the nanoparticles (simulated as spheres) from where the values $D_{m,n}$ - median magnetic diameter, and W – dispersion on diameter distribution, are deduced.

VI.5.3. Results

VI.5.3.1. Characterization of the P904 agent before injection

The P904 agent in the initial suspension had a tendency to agglomerate which made the magnetic measurements impossible because of saturation. In order to characterize the magnetic behavior of the agent, several dilutions were done, but only dilution per 1000 (1000x) was measured as a reference.

The corresponding ZFC and FC curves show that the agent nanoparticles before administration have a superparamagnetic behavior, what is confirmed by the magnetization curve at room temperature (Figure VI.23).

In the case of P904 agent diluted 1000 times, the superposition of the simulated curves with the experimental ones occurred for the optimized values of the parameters: $D_{m,n}$= 7.5 ± 0.5 nm, W = 0.25 ± 0.02, $N_t = 1.2 \times 10^{13}$, K = 15 ± 8 kJ·m^{-3}.

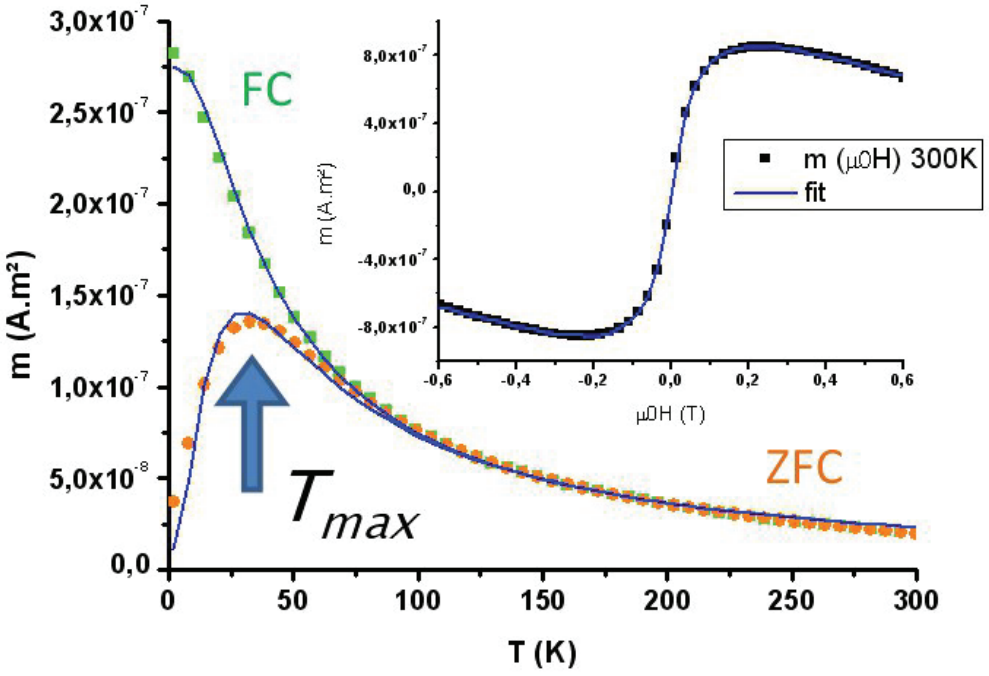

Figure VI.23. Magnetization measurements for initial P904 nanoparticles.

The corresponding distribution of the nanoparticle magnetic diameters is plotted in Figure VI.24 compared to CTEM measurements. The fact that the magnetic diameter of the nanoparticles, determined by SQUID, coincides well with the physical diameter, determined by TEM (Figure VI.24), tells us that the entire nanoparticles contribute to the magnetic behavior and that there are no inert layers.

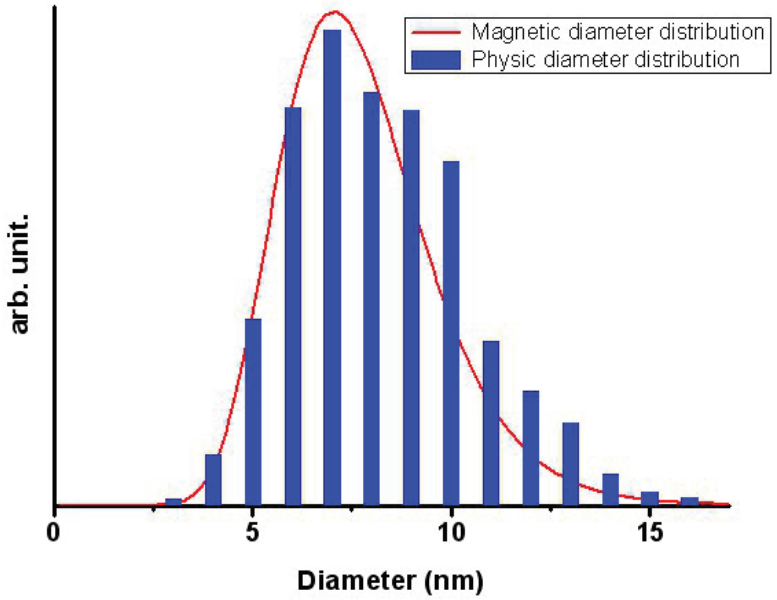

Figure VI.24. Size distribution of the nanoparticles, determined by CTEM and SQUID magnetic measurements.

VI.5.3.2. Results from aorta's samples

The distribution of the magnetic diameters for the P904 nanoparticles in the aorta at D0 and D2, compared to the 1000x dilution before injection are plotted in Figure VI.25. These curves do correspond to populations of individual particles. A decrease of the magnetic diameter for the cases of aorta at D0 and D2 is observed with respect to the state before injection. The corresponding values of the median magnetic diameters and the dispersions, very close for D0 and D2, are: D_m=5.4 nm and w=0.34 (D0), D_m=5.45 nm and w=0.35 (D2).

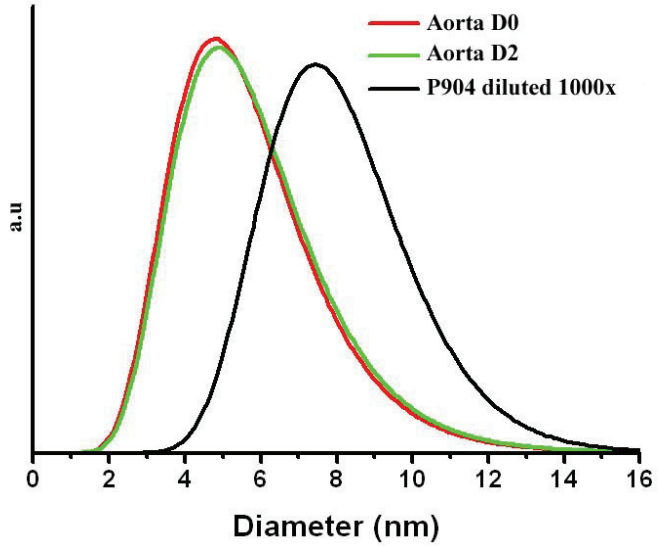

Figure VI.25. Magnetic diameter distribution for nanoparticles in the aorta.

VI.5.3.3. Results from spleen's samples

The corresponding magnetic diameter distributions are plotted in Figure VI.26.

The fitting of the magnetization curves required the introduction of 16% of dimmers (two magnetic particles interacting together) over the total nanoparticle population, what indicates a tendency to agglomeration.

Taking into account the experimental uncertainty (Section VI.5.3.1) the magnetic diameter can be regarded as nearly constant before it starts decreasing slightly. The corresponding values for the median magnetic diameters and dispersions are: D_m=7.8 nm and w=0.20 (D0), D_m=7.2 nm and w=0.24 (D2), D_m=7.1 nm and w=0.22 (D7).

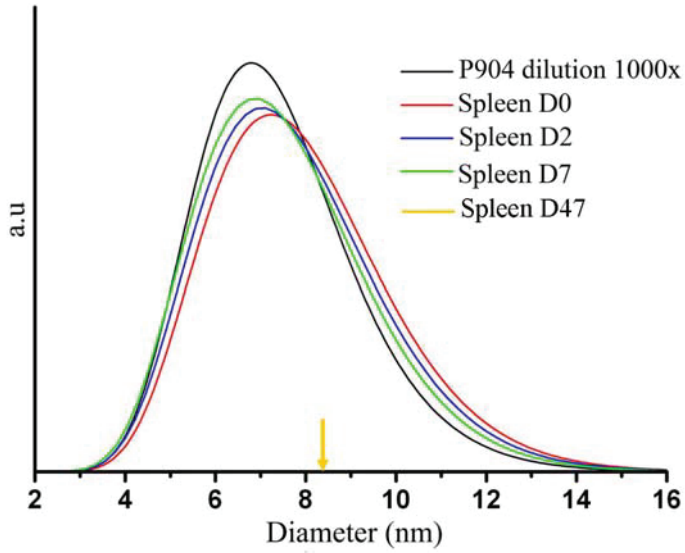

Figure VI.26. Magnetic diameter distribution for nanoparticles in the spleen.

VI.5.3.4. Discussion

In Table VI.1 hereafter are summarized the values of the nanoparticle median diameters in the aorta or the spleen determined by TEM or magnetic measurements before injection (*Initial*) and then at different Days (D) after injection of the nanoparticles.

	Aorta						***Spleen***				
	Initial	D0	D2	D20	D49		Initial	D0	D2	D20	D49
TEM (nm)	6.7	6.7	5.8	6.4	7.3		6.7	6.7	6.7	6.1	7.4
Magnetic (nm)	7.2-7.5	5.4	5.5	-	-		7.2-7.5	7.8	7.2	-	-

Table VI.1. Temporal follow-up for values of the median nanoparticle diameters from distributions determined by TEM and magnetic measurements respectively.

In the *Initial* condition for magnetic measurements two distinct values 7.2-7.5 nm have been determined separately by F.GAZEAU's team (Université Paris Diderot) and Centre de Magnétométrie (UCBL). This discrepancy is consistent with the experimental uncertainty of ± 0.5 nm raised by the team at Centre de Magnétométrie (see Section VI.5.3.1.) and such a value also holds for the TEM measurements. Despite this uncertainty and some restriction in experiments due to the limited duration of the present PHD work, coherent trends merge from Table VI.1. All together, the results can be understood on the basis of competition between two mechanisms which take place in the phagolysosomes where the nanoparticles get internalized are displayed in Section VI. The first one is the decrease in the iron oxide core size, towards the value corresponding to the ferritin core size (between 5 and 6 nm) so that the core will fit in the apoferritin cage. This decrease results from chemical reactions in the acidic medium corresponding to the lysosomal metabolism. The second mechanism corresponds to the agglomeration between nanoparticles which has been seen to occur in the endosomes and the phagolysosomes, what increases the magnetic interactions between the nanoparticles becoming closer.

Table's results are consistent with the fact that the agglomeration process is strong since the early times in the spleen what counteracts the tendency in decrease of the core size which then is statistically measured as nearly constant; whereas early stages in the aorta are governed by the decrease in size of less interacting nanoparticles. Indeed these conclusions are fully consistent with the TEM studies reported in Section VI.3.

References

[1] LAERMER F., ISRAEL W., ELSAESSER T., Femtosecond spectroscopy of stimulated emission from highly excited dye molecules, 1990, *J.Opt.Soc.Am. B*, 7 (8), p. 1604 – 1609

[2] MOSIMAN V., PATTERSON B.K., CANTERERO L., GOOLSBY C.L., Reducing cellular autofluorescence in flow cytometry: an in situ method, 1997, *Cytometry*, 30, p. 151 – 156

[3] ZIPFEL W.R., WILLIAMS R.M., CHRISTIE R., *et al.*, Live tissue intrinsic emission microscopy using multiphoton-excited native fluorescence and second harmonic generation, 2003, PNAS, 100 (12), p. 7075 – 7080

[4] LILLEDAHL M.B., HAUGEN O.A., DE LANGE DAVIES C., SVAASAND L.O., Characterization of vulnerable plaques by multiphoton microscopy

[5] GUTIERREZ L., LAZARO F.J., ABADIA A.R., *et al.*, Bioinorganic transformations of liver iron deposits observed by tissue magnetic characterisation in a rat model, 2006, *Journal of Inorganic Biochemistry*, 100, p. 1790 – 1799

[6] ONO T., TSUJII T., SENO S., A morphological study of ferritin synthesis in macrophages with ingested ferric hydroxide-potassium polyvinyl sulfate complexes, 1983, *Cell structure and function*, 8, p. 267 – 279

[7] QUINTANA C., COWLEY J.M., MARHIC C., Electron nanodiffraction and high resolution electron microscopies studies of the structure and composition of physiological and pathological ferritin, 2004, *Journal of Structural Biology*, 147, p. 166 – 178

[8] PAN Y-H., SADER H., POWELL J., *et al.*, 3D morphology of the human hepatic ferritin mineral core: New evidence for a subunit structure by single particle análisis of HAADF-STEM images, 2009, *Journal of Structural Biology*, 166, p. 22 - 31

[9] TAMION A., HILLENKAMP M., TOURNUS F., *et al.*, Accurate determination of the magnetic anisotropy in cluster-assembled nanostructures, 2009, *Appl. Phys. Lett,* 95, 062503

GENERAL DISCUSSION

The present work has achieved innovative developments in two domains of interest for magnetic nanovectors including nanoparticular contrast agents.

The first one is the application of Wet STEM mode of ESEM, with image simulation, to characterise the collective behaviour as well as the individual internal structure down to nanometric scale, for nanovectors in liquid suspension. This is a first step towards transmission electron microscopy at high spatial resolution for liquid suspensions. Comparison with our own TEM studies of nanoparticles after dry deposition has evidenced the need for such a characterization of nanovectors in the liquid suspension which is injected through intravenous route, in the patient's body. From this point of view, both the individual composite structure of the nanovectors as well as their collective behaviour, especially any tendency to flocculation, have to be assessed. Our experimental procedure can be further developed to optimize a more quantitative determination of these data with follow up in time for instance. The imaging studies can be also combined with in situ chemical analysis performed using the EDX setup which remains available in the ESEM microscope.

The second achievement corresponds to high resolution structural studies of USPIO contrast agent nanoparticles (having an iron oxide core) in the atherotic mouse. For the first time with respect to past literature, the structural follow up of agent nanoparticles in the atherotic aorta has been achieved by CTEM, HRTEM down to subnanometer range and electron diffraction for particles embedded in the organ, showing that some nanoparticles keep their crystalline structure and size at times as long as 40-50 days after injection. This is consistent with the fact that some negative contrast regions can be seen on MR images of aorta at those times, and with the results from in vitro experiments in acidic medium mimicking the lysosomal metabolism. A first remark is that iron oxide structures like maghemite and even magnetite are very stable structures from a chemical point of view with respect to acids. Also the maghemite compound cannot be oxidized furthermore. Another consideration is that the study was made on ApoE -/- mice. Without the apolipoprotein E, which has a key role in the normal catabolism of triglyceride-rich lipoprotein constituents, the time needed for the liver to catabolise the additional lipids from the fat diet increases. This could diminish the capacity of the liver for neutralizing and destroying foreign substances. The iron oxide, a biocompatible substance, will be stored until the organism has the capacity to transform it in simpler elements.

An objective difficulty, pointed out in Chapter VI, occurred from the low density of agent nanoparticles in the aorta with respect to the spatial resolution of TEM techniques. Clearly this drawback together with a less marked TEM contrast expected from other phases

like ferritin made the study of nanoparticles under way of transformation more difficult. Another problem was the impossibility (to avoid dark contrast artefacts) of using standard post coloration of the TEM grids so that the tissular and cellular environments were not easily identified according to classical biology requirements. Hence it was not possible to assess whether many particles in the early stages could be located in a particular tissular or cellular environment whereas most of the configurations that we observed were consistent with internalisation of the nanoparticles in macrophages.

The new developments that we achieved in bi-photon microscopy using a fluorescent agent have shown that this technique provides the adequate intermediate scale of investigation with respect to TEM and HRTEM. The heterogeneous distribution of the agent nanoparticles in the aorta has been evidenced, with possible occurrence of very big agglomerates. High magnification studies proved that the procedure has the capability to reveal agglomerations of the agent nanoparticles at the macrophage scale. For practical (sanitary) reason, the present investigations could not be achieved on fresh tissues. New studies on fresh tissues combined with use of special reactive chemicals to reveal the cellular environment should allow to determine whether the nanoparticles are all internalized in macrophages or not. In a further step, quantification of the fluorescence should allow to map the nanoparticle density.

Our TEM studies of the aorta have shown that the nanoparticle get agglomerated in vesicles similar to those occurring more densely in the spleen, where those features could be then more easily studied. In late stages, those vesicles do correspond to phagolysosomes where the transformation into ferritin finally takes place. First results from STEM studies confirm that this technique offers the possibility of studying such a transformation in small vesicles at ultrahigh resolution.

With respect to the long time consuming SQUID measurements, the magnetic study has to be continued. Nevertheless the first results are consistent with a competition between the reduction in the size of nanoparticle iron oxide core and the magnetic interactions resulting from nanoparticle agglomeration in the vesicles, all data well correlated with results from TEM measurements.

Conclusions and perspectives

The present doctoral work has brought innovative achievements to understand the behavior of nanometric magnetic nanovectors, including USPIO contrast agents for MRI, before and after injection into the patient's body.

The first achievement concerns the development of a new mode of ESEM in transmission, called Wet-STEM, to investigate both the individual and the collective behavior of nanovectors in liquid suspensions. The present studies have revealed the structure of composite nanovectors having loaded a radioactivable compound of Rhenium; it should be mentioned here that Re can be replaced by Technetium whose biodistribution and accumulation in tissues can be investigated by gammagraphy.

The second achievement is related to the investigations of the biodistribution and the biotransformations of the USPIO contrast agents injected in atherotic mice for MRI examination of the aorta's atheroma. While revealing the heterogenous distribution of the agent nanoparticles in the tissues, especially in the aorta, our work has overcome this difficulty to bring the first revelation by HRTEM and diffraction, that some of these USPIO nanoparticles keep their morphological, structural and magnetic characteristics long times after the injection. These results are consistent with a model proposed for the degradation of the USPIO nanoparticles in an acidic medium mimicking the lysosomal environment.

In a multiscale approach, we showed that biphoton microscopy can be performed at the intermediate resolution adequate versus TEM.

Our studies demonstrated that biphoton microscopy has the capability to reveal the biodistribution of the USPIO contrast agents in tissues of aorta or spleen down to a few nm spatial resolution at the macrophage scale. Performed on fresh (non fixed) tissues from ex vivo samples, with specific labeling to differentiate different tissular components the biodistribution can be determined precisely using reactive products to reveal the cellular environment. Once detected, a region rich in nanoparticles can be then removed ex vivo by microbiopsy for further TEM studies. On the other hand, the biodistribution of the contrast agent revealed by biphoton microscopy can be possibly observed in situ in the patients using optical fibers.

APPENDIX I: Most common Gadolinium systems

The most common Gadolinium systems use as coating the chelates complexes DTPA (diethylenetriaminepentaacetic acid) or DOTA (1,4,7,10- tetraazacy clododecane-*N*,*N*',*N*'',*N*'''-tetraacetic acid). Their molecular structures are presented in Figure A.I.1.

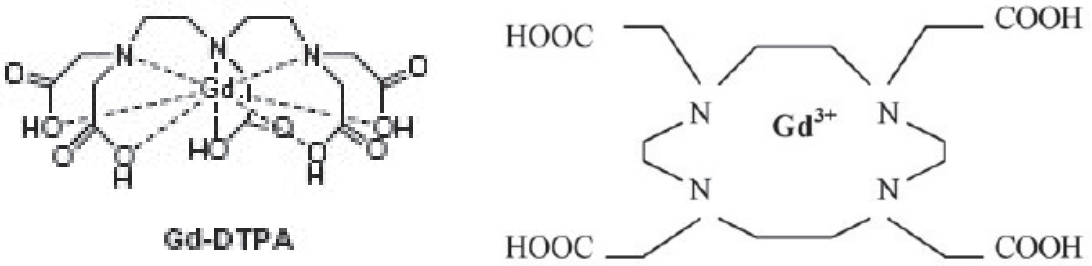

Figure A.I.1. The molecular structure of DPTA (left) and DOTA (right) chelate complexes.